

Galaxy clustering in the CFHTLS-Wide: the changing relationship between galaxies and haloes since $z \sim 1.2$ [★]

J. Coupon^{1,2,★★}, M. Kilbinger^{3,4}, H. J. McCracken⁵, O. Ilbert⁶, S. Arnouts⁷, Y. Mellier⁵,
U. Abbas⁸, S. de la Torre⁹, Y. Goranova⁵, P. Hudelot⁵, J.-P. Kneib⁶, and O. Le Fèvre⁶

¹ Astronomical Institute, Graduate School of Science, Tohoku University, Sendai 980-8578, Japan

² Institute of Astronomy and Astrophysics, Academia Sinica, P.O. Box 23-141, Taipei 10617, Taiwan

³ Excellence Cluster Universe, Technische Universität München, Boltzmannstr. 2, 85748 Garching, Germany

⁴ Universitäts-Sternwarte München, Scheinerstr. 1, 81679 München, Germany

⁵ Institut d'Astrophysique de Paris, UMR7095 CNRS, Université Pierre et Marie Curie, 98 bis Boulevard Arago, 75014 Paris, France

⁶ Laboratoire d'Astrophysique de Marseille (UMR 6110), CNRS-Université de Provence, 38, rue Frédéric Joliot-Curie, 13388 Marseille Cedex 13, France

⁷ Canada-France-Hawaii Telescope, 65–1238 Mamalahoa Highway, Kamuela, HI 9674

⁸ INAF-Osservatorio Astronomico di Torino, 10025 Pino Torinese, Italy

⁹ SUPA, Institute for Astronomy, University of Edinburgh, Royal Observatory, Blackford Hill, Edinburgh EH9 3HJ, UK

Received date / Accepted date

ABSTRACT

It has become increasingly apparent that studying how dark matter haloes are populated by galaxies can provide new insights into galaxy formation and evolution. In this paper, we present a detailed investigation of the changing relationship between galaxies and the dark matter haloes they inhabit from $z \sim 1.2$ to the present day. We do this by comparing precise galaxy clustering measurements over 133 deg^2 of the “Wide” component of the Canada-France-Hawaii Telescope Legacy Survey (CFHTLS) with predictions of an analytic halo occupation distribution (HOD) model where the number of galaxies in each halo depends only on the halo mass. Starting from a parent catalogue of $\sim 3 \times 10^6$ galaxies at $i'_{\text{AB}} < 22.5$ we use accurate photometric redshifts calibrated using $\sim 10^4$ spectroscopic redshifts to create a series of type-selected volume-limited samples covering $0.2 < z < 1.2$. Our principal result, based on clustering measurements in these samples, is a robust determination of the luminosity-to-halo mass ratio and its dependence on redshift and galaxy type. For the full sample, this reaches a peak at low redshifts of $M_{\text{h}}^{\text{peak}} = 4.5 \times 10^{11} h^{-1} M_{\odot}$ and moves towards higher halo masses at higher redshifts. For redder galaxies the peak is at higher halo masses and does not evolve significantly over the entire redshift range of our survey. We also consider the evolution of bias, average halo mass and the fraction of satellites as a function of redshift and luminosity. Our observed growth of a factor of ~ 2 in satellite fraction between $z \sim 1$ and $z \sim 0$ is testament to the limited role that galaxy merging plays in galaxy evolution for $\sim 10^{12} h^{-1} M_{\odot}$ mass haloes at $z < 1$. Qualitatively, our observations are consistent with a picture in which red galaxies in massive haloes have already accumulated most of their stellar mass by $z \sim 1$ and subsequently undergo little evolution until the present day. The observed movement of the peak location for the full galaxy population is consistent with the bulk of star-formation activity migrating from higher mass haloes at high redshifts to lower mass haloes at lower redshifts.

Key words. Cosmology: observations - large-scale structure of Universe - Galaxies: distances and redshifts - Galaxies: evolution - Galaxies: haloes

1. Introduction

In our current paradigm of galaxy formation, haloes of dark matter grow from tiny imperfections in the early Universe. Against the background (at the present day) of an accelerating Universe, structures grow “hierarchically”: small haloes form first and merge to build up larger ones, resulting in a complex filamen-

tary network where the most massive haloes lie at the nodes of the cosmic web (Springel et al. 2006). Galaxies form as baryons fall into the centres of dark matter haloes and the inflow of cold gas provides the fuel for star formation (White & Rees 1978; Fall & Efstathiou 1980). While this scenario broadly reproduces the observed galaxy distribution over a large range of scales and cosmic time, several open questions remain concerning which processes regulate star formation inside haloes and how this leads to the Hubble sequence observed at the present day.

These physical processes which drive galaxy formation and regulate star formation are expected to correlate closely to the mass of dark matter haloes which host galaxies. Therefore, a profitable avenue to pursue to better understand the physics of galaxy formation is to determine how the relationship between the stellar mass M_{star} and the dark matter halo mass M_{h} changes over the lifetime of the Universe. In the local Universe, abundance-matching studies have shown that at $z < 0.1$ the

Send offprint requests to: J. Coupon

[★] Based on observations obtained with MegaPrime/MegaCam, a joint project of CFHT and CEA/DAPNIA, at the Canada-France-Hawaii Telescope (CFHT) which is operated by the National Research Council (NRC) of Canada, the Institut National des Sciences de l'Univers of the Centre National de la Recherche Scientifique (CNRS) of France, and the University of Hawaii. This work is based in part on data products produced at TERAPIX and the Canadian Astronomy Data Centre as part of the Canada-France-Hawaii Telescope Legacy Survey, a collaborative project of NRC and CNRS.

^{★★} e-mail: coupon@asiaa.sinica.edu.tw

stellar-to-halo mass ratio (SHMR, $M_{\text{star}}/M_{\text{h}}$) reaches a maximum of a few percent at $M_{\text{h}} \sim 10^{12} M_{\odot}$, much smaller than the universal baryon fraction (Guo et al. 2010). This indicates that the conversion efficiency of baryons to luminous galaxies is highest at these halo masses. In less massive haloes, supernovae winds are responsible for gas reheating, which reduces star formation and flattens the galaxy luminosity function at the faint end (Benson et al. 2003). In more massive haloes, feedback from active galactic nuclei (Hopkins et al. 2006; Somerville et al. 2008) can “quench” star formation, leading to formation of the “red sequence” of passively evolving galaxies (Bower et al. 2006; Croton et al. 2006). The relative importance of these different processes as well as their dependence on environment, redshift and galaxy type is still very much an open question.

Ideally we would like to make a detailed comparison between the luminous content of dark matter haloes and the halo masses themselves as a function of redshift. Several methodologies exist to estimate halo masses: for example, using satellite kinematics (More et al. 2011), X-ray temperatures (Peterson & Fabian 2006; Cattaneo et al. 2009), or gravitational lensing (Heymans et al. 2006; Mandelbaum et al. 2006; Auger et al. 2010; Leauthaud et al. 2011b). However, the range in redshifts over which these techniques can be applied is limited, and amassing large samples is not always easy.

At the price of making some assumptions concerning the profiles of dark matter haloes and their evolution in number density, another way of inferring halo masses is from the observed galaxy clustering and mass functions. Usually, one makes the simplifying assumption that the number of galaxies in a given dark matter halo only depends on the halo mass, an assumption which has been verified with N -body simulations (Berlind et al. 2003, 2005; Berlind & Weinberg 2002; Kravtsov et al. 2004). Furthermore, the galaxy population of a halo, described by the “halo occupation distribution” (HOD), is assumed to be independent of environment and assembly history of the halo. Although some authors have shown that this “halo assembly bias” can have an observable effect on galaxy clustering measurements, the magnitude of this effect is, for the moment, much smaller than the size of systematic errors (Croton et al. 2007). This will be an important effect to test in future surveys.

In this paper we will use this model to investigate the changing relationship of dark matter and luminous matter from $z \sim 1.2$ to the present day. Until now, the majority of papers which have used HOD modelling to interpret galaxy clustering have analysed either large, low redshift surveys such as the SDSS (see, for e.g., Zehavi et al. 2010; Blake et al. 2008; Zehavi et al. 2010), or smaller ($\sim 1 \text{ deg}^2$) deep fields such as the COMBO-17 and COSMOS surveys (Phleps et al. 2006; Simon et al. 2009; Leauthaud et al. 2011b). For the moment, spectroscopic surveys at higher redshifts are also limited to small fields of view (Zheng et al. 2007; Abbas et al. 2010). Brown et al. (2008) has interpreted clustering measurements in the framework of the halo model of slightly larger redshift baseline, although their survey only covered $\sim 7 \text{ deg}^2$ and used five-band photometric redshifts. None of these surveys had the required combination of depth and areal coverage to make reliable measurements from low redshift to $z \sim 1$ of large samples of galaxies selected by type and intrinsic luminosity. In contrast, this is an ideal task for the Canada-France-Hawaii Legacy Survey (CFHTLS) with its unique combination of depth, area, and image quality.

The five-band u^*, g', r', i', z' CFHTLS photometry allows us to measure photometric redshifts out to $z \sim 1.2$ with $\sim 3\%$ accuracy and small systematic errors (Coupon et al. 2009). The large sky coverage, $\sim 133 \text{ deg}^2$ after masking, enables us to probe a

large range of halo masses. In addition, from the four independent fields of the CFHTLS we can obtain a reliable estimate of cosmic variance from the data itself. In this paper we construct a series of volume-limited samples selected by type, luminosity, and redshift, and use the halo model combined with the HOD formalism to infer how each galaxy sample populates their hosting dark matter haloes, and how this changes with look-back time.

The paper is organized as follows. In Section 2, we present our data set and catalogue production, including data reduction and photometric redshift measurement. In Section 3 we outline the techniques we use to estimate galaxy clustering, and in Section 4 we present our model. Results are described in Section 5 and discussed in Section 6. Conclusions are presented in Section 7.

Throughout the paper we use a flat Λ CDM cosmology ($\Omega_m = 0.25, \Omega_\Lambda = 0.75, H_0 = 70 \text{ km s}^{-1} \text{ Mpc}^{-1}$ and $\sigma_8 = 0.8$) with $h = H_0/100 \text{ km s}^{-1} \text{ Mpc}^{-1}$. All magnitudes are given in the AB system.

2. Observations, reductions and catalogue production

2.1. The Canada-France-Hawaii Legacy Survey

We use the “T0006” release of the CFHTLS Wide¹ (Goranova et al. 2009). The CFHTLS Wide has the mean limiting AB magnitudes (measured as the 50% completeness for point sources) $\sim 25.3, 25.5, 24.8, 24.48, 23.60$ in u^*, g', r', i', z' , respectively. An important feature in T0006 compared to previous releases is that for each MegaCam pointing (“tile”), the TERAPIX group provides a magnitude offset in each filter to account for tile-to-tile variations in magnitude zero points. These offsets are calculated using a stellar locus regression technique (High et al. 2009). In each tile, objects are detected on a $gri-\chi^2$ image (Szalay et al. 1999). Galaxies are selected using SEXTRACTOR “mag_auto” magnitudes (Bertin & Arnouts 1996), and colours are measured in $3''$ apertures which are all well matched to the median size of galaxies at our $i' < 22.5$ magnitude limit. The sky coverage of the four CFHTLS Wide fields is shown in Figure 1.

The MegaCam i -band filter broke in 2006, and subsequent observations were made with a new i -band filter denoted by “y”. Data from these two filters were treated separately with separate filter curves. Using a small data set observed with both the new y - and the old i -band, we detected no significant difference in photometric redshift accuracy. For the rest of the paper, we use i' to represent both filters.

2.2. Photometric redshift estimation

Our photometric redshifts were measured using LePhare (Arnouts et al. 2002) following the procedures outlined in Ilbert et al. (2006) and Coupon et al. (2009). Our primary template set is composed of the four Coleman et al. (1980) (CWW) observed spectra (EII, Sbc, Scd, Irr) complemented with two observed starburst spectral energy distributions (SED) from Kinney et al. (1996). This primary set of templates is optimized using the VVDS Deep spectroscopic sample. We performed an automatic calibration of the zero-points using spectroscopic redshifts in the W1, W3 and W4 fields. The calibration is obtained

¹ <http://terapix.iap.fr/cpl/T0006-doc.pdf>

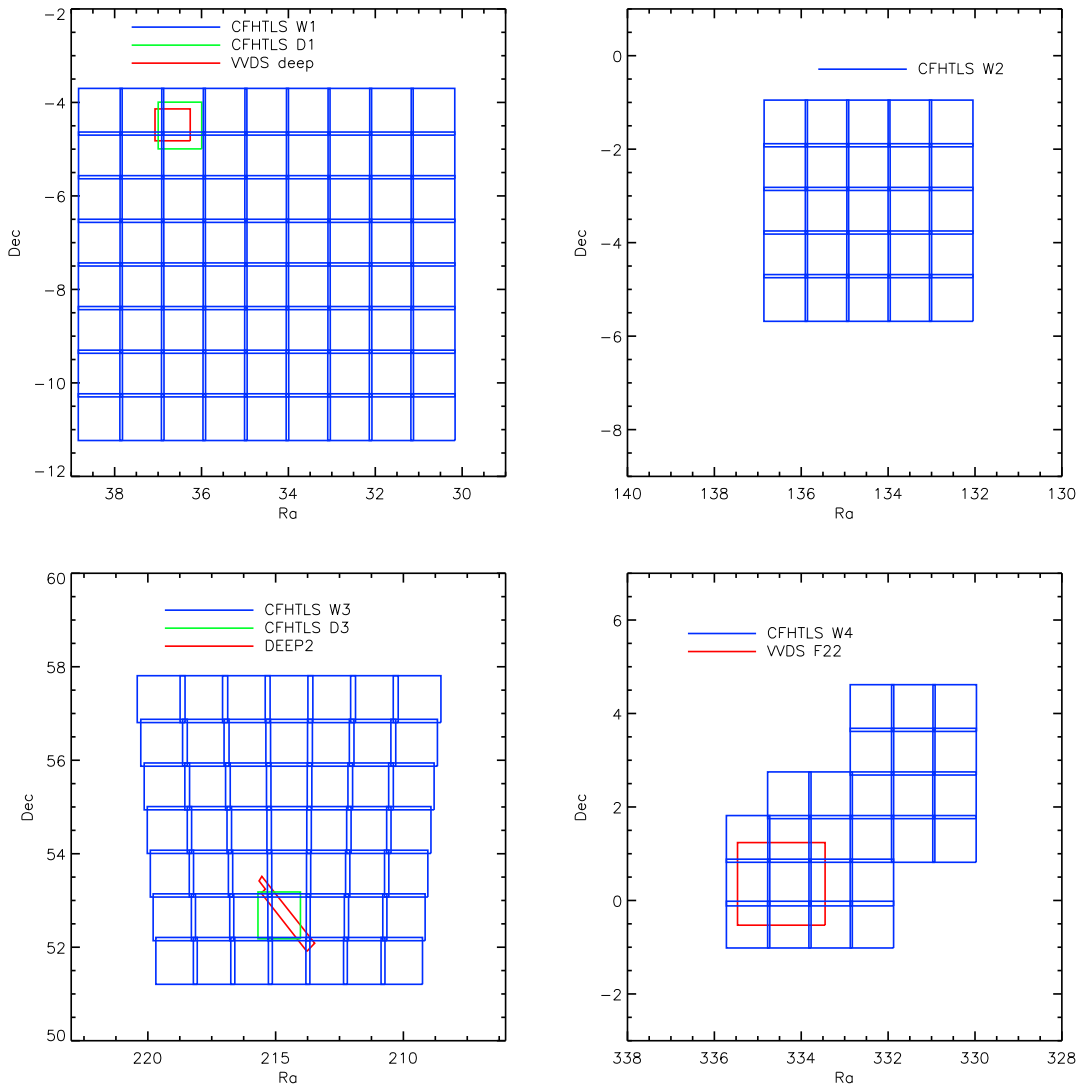


Fig. 1. Sky coverage of W1, W2, W3 and W4 fields. Each blue square represents one MegaCam pointing. Spectroscopic data (VVDS F02, F22, and DEEP2) are in red. CFHTLS Deep fields overlapping with the wide survey (D1 and D3) are shown in green.

by comparing the observed and modelled fluxes, and done iteratively until the zero-points converge. For spectral types later than Sbc, we introduced a reddening $E(B - V) = 0$ to 0.35 using the Calzetti et al. (2000) extinction law.

Without near-infrared photometry, Lyman- and Balmer-breaks create degeneracies between high and low photometric redshift solutions. Following a Bayesian approach similar to Benítez (2000) and Ilbert et al. (2006), we adopt a “prior” based on the observed spectroscopic redshift distribution to reduce the number of catastrophic failures. No redshift solution is allowed which will produce a galaxy brighter than $M_g = -24$.

Our photometric redshifts were calibrated with spectroscopic samples. The VVDS Deep survey (Le Fèvre et al. 2005) is available in the W1 field. The VVDS Deep is a pure magnitude-limited sample at $I_{AB} < 24$ and we used 5926 secure redshifts (flags 4 and 5) for photometric calibration, and for building the redshift distribution prior. From the VVDS F22 (“VVDS WIDE”, Garilli et al. 2008) in W4 we used 4514 galaxies limited to $I_{AB} < 22.5$. This sample has a success rate of 92%. Finally, in the W3 field, 1267 redshifts from the DEEP2

survey (Davis et al. 2003) selected at $R_{AB} < 24.1$ were used for photometric calibration. No spectroscopic redshifts were available in W2.

To estimate photometric redshifts, we adopted a slightly different method than for previous studies to measure redshifts from the probability distribution function (PDF). Rather than directly using the redshift that minimizes the χ^2 distribution function, we chose the median of the PDF. It has been found that the maximum likelihood estimate can lead to a systematic concentration of photometric redshifts around discrete values (“redshift focusing”), although we checked that the effect is very small for redshift bins of size $\Delta z > 0.1$.

The redshift accuracy (“ σ ”) of our samples with spectroscopic redshift z_s and photometric redshift z_p is defined as $\sigma_{\Delta z} / (1 + z_s)$, where $\Delta z = |z_p - z_s|$ represents the difference between spectroscopic and photometric redshift. We use the normalised median absolute deviation as accuracy estimator (NMAD, Hoaglin et al. 1983), expressed as $\sigma_{\Delta z} = 1.48 \times \text{median}(|z_p - z_s|)$. “Catastrophic” redshifts are defined as objects with $|z_p - z_s| / (1 + z_s) > 0.15$. The percentage of catas-

trophic redshifts is denoted by η . The dispersion and the fraction of catastrophic redshifts increase from bright to faint samples. The accuracy is $\sigma_{\Delta_z}/(1+z_s) = 0.034$ (W1) to 0.037 (W4) at $i' < 21.5$ and reaches 0.039 (W1) to 0.051 (W3) at $21.5 < i' < 22.5$. The failure rate increases from $\eta \sim 1.4\%$ at $i' < 21.5$ to $\eta \sim 5.5\%$ at $21.5 < i' < 22.5$. Galaxies with redder colours (El, Sbc) have more accurate photometric redshift estimates ($\sigma_{\Delta_z}/(1+z_s) = 0.031$, $\eta = 1.64\%$) than bluer ones (Scd, Irr and starbursts, $\sigma_{\Delta_z}/(1+z_s) = 0.038$, $\eta = 3.69\%$).

We constructed a merged catalogue with unique objects from individual tile catalogues provided by TERAPIX. We identified duplicate sources positionally and chose the object closest to the centre of its original tile. Although photometric redshifts were estimated to $i' < 24$, we selected objects brighter than $i' = 22.5$ to maintain a low outlier rate (see Table 3 of Coupon et al. 2009) and to ensure catalogue completeness. This sample covers a total effective area of 133 deg^2 . We show the photometric redshift accuracy in the secure redshift range covered in this study, $0.2 < z < 1.2$, compared to spectroscopic redshifts in Fig. 2.

Stars appear as point-like sources on the image and can easily be identified using their half-light radius at bright magnitudes; however, at fainter magnitudes this estimator can be confused by unresolved galaxies. We refined our star-galaxy separation by combining this profile-magnitude criteria with a colour-based criteria. We computed the half-light radius limit for each tile from the median and dispersion of the brightest objects and classified as stars all objects brighter than $i' = 20$ with flux radii limits smaller than this amount. In the magnitude range $20 < i' < 22.5$, we classified stars as objects smaller than the half-light radius *and* with $\chi^2(\text{star}) < \chi^2(\text{galaxy})$, where $\chi^2(\text{object})$ is estimated from the stellar and galaxy template libraries.

We eliminated objects observed with less than three filters and with $\chi^2(\text{galaxy}) > 100$. We suspect that these objects are false detections or rare objects with wrong photometric redshift estimates. Most of these objects reside in specific areas, such as around bright stars and field borders where the masking procedure has failed.

Using the photometric redshift, the associated best-fitting template and the observed apparent magnitude in a given band, we can directly measure the k -correction and the absolute magnitude in any rest-frame band. Since at high redshifts the k -correction depends strongly on the galaxy spectral energy distribution, it is the main source of systematic error in determining absolute magnitudes. To minimise k -correction uncertainties, we derive the rest-frame luminosity at λ using the object's apparent magnitude closer to $\lambda \times (1+z)$. We use either the u^* , g' , r' , i' , or z' observed apparent magnitudes according to the redshift of the galaxy (the procedure is described in Appendix A of Ilbert et al. 2005). For this reason the bluest absolute magnitude estimate makes full advantage of the complete observed magnitude set. However, as the u -band flux has larger photometric errors, we decided to use M_g -band magnitudes.

3. Clustering measurements

3.1. Sample selection and galaxy number density estimation

Objects are selected with $i' < 22.5$ and divided into five redshift bins: $0.2 < z < 0.4$, $0.4 < z < 0.6$, $0.6 < z < 0.8$, $0.8 < z < 1.0$, and $1.0 < z < 1.2$. A large bin width ($\Delta_z = 0.2$) ensures a low bin-to-bin contamination from random errors ($\sigma_z < 0.1$). We investigate effects from systematic errors in Sect. 3.2. The complete sample contains 2 924 730 galaxies. To separate galaxies

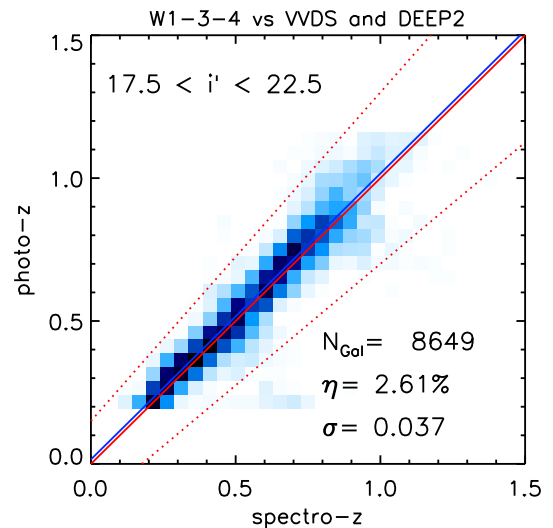


Fig. 2. Photometric redshift accuracy in the $0.2 < \text{photo-}z < 1.2$ interval. The figure shows the number density of photometric redshifts in W1, W3 and W4, versus spectroscopic redshifts from VVDS and DEEP2 surveys. The blue line is a linear fit to photo- z versus spectro- z .

into “red sequence” and “blue cloud” types, we used a criterion based on best-fitting galaxy templates. We define “red” galaxies as objects with best-fitting CWW templates (see Sect. 2.2) estimated as El and Sbc (early-type), and “blue” galaxies estimated as Sbc, Scd, Im, SB1 and SB2 (late-type). Selecting galaxies by best-fitting template is a more robust way of selecting galaxies by type, as compared to a simple colour selection, and it is less sensitive to the effects of dust extinction. Our resulting colour selection in the absolute magnitude-redshift plane is shown in Fig. 3. We note that a small amount of red-classified galaxies at high redshift $z > 0.8$ have slightly bluer colours. Their distribution peaks near the blue galaxy distribution, suggesting that these objects could be blue galaxies erroneously identified as red galaxies due to photometric redshift errors. We also note that a simple colour cut would not exactly reproduce our selection. However, in the interests of simplicity and clarity we keep the “red”/“blue” labels for the rest of the paper.

We extract volume-limited luminosity-selected samples for each of the “full” (or “all galaxies”), “red” and “blue” samples, using M_g absolute magnitude thresholds (hereafter denoted as “luminosity threshold samples”), from $M_g - 5 \log h = -17.8$ (fainter threshold in the range $0.2 < z < 0.4$) to $M_g - 5 \log h = -22.8$ (brighter threshold in the range $1.0 < z < 1.2$). The sample selection is illustrated in Fig. 4. For the rest of this paper we will refer to these samples as simply full, red and blue. Due to low numbers of pairs at small scales, luminous blue samples were discarded. We are left with 45 samples, each comprising on average $\sim 153\,000$, $\sim 70\,000$ and $\sim 129\,000$ galaxies for a typical full, red and blue sample, respectively. The sample properties are displayed in Tables B.1, B.2 and B.3.

Finally, in each redshift interval $[z_{\min}; z_{\max}]$ we compute the galaxy number density:

$$n_{\text{gal}}^{\text{obs}} = N_{\text{total}} / \left[\Omega \int_{z_{\min}}^{z_{\max}} \frac{dV}{dz} dz \right], \quad (1)$$

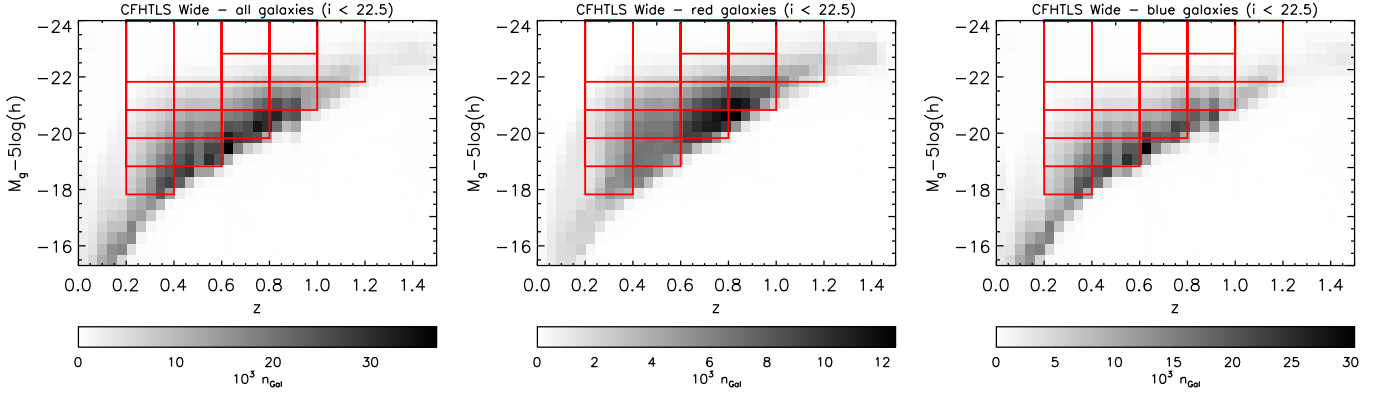


Fig. 4. Sample selection in the full (left), red (center) and blue (right) galaxy samples. In each panel, the galaxy number density in the plane M_g/z is shown; red rectangles represent the luminosity threshold samples.

where Ω represents the solid angle subtended by the survey, and dV/dz the volume element. Errors are estimated from the weighted galaxy number density field-to-field variance.

3.2. Photometric redshift uncertainties

Our modelled two-point correlation function is projected using the measured redshift distributions. In order to take into account statistical errors on redshifts, we select galaxies in the redshift range considered and convolve the observed redshift distributions with the estimated photometric redshift errors, derived from the probability distribution functions. We construct a Gaussian error distribution for each galaxy centred on the median redshift of the PDF, with a width corresponding to the 68% confidence limits of the PDF, and normalised to unity. We then sum these Gaussians to construct the redshift distribution resampled to a redshift bin width of 0.04. Redshift distributions for each sample are illustrated in Fig. 5.

To further assess the quality of photometric redshifts, we perform the cross-correlation analysis introduced in Benjamin et al. (2010). The measurement of the angular correlation functions for galaxies in different photo- z bins is used to constrain the fraction of galaxies that are scattered into “wrong” redshift bins due to photo- z errors. We measure the bin-to-bin cross correlation function for the full, red and blue samples, respectively. A non-zero correlation between adjacent redshift bins is present in all cases. This may be due to the presence of large-scale structures extending over several redshift bins. More importantly, this is also due to photometric redshift scatter, which results in the leakage of galaxies into neighbouring bins. This error contribution to the redshifts is taken into account by the convolution of the redshift distribution with the errors, therefore, we do not consider adjacent bins further in the analysis of photometric redshift uncertainties.

The angular cross-correlation of galaxies in non-adjacent redshift bins is much lower, indicating a small fraction of catastrophic outliers. We use the “global pairwise analysis” method to measure the contamination between two redshift bins i and j . In this approximation, the following linear combinations of the angular cross-correlation function w_{ij} and the two auto-correlation functions, w_{ii} and w_{jj} , respectively, are expected to cancel for all angular scales θ_i ,

$$d_i = w_{ij}(\theta_i) (f_{ii}f_{jj} + f_{ij}f_{ji}) - w_{ii}(\theta_i) \frac{N_i}{N_j} f_{ij}f_{jj} - w_{jj}(\theta_i) \frac{N_j}{N_i} f_{ji}f_{ii}$$

$$= 0. \quad (2)$$

Here, N_i (N_j) is the observed number of galaxies in bin i (j). The contamination f_{ij} is the number of galaxies with true redshift in bin i , but misidentified into bin j , as a fraction of the true number of galaxies in bin i . For each bin pair (i, j) , the leakage of the other redshift bins is neglected. This approximation is valid for contamination fractions of up to 10% (Benjamin et al. 2010). With this, the fraction of galaxies which stay in their bin is $f_{ii} = 1 - f_{ij}$. We fit the two parameters f_{ij} and f_{ji} in Eq. 2 by performing a χ^2 null-test on d_i . For the covariance $\langle d_i d_s \rangle$, we take into account the correlation between angular scales for each of the three correlation functions using a Jackknife estimate (see next section). We neglect the sub-dominant covariance between different correlation functions. This corresponds to using the first three terms in Eq. A4 of Benjamin et al. (2010).

Due to degeneracies between the parameters f_{ij} and f_{ji} , large values for f_{ij} ($i > j$) cannot be ruled out in principle. However, for the full and red galaxy samples, the contamination fractions are consistent with zero in most cases. The blue galaxy samples are slightly worse, but contaminations are consistent with values between 2% and 10%. Together with the very low outlier rate for the sub-sample with spectroscopic redshifts (see Fig. 2), these results further strengthen our confidence in the photometric redshift estimates in this work and to use them to measure angular correlation functions. Our measurements for the full sample are shown in Fig. 6.

Bin-to-bin mixing caused by photometric redshift errors will reduce our measured clustering signal, given that objects in separate bins are uncorrelated. This would lead to an underestimation of halo masses, as low mass haloes tend to be less clustered than more massive ones. However, it is not trivial to predict how galaxy number density estimates would be affected by such errors, which may result in incomplete or contaminated samples. Since the halo number density decreases monotonically with halo mass, galaxy number density decreases with increasing host halo mass. Therefore, a contaminated sample will underestimate halo mass fitting estimates. Conversely, an incomplete sample will tend to overestimate halo masses.

To understand how photometric redshift errors could affect our results as function of redshift and luminosity threshold, we compared our measurements in the CFHTLS Wide with those from the “Deep” component of the CFHTLS (Goranova et al. 2009), where more precise photometric redshifts are available (see Table 3 in Coupon et al. 2009). Photometric redshifts in

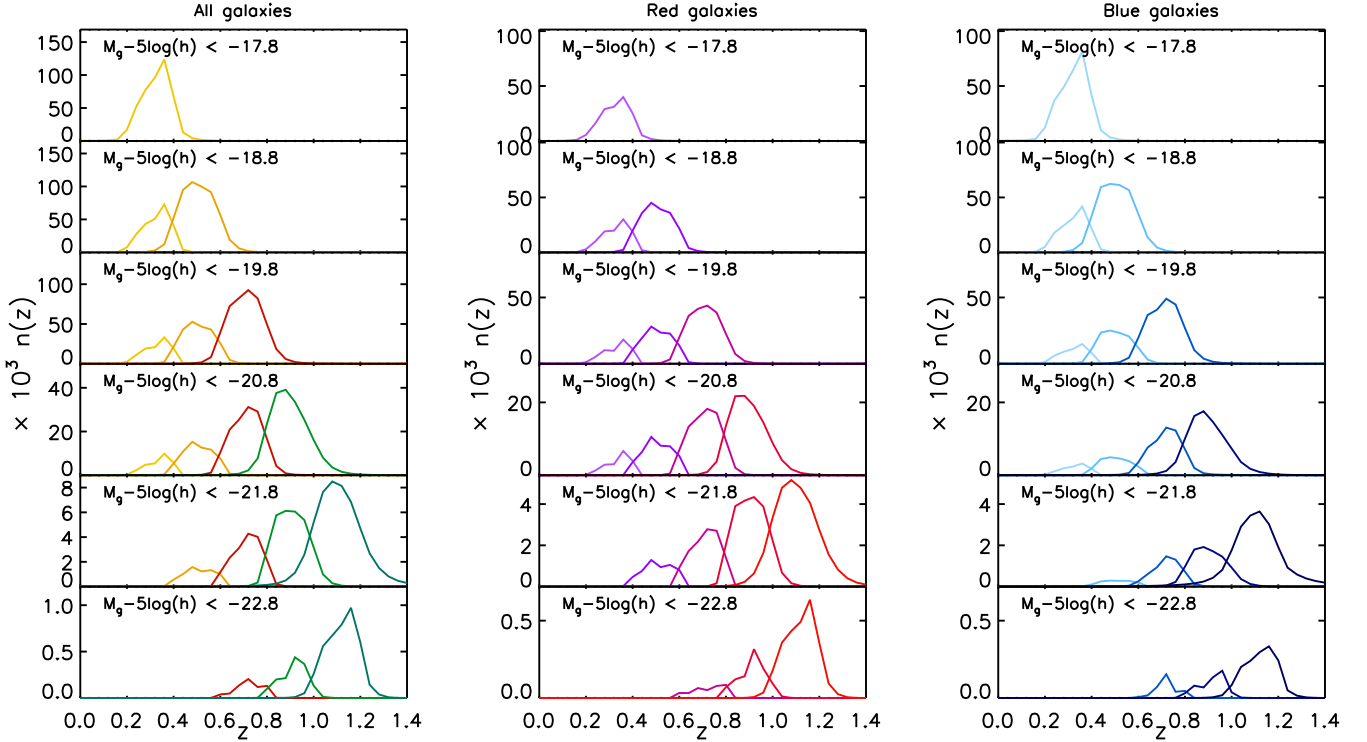


Fig. 5. Redshift distributions for the full (left), red (center) and blue (right) galaxy samples as function of absolute magnitude threshold.

the CFHTLS Deep were computed using the method described in Sect. 2.2 and to avoid cosmic variance uncertainties we performed our tests in overlapping areas between the Wide and the Deep, D1/W1 and D3/W3, over a total area of 2 deg^2 .

These tests show that faint luminosity threshold samples are slightly incomplete at low redshift, probably as a consequence of catastrophic errors moving low redshift galaxies to higher redshift. We report that the difference in galaxy density between the Wide and the Deep estimates rarely exceeds the field-to-field variance error estimate. However, brighter and brighter samples become more and more contaminated by spurious objects, and in the worst case (the brightest sample in the range $0.8 < z < 1.0$), the number of objects in the Wide is more than three times higher than in the Deep, much larger than the 40% field-to-field variance. A higher galaxy number density estimate will enhance the effect of a reduced clustering signal, which may result in underestimated halo masses for brighter samples up to a few sigmas. In the worst case, this represents a bias of ~ 0.5 in $\log M_{\text{min}}$.

3.3. Angular correlation function

We measure the two-point angular correlation function w using the Landy & Szalay (1993) estimator

$$w(\theta) = \frac{N_r(N_r - 1)}{N_d(N_d - 1)} \frac{\langle DD \rangle}{\langle RR \rangle} - \frac{N_r - 1}{N_d} \frac{\langle DR \rangle}{\langle RR \rangle} + 1, \quad (3)$$

where $\langle DD \rangle$ is the number of galaxy pairs, $\langle RR \rangle$ the number of random pairs, $\langle DR \rangle$ the number of galaxy-random pairs, all in a bin around the angular separation θ . N_d and N_r are the number of galaxies and random objects, respectively. A random catalogue is generated for each sample. In order to find an acceptable

compromise between small Poisson errors and computational requirements we scale N_r depending on the number of galaxies in our input catalogues, from $50 \times N_d$ in the case of low density data catalogues to $2 \times N_d$ for high density catalogues. We measure w using a fast two-dimensional tree code. At large separations θ , instead of counting individual galaxy pairs, we correlate boxes by multiplying the number of objects in the two boxes. For that, we define a threshold angle $\alpha_w = \theta/d_b$, where d_b is the box size. Below this threshold, the number of objects inside the box is taken into account instead of individual objects. We found that $\alpha_w = 0.05$ gives accurate results at low computational cost.

We correct our galaxy correlation measurements for the “integral constraint” (Groth & Peebles 1977), a correction factor which arises from the finite area of our survey Ω^2 :

$$w(\theta) = w_{\text{mes}}(\theta) + w_C. \quad (4)$$

The correction factor w_C can be estimated as follows:

$$w_C = \frac{1}{\Omega^2} \iint w(\theta) d\Omega_1 d\Omega_2, \quad (5)$$

assuming a simple power law fitted on the data with slope γ and amplitude A_w :

$$w_{\text{mes}}(\theta) = A_w \theta^{1-\gamma} - w_C = A_w (\theta^{1-\gamma} - C). \quad (6)$$

As A_w varies with each sample, we first compute C using Monte Carlo integration over random pairs

$$C = \frac{\sum \theta^{1-\gamma} RR(\theta)}{\sum RR(\theta)}, \quad (7)$$

and then correct $w_{\text{mes}}(\theta)$ using

$$w(\theta) = w_{\text{mes}}(\theta) \frac{\theta^{1-\gamma}}{\theta^{1-\gamma} - C}. \quad (8)$$

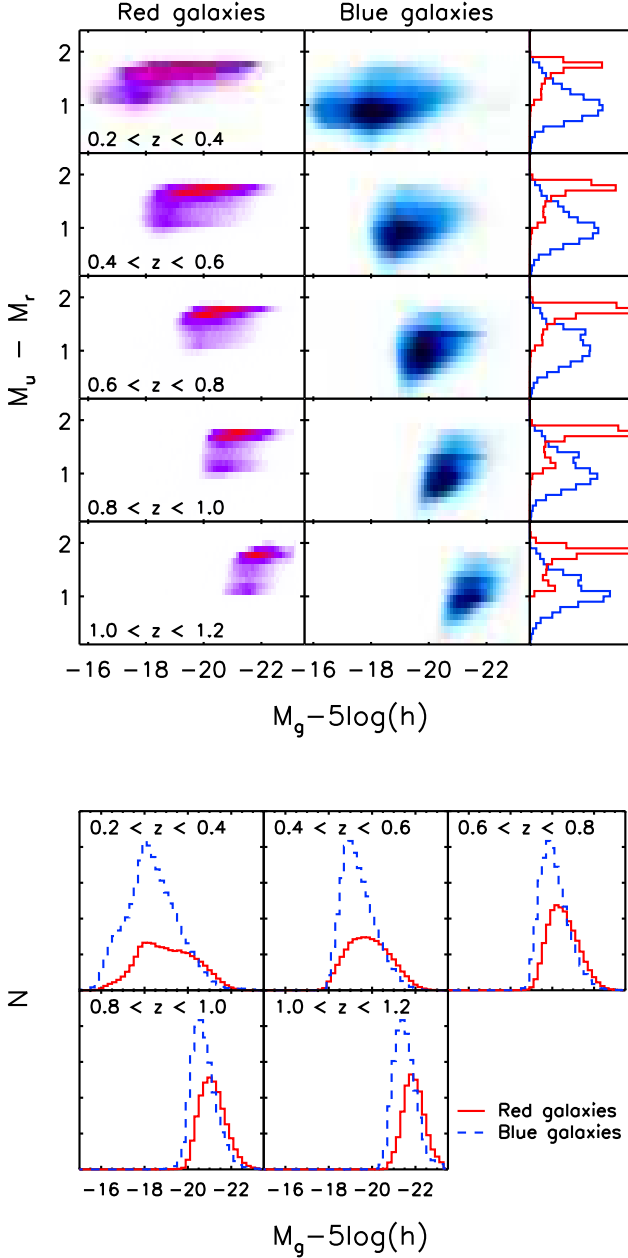


Fig. 3. Top: type selection based on best fitting templates for the “red” sample (left) and the “blue” sample (right) in the CFHTLS Wide. We show the colour distribution ($M_u - M_r$) as function of absolute magnitude (M_g) and redshift (top to bottom) and number counts for “red” and “blue” objects on the right panels. Bottom: number of red and blue galaxies as function of magnitude and redshift.

The integral constraint for the four Wide fields is $C \sim 0.5$. Assuming $\gamma = 1.8$, this leads to a correction of $\sim 10\%$ at $\theta = 0.1$ deg and up to a factor of two at $\theta = 1.0$ deg. We note that assuming a power-law for $w(\theta)$ to estimate C could be a source of error; it is neglected in the current analysis as the correction is smaller than our Jackknife error estimates.

We combine our galaxy samples from the four CFHTLS fields into a single catalogue for the correlation function measurement. Computing $w(\theta)$ on the four fields independently, and

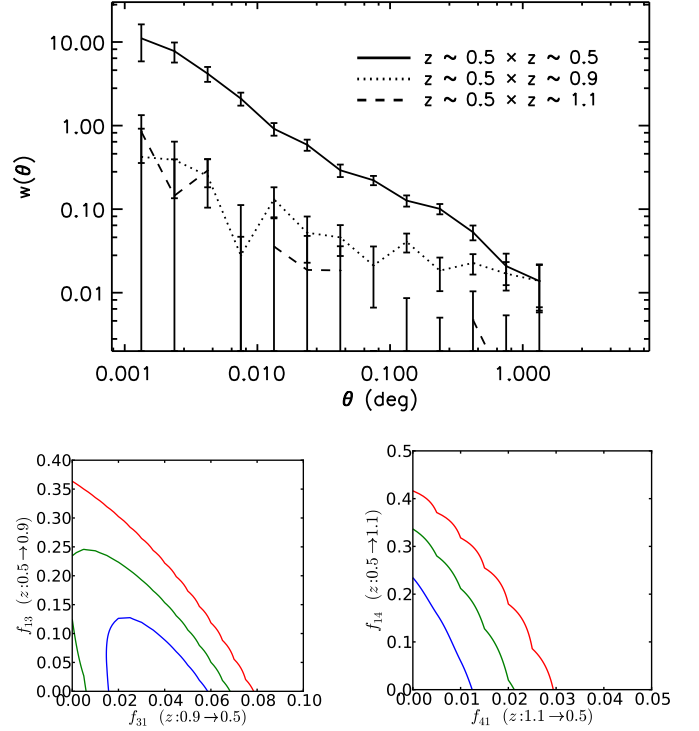


Fig. 6. Cross correlation analysis between redshift bins for the full sample. Top: auto-correlation in the redshift bin $0.4 < z < 0.6$ (straight line) and cross-correlation between the bins $0.4 < z < 0.6$ and $0.8 < z < 1.0$ (dotted line) and between $0.4 < z < 0.6$ and $1.0 < z < 1.2$ (dashed line). Bottom: quantitative estimates of the contamination (percentage of galaxies scattered) from a pairwise analysis between redshift bins $0.4 < z < 0.6$ and $0.8 < z < 1.0$ (left) and between $0.4 < z < 0.6$ and $1.0 < z < 1.2$ (right). The contours show the 68.3 (blue), 95.5 (green) and 99.7 (red) confidence regions.

using a pair-weighted average would not lead to the same clustering estimate at large scales. Relative photometric offsets are expected to vary more from one field to another than within the same field, as the four fields are non-overlapping. Since our parent catalogue is selected by apparent magnitude cut ($i' < 22.5$), even a small difference in photometric offsets will lead to a spurious field-to-field variation of the galaxy number density. In addition, different photometric offsets could bias the photometric redshift selection and also increase the field-to-field density fluctuations. A 0.02 magnitude offset variation would result in a $\sim 2\%$ variation in galaxy number density, which may bias the two-point correlation at very large scales. Because we expect these effects to occur at the scale of individual field (a few degrees), we adopt a conservative cut and limit our measurements to $\theta < 1.5$ deg. We do not measure w at separations below $3''.6$ to avoid blended objects. Two-point correlation function measurements and errors are provided in the appendix C.

3.4. $w(\theta)$ error estimates

We estimate statistical errors on the two-point correlation function using the Jackknife internal estimator. We divide all samples into $N = 68$ sub-samples of about 2 deg^2 . Removing one

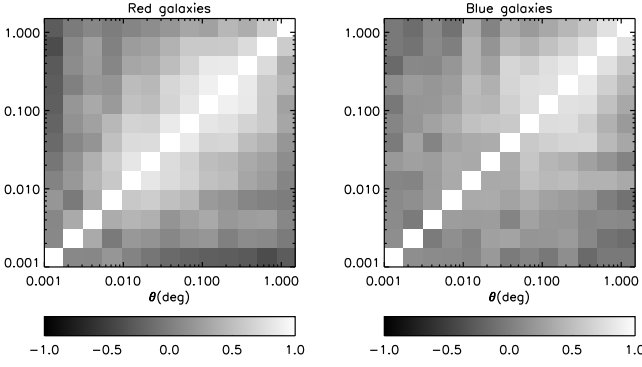


Fig. 7. Covariance matrix correlation coefficients of $w(\theta)$ from Jackknife estimates, for galaxy samples with $0.4 < z < 0.6$ and $M_g - 5 \log h < -19.8$. Left panel: red sample. Right panel: blue sample.

sub-sample at a time for each Jackknife realisation, we compute the covariance matrix as

$$C(w_i, w_j) = \frac{N-1}{N} \sum_{l=1}^N (w_i^l - \bar{w}_i)(w_j^l - \bar{w}_j), \quad (9)$$

where N is the total number of subsamples, \bar{w} the mean correlation function, and w^l the estimate from the l^{th} Jackknife sample. Since $w(\theta)$ is computed from a combined catalogue including all four fields, our Jackknife estimate leads to a noisy but fair estimate of cosmic variance. We apply the correction factor given by Hartlap et al. (2007) to the inverse covariance matrix to compensate for the bias introduced by the noise. We show the correlation coefficient of the covariance matrix, $r_{ij} = C_{ij} / \sqrt{C_{ii}C_{jj}}$ for two red and blue samples, respectively, in Fig. 7.

4. Filling haloes with galaxies: the halo occupation model

4.1. The halo occupation distribution

In order to relate galaxies to the dark matter haloes which host them we have implemented an analytic model of galaxy clustering, the halo model (for a review see Cooray & Sheth 2002), which contains at its core a prescription for how galaxies populate haloes, namely the halo occupation distribution. Our model follows closely the approaches used in recent works; further details and references can be found in Appendix A. The key assumption underlying our halo occupation distribution function is that the number of galaxies N in a given dark matter halo depends only on the halo mass M ; it does not depend on environment of formation history of the haloes. Furthermore, following Zheng et al. (2005), we express $N(M)$ as the sum of two terms, corresponding to the contribution from the central galaxy N_c and the satellite galaxies N_s :

$$N(M) = N_c(M) \times [1 + N_s(M)], \quad (10)$$

where

$$N_c(M) = \frac{1}{2} \left[1 + \operatorname{erf} \left(\frac{\log M - \log M_{\min}}{\sigma_{\log M}} \right) \right], \quad (11)$$

$$N_s(M) = \left(\frac{M - M_0}{M_1} \right)^\alpha. \quad (12)$$

The smooth transition for central galaxies expresses the uncertainties in the galaxy formation process (Zheng et al. 2007). The factor $N_c(M)$ for the satellite number in $N(M)$ accounts for the fact that a halo cannot be populated by satellite galaxies without the presence of a central galaxy.

For a given cosmology and dark matter halo profile, our model has five adjustable parameters. M_{\min} is the mass scale for which 50% of haloes host a galaxy. To reflect the scatter in the luminosity-halo mass relation, a smooth transition of width $\sigma_{\log M}$ is used. Zheng et al. (2007) show that if this scatter is small, the above expression takes the identical form as the distribution of central galaxies given a halo mass M , integrated over the entire luminosity range above the luminosity threshold. Thus M_{\min} also represents the halo mass scale for central galaxies, whose mean luminosity $\langle L_c \rangle$ is equal to the luminosity threshold L_{\min} .

This simple relation between M_{\min} and L_c is based on the hypothesis that stellar mass (or luminosity) has a power law dependence on halo mass, which may not be exact over the entire mass range. Leauthaud et al. (2011a) recently proposed a model in which this relation assumes a more realistic form. The authors showed that in their model M_{\min} and $\sigma_{\log M}$ take different values than those computed with other models. However, in the mass range over which we compare our results with theirs in Sect. 6 ($M_h \sim 10^{12} h^{-1} M_\odot$), M_{\min} values do not differ by more than 10% (see Fig. 3 in Leauthaud et al. 2011a).

The number of satellite galaxies as function of halo mass follows a power law with slope α and amplitude M_1 . M_1 then represents the characteristic scale for haloes hosting one satellite galaxy. At lower masses, the dependence becomes steeper and the transition mass scale occurs at $M \sim M_0$.

We show in Fig. 8 an example of measured $w(\theta)$ and its best-fitting model, together with the best-fitting HOD function $N(M)$. The total galaxy correlation function is the sum of two terms. At distances much smaller than the virial radius, the one-halo term contains contributions from galaxy pairs within a single halo, whereas at large distances the two-halo term contains contributions from pairs in separate haloes.

4.2. Deduced parameters

From the HOD model we obtain deduced parameters describing galaxy properties. The mean galaxy bias b_g at redshift z is the mass-integral over the halo bias b_h (see Sect. A) weighted by the number of galaxies,

$$b_g(z) = \int dM b_h(M, z) n(M, z) \frac{N(M)}{n_{\text{gal}}(z)}. \quad (13)$$

The dark-matter mass function n is given in Eq. A.6, and the halo bias b_h in Eq. A.14. The total number of galaxies is

$$n_{\text{gal}}(z) = \int N(M) n(M, z) dM. \quad (14)$$

Similarly to the galaxy bias, the mean halo mass for a galaxy population is

$$\langle M_{\text{halo}} \rangle(z) = \int dM M n(M, z) \frac{N(M)}{n_{\text{gal}}(z)}. \quad (15)$$

The fraction of central galaxies per halo is

$$f_c(z) = \int dM n(M, z) \frac{N_c(M)}{n_{\text{gal}}(z)}. \quad (16)$$

Consequently, the fraction of satellite galaxies is

$$f_s(z) = 1 - f_c(z). \quad (17)$$

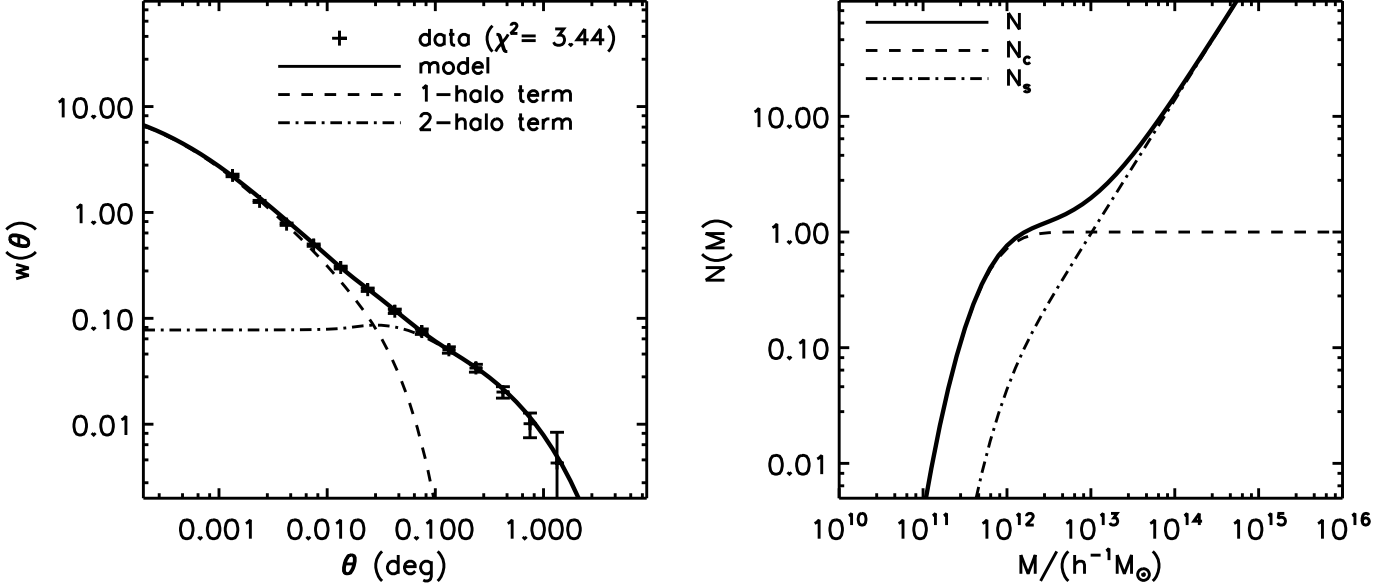


Fig. 8. Example of a measured $w(\theta)$ (for all galaxies in the redshift range $0.4 < z < 0.6$ and for $Mg - 5 \log h < -19.8$), as well as the best-fitting model, as described in sec. 4. Left: $w(\theta)$ measurement and model. Right: $N(M)$, showing the central term N_{cent} and the satellite term N_s .

4.3. Population Monte Carlo sampling

We use the ‘‘Population Monte Carlo’’ (PMC) technique to sample likelihood space (Wraith et al. 2009; Kilbinger et al. 2010, 2011) and have implemented it in a publicly-available code, CosmoPMC². Contrary to the widely-used Monte Carlo Markov Chain method (MCMC), PMC is an adaptive importance-sampling technique (Cappé et al. 2004, 2008), which has two principal advantages: first, the parallel sampling algorithm combined with our fast HOD code means that each run can be quickly computed. Secondly, PMC does not have issues with chain convergence. Instead, the perplexity (defined below) is a diagnostic for the reliability of a given sampling run.

Points are sampled from a simple, so-called importance sampling function q . Each sample point θ_n is attributed a weight \bar{w}_n which is the ratio of the posterior π to the importance function,

$$\bar{w}_n \propto \frac{\pi(\theta_n)}{q(\theta_n)}; \quad \sum_{n=1}^N \bar{w}_n = 1. \quad (18)$$

The initial importance sampling function q is a mixture of seven multi-variate Gaussians. A PMC run consists of a number of iterations, in the course of which the importance function is adapted to better match the posterior distribution. We run PMC for typically 10 iterations using 10 000 sample points per iteration.

As a stopping criterion for the iterations we take the perplexity p which is defined as

$$p = \frac{1}{N} \exp \left(- \sum_{n=1}^N \bar{w}_n \log \bar{w}_n \right). \quad (19)$$

The perplexity $p \in [0; 1]$ is a measure of the distance between the posterior and the importance function, and it approaches unity if the two distributions are identical. The perplexity is a measure of the adequacy and efficiency of the sampling.

Values of p above about 0.6 indicate a good agreement between the posterior and the importance function.

The evaluation of the likelihood function, which is the most time-consuming process for most sampling tasks, is easily parallelisable in importance sampling with little overhead. Furthermore, we have optimized several aspects of the numerical computations of the HOD model. For example, we employ the FFTLog (Hamilton 2000) algorithm to perform Fourier transforms and make use of tabulated values to improve efficiency. The computation of the angular correlation function w on a range of scales is performed in under a second on a standard desktop. This module is part of the latest public version (v1.1) of CosmoPMC. Typically, on an eight-core desktop (16 threads) a single PMC run takes around 90 minutes for a total of 100,000 sample points. Our PMC technique allows us to efficiently sample the parameter space for the large number of galaxy samples used in this work.

4.4. Likelihood function

For each galaxy sample we simultaneously fit both the projected angular correlation function w and the number density of galaxies n_{gal} , by summing both contributions in log-likelihood:

$$\chi^2 = \sum_{i,j} [w^{obs}(\theta_i) - w^{model}(\theta_i)] (C^{-1})_{ij} [w^{obs}(\theta_j) - w^{model}(\theta_j)] + \frac{[n_{gal}^{obs} - n_{gal}^{model}]^2}{\sigma_{n_{gal}}^2}, \quad (20)$$

where n_{gal}^{model} is given by Eq. 14, at the mean redshift of the sample. The data covariance matrix C is approximated by Eq. 9. The error on the galaxy number density $\sigma_{n_{gal}}$ contains Poisson noise and cosmic variance. The latter is estimated from the field-to-field variance between the four Wide patches.

² <http://cosmopmc.info>

The likelihood function is

$$\mathcal{L} = \exp(-\chi^2/2). \quad (21)$$

The product of prior P and likelihood defines the posterior distribution, $\pi = P\mathcal{L}$. We sample a five-dimensional space where $\{\log_{10} M_{\min}, \log_{10} M_1, \log_{10} M_0, \alpha, \sigma_{\log M}\}$ is the parameter vector. We use flat priors for all parameters; the ranges are $\log_{10} M_{\min} \in [11; 15]$, $\log_{10} M_1 \in [12; 17]$, $\log_{10} M_0 \in [8; 15]$, $\alpha \in [0.6; 2]$ and $\sigma_{\log M} \in [0.1; 0.6]$.

5. Results

5.1. Clustering measurements

Our measurements are presented in Figure 9, 10 and 11 for the full, red and blue samples, respectively. For clarity, we show three samples selected with the same luminosity threshold ($M_g - 5 \log h < -19.8$) and three samples covering the same redshift range ($0.4 < z < 0.6$). At the same luminosity and redshift, red samples are more clustered on small scales than the full sample, and blue galaxies are the least clustered. At a constant luminosity threshold, $w(\theta)$ increases with redshift for the full, red and blue samples.

On the left panels of Figs. 9 and 10, we plot our best fit $w(\theta)$ models. Model parameters and deduced quantities are shown in Tables B.1 (full) and B.2 (red). An example of sample distributions of best-fitting HOD parameters is given in Fig. C.1. Since the halo model aims to reproduce the clustering in threshold samples as a sum of contributions from central and satellite galaxies, both types of galaxy must be present. We presume that in general, central galaxies are brighter than their satellites, so that the latter assumption is valid for full samples selected by luminosity threshold. Also, we assume that red satellites are systematically associated with a (brighter) red central galaxy. On the contrary blue satellites may belong to a red central galaxy. For this reason, we defer fitting our model to our pure blue samples. We plan to address the blue population in a future work, perhaps considering separate halo occupation functions for both red and blue populations (Simon et al. 2009; Skibba & Sheth 2009).

In most cases, we find a good agreement between the data and our model, with χ^2/dof from 1.77 to 10.21 for full samples and from 1.20 to 6.21 for red samples. We report a few large χ^2 values in some full samples, mostly at high redshift and for bright luminosity thresholds, where the galaxy number density is small. We suspect systematic photometric redshift errors to be responsible for an underestimated clustering signal and systematic errors in the galaxy number density estimates (see Sec 3.2). Perplexity (see Sect. 4.3) is larger than 0.6 for most samples, indicating that our model accurately describes the observations.

5.2. Halo model fitting

In the right panels of Figs. 9 and 10 we show our best fit $N(M)$, the halo occupation function. First, we note that at a given redshift interval, M_{\min} , the average mass for which 50% of haloes contain one galaxy increases with luminosity. Secondly, we note that the evolution in $N(M)$ with redshift at a fixed luminosity is less pronounced than the evolution with luminosity at a fixed redshift, whereas the amplitude of $w(\theta)$ significantly decreases with redshift.

Halo masses M_1 and M_{\min} are tightly constrained, whereas M_0 , $\sigma_{\log M}$ and α are poorly constrained. M_{\min} and M_1 measurements are displayed in the top panels of Fig. 12 with re-

spect to luminosity threshold (M_g). For every sample, halo masses increase with luminosity. M_{\min} covers the range 10^{11} to $10^{14} h^{-1} M_{\odot}$. M_1 is significantly larger than M_{\min} , ranging from $10^{12.5}$ to $10^{16} h^{-1} M_{\odot}$. These trends are consistent with those found in both the local (Zehavi et al. 2010, 2005) and distant Universe studies (Zheng et al. 2007; Abbas et al. 2010). At high luminosity thresholds, where the number of objects is small, error bars on our best-fitting parameters are correspondingly larger. This trend is especially pronounced for α , where the small number of satellites in high mass haloes makes it difficult to constrain this parameter. However, we note α increases with luminosity threshold, suggesting that for massive haloes, bright galaxies will be more numerous than faint ones. $\sigma_{\log M}$ remains relatively stable for red galaxies (~ 0.3), as also seen in other data sets and numerical simulations. For the full sample, values are slightly larger (up to ~ 0.5 in some cases). Our fitted $\sigma_{\log M}$ values are slightly larger than previous works. We also made fits where values $\sigma_{\log M} > 0.6$ were allowed, and in some cases large values (> 1.0) were found. We therefore decided to impose the restriction that $\sigma_{\log M} < 0.6$. Sample incompleteness (due to errors in the photometric redshifts), leading to missing central galaxies, could explain such high $\sigma_{\log M}$ values.

At constant luminosity threshold, in both red and full samples, M_1 and M_{\min} decrease with increasing redshift. This effect is partially due to a selection effect caused by the dimming and reddening of stellar populations with time; for a constant luminosity cut one selects less and less massive galaxies at higher redshifts. We will return to this measurement in Sect. 6 where we attempt to separate this passive stellar evolution effect from the intrinsic stellar-to-halo mass evolution.

At faint luminosities, M_{\min} values are higher for red galaxies than for full samples. As we explained previously, one assumption of our model is that our red threshold samples have luminous red central galaxies. On the other hand, it is also possible, especially for fainter samples, that blue satellite galaxies inhabit haloes with red central galaxies. In such a case for the faint red galaxy sample, a red central galaxy will be seen ‘‘alone’’ in a more massive halo. This would also increase the halo mass estimate found for red central galaxies as compared to those in the full sample.

The bottom panels of Fig. 12 show M_1 with respect to M_{\min} for full and red samples. The parameters are strongly correlated and we fitted a power law (dashed line) in each redshift bin. For the full sample, we compare our results with a linear relation, $M_1 = 17 \times M_{\min}$ (dotted line), based on the coefficient observed in the SDSS ($z \sim 0.1$) by Zehavi et al. (2010). Our results agree with them in the lowest redshift bin, $z \sim 0.3$, but depart from this value at higher redshift.

We find that although M_1/M_{\min} relation does not vary significantly with luminosity threshold it does show some indications of evolution with redshift. We note that M_1/M_{\min} decreases with redshift for $M_{\min} \lesssim 10^{13} h^{-1} M_{\odot}$ and increases with redshift at higher mass. For red galaxies, M_1 is no longer proportional to M_{\min} but follows a power law. For $M_{\min} \sim 10^{12} h^{-1} M_{\odot}$, the ratio M_1/M_{\min} is ~ 12 (as compared to ~ 10 for luminous red galaxies found by Zheng et al. 2009) and shows a much smaller redshift evolution over the entire mass range.

Figure 13 shows the relationship between M_{\min} and the galaxy number density n_{gal} for red and full samples. As one would expect, progressively rarer objects are found in more massive haloes. We do not detect a significant evolution of the slope of our M_{\min} versus n_{gal} relationship with redshift. For red galaxies, we overplot the measurements from Brown et al. (2008) with which we are in excellent agreement, even though it covers

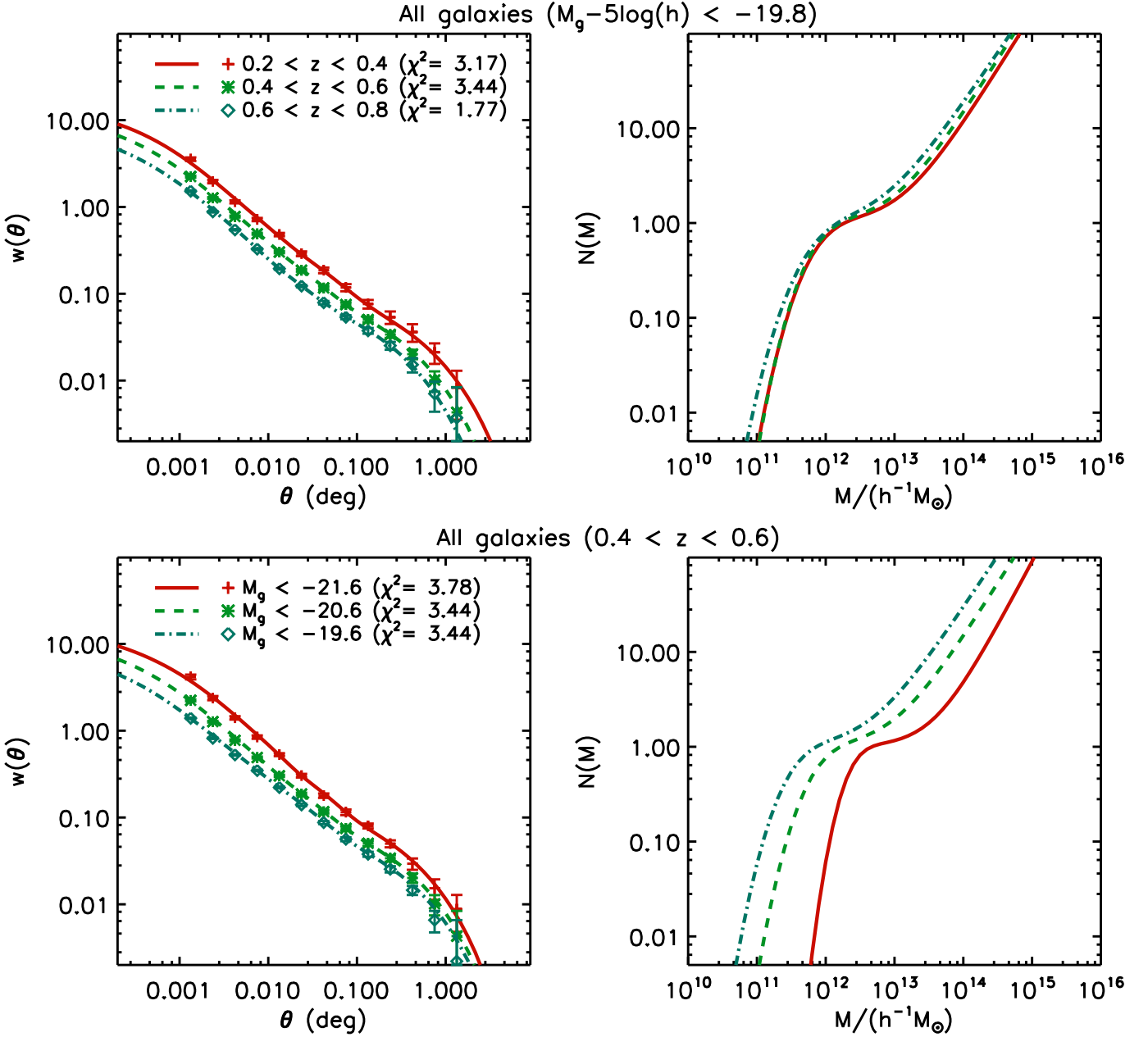


Fig. 9. $w(\theta)$ measurements (left) with their best fit models for all galaxies, and the resulting galaxy occupation function (right) with respect to halo mass. We illustrate the redshift evolution (top) in the luminosity threshold $M_g - 5 \log h < -19.8$, and the luminosity dependence (bottom) in the redshift range $0.4 < z < 0.6$.

a much smaller area. For the full galaxy sample we compare with SDSS measurements (Zehavi et al. 2010). The agreement is good at high surface densities; however we note a departure for low density samples. This difference suggests that at constant density, galaxies tend to reside in more massive haloes at low redshift ($z \sim 0$) than at higher redshift ($z > 0.6$). Part of this difference could be caused by systematic photometric redshift errors. As we discussed in Sec 3.2, bright samples may be contaminated by fainter objects, and the combined effect of higher density and lower clustering signal will result in reducing M_{\min} . In the most pessimistic case outlined in Sec 3.2, where the density estimate would be overestimated by a factor 3, $\log M_{\min}$ would be biased low by a few sigmas (up to ~ 0.5).

The relationship between M_{\min} and n_{gal} can be well approximated by a power law and we fitted galaxy samples at all redshifts simultaneously. We found:

$$M_{\min}^{\text{all}} = 10^{10.0} \times [n_{\text{gal}}^{\text{all}} / (h^3 \text{Mpc}^{-3})]^{-0.84} h^{-1} M_{\odot}, \quad (22)$$

for all galaxies and

$$M_{\min}^{\text{red}} = 10^{10.3} \times [n_{\text{gal}}^{\text{red}} / (h^3 \text{Mpc}^{-3})]^{-0.74} h^{-1} M_{\odot}, \quad (23)$$

for red galaxies.

6. Discussion

The key issue we would like to address is to understand how galaxy formation and evolution depend on the properties of the

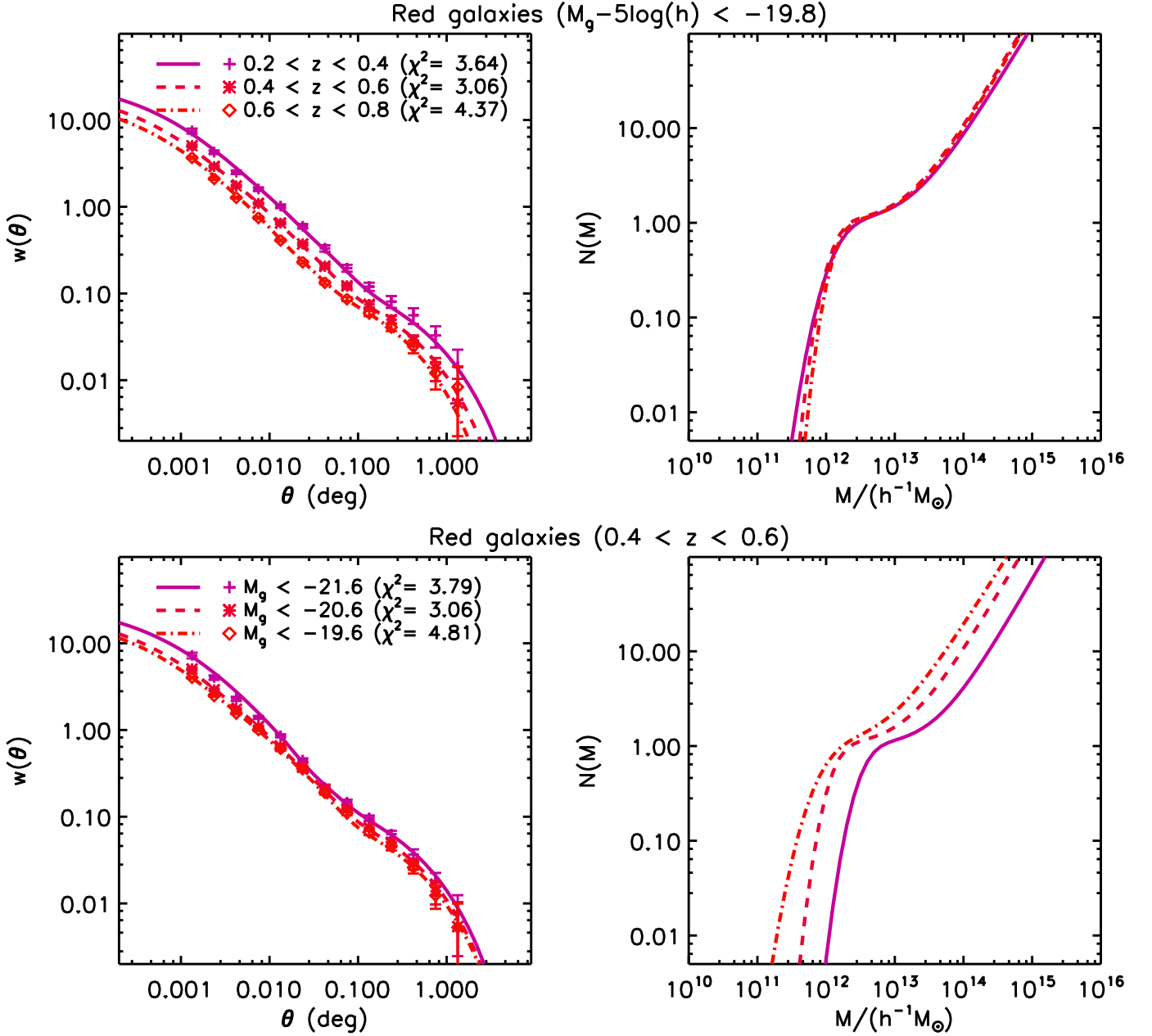


Fig. 10. $w(\theta)$ measurements (left) with their best fit models for red galaxies, and the resulting galaxy occupation function (right) with respect to halo mass. We illustrate the redshift evolution (top) in the luminosity threshold $M_g - 5 \log h < -19.8$, and the luminosity dependence (bottom) in the redshift range $0.4 < z < 0.6$.

underlying dark matter haloes. Ideally, to relate halo masses to their stellar content, one would select our samples by stellar mass. However, stellar mass estimates computed from our five-band optical data alone would suffer from large uncertainties. Keeping this limitation in mind, we adopt an intermediate approach where we determine an empirical relation to convert the observed luminosity threshold of each sample to an approximately mass-selected sample using a reference sample with accurate stellar masses. This method allows to transform luminosities into masses and provides an estimate of the likely errors in such a transformation.

6.1. Transforming to stellar mass threshold samples

As a consequence of passive stellar evolution, the characteristic rest-frame M_g -band luminosity of a given galaxy type evolves significantly over the redshift range $0.2 < z < 1.2$ (Ilbert et al. 2005; Zucca et al. 2006; Faber et al. 2007).

In order to account for these effects, we have established a simple approximation to relate stellar mass and luminosity based on COSMOS 30-band photometry (Ilbert et al. 2010). We used the COSMOS B -band luminosities in order to be as close as possible to our M_g -band selected samples. Red galaxies are selected as $M(NUV) - M_R > 3.5$ and blue galaxies as $M(NUV) - M_R \leq 3.5$. We then fit the stellar mass-to-luminosity ratio with power-law functions as function of redshift between

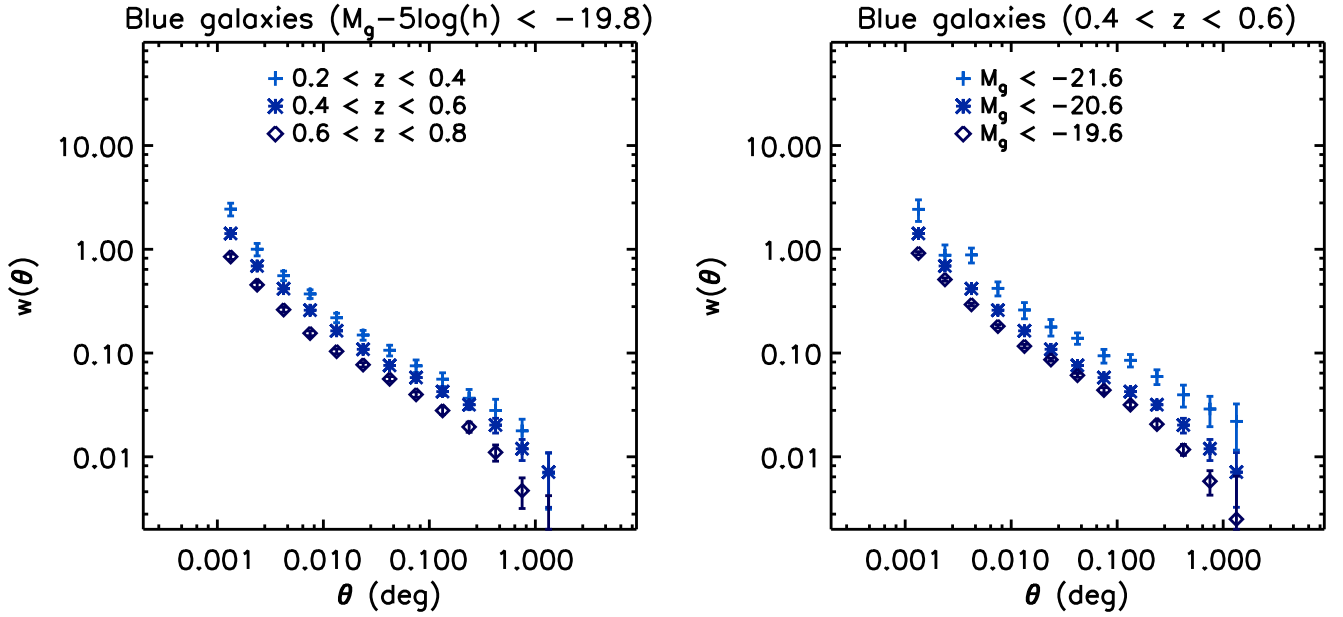


Fig. 11. $w(\theta)$ measurements for blue galaxies. We illustrate the redshift evolution (left) at the luminosity threshold $M_g - 5 \log h < -19.8$, and the luminosity dependence (right) in the redshift range $0.4 < z < 0.6$.

$z = 0$ and $z = 1.5$ for five stellar mass bins from $10^{9.0}$ to $10^{11.5}$. These results are displayed in Fig. 14.

Due to the ageing of stellar populations, the average stellar mass-to-light ratio increases with time. For red galaxies, the slope depends weakly on stellar mass at intermediate masses ($10^{9.5} - 10^{11.5} h^{-1} M_\odot$) and ranges from -0.56 to -0.44 . The slope is steepest in the lowest mass bin, but the number of objects in this bin is small. Based on these results we adopt the following relationship for the red galaxy population:

$$\log\left(\frac{M_{\text{star}}}{L_B}\right)_{\text{red}} = \log\left(\frac{M_{\text{star}}}{L_B}\right)_{\text{red}, z=0} - (0.5 \pm 0.1)z, \quad (24)$$

where the 0.1 error accounts for the scatter between mass bins. This evolution is consistent with the luminosity function evolution measured for red galaxies in the DEEP2 and COMBO17 surveys (Faber et al. 2007; Willmer et al. 2006), where the characteristic absolute magnitude M_B^* decreases by about 1.2–1.3 mag per unit redshift ($M_B \propto -2.5 \log L_B$).

For the blue sample, the evolution in redshift is more pronounced than for the red sample, as also seen in DEEP2 (Willmer et al. 2006) and VVDS (Zucca et al. 2006). Unfortunately, in this case, the slope depends on stellar mass, ranging from -0.69 to -1.10 in the mass range $[10^{9.5}, 10^{11.5}]$, and has a larger scatter. The full sample is dominated by blue galaxies at faint luminosities but by red galaxies at bright luminosity (see Fig. 3). Therefore a simple relation between luminosity and stellar mass valid for all luminosities cannot be obtained. For the full sample we choose to apply the same correction as for the red sample. As blue galaxies evolve more rapidly than red ones such a correction underestimates the expected evolution of the full samples at faint luminosity and therefore cannot be used to construct stellar-mass selected samples. In the following sections, we discuss how our results depend on this correction.

In the following sections we use these expressions to calculate “corrected” luminosities, denoted as L' . Note that these corrections are equivalent to shifting observed galaxy luminosities to redshift $z = 0$. Our results are displayed as a function

of relative luminosity threshold L'/L_* , where L_* corresponds to $M_g^* - 5 \log h = -19.81$ and -19.75 for the full and red samples, respectively, measured in the local Universe (Faber et al. 2007, and references therein). It is also worth mentioning that if galaxies would experience a pure passive luminosity evolution with cosmic time, this would result in constant HOD parameters for a given L'/L_* as function of redshift. However, deduced parameters (galaxy bias, mean halo mass and satellite fraction) are expected to vary due to the evolving halo mass function and halo bias (see Eqs. 13–17).

6.2. The stellar-to-halo mass relationship

In our model, M_{min} represents the hosting halo mass for central galaxies whose median luminosity equals the luminosity threshold of the sample (see Sect. 4.1). The ratio L'/M_{min} is therefore the ratio of luminosity to dark matter mass for central galaxies. Zehavi et al. (2010) showed that the relation between central galaxy luminosity L'_c (corresponding to our L') and the halo mass could be approximated by:

$$\frac{L'_c}{L_*} = A \left(\frac{M_h}{M_t}\right)^{\alpha_M} \exp\left(-\frac{M_t}{M_h} + 1\right), \quad (25)$$

where A , α_M and M_t are free parameters and M_h represents M_{min} or M_1 .

This expression encapsulates the idea that there exists a “transition halo mass” ($\sim M_t$) where the ratio of central galaxy luminosity to dark matter halo mass reaches a maximum. This transition mass represents the halo mass for which baryons have been most efficiently converted into stars until the time of observation, resulting from past and on-going star formation over cosmic history.

We fit Eq. 25 for full and red samples for each redshift slice. For our two highest redshift bins where the number of points are less than the number of free parameters, we perform a simultaneous fit over both redshift bins. Results are plotted in Fig. 15 and best-fitting parameters given in Table C.6.

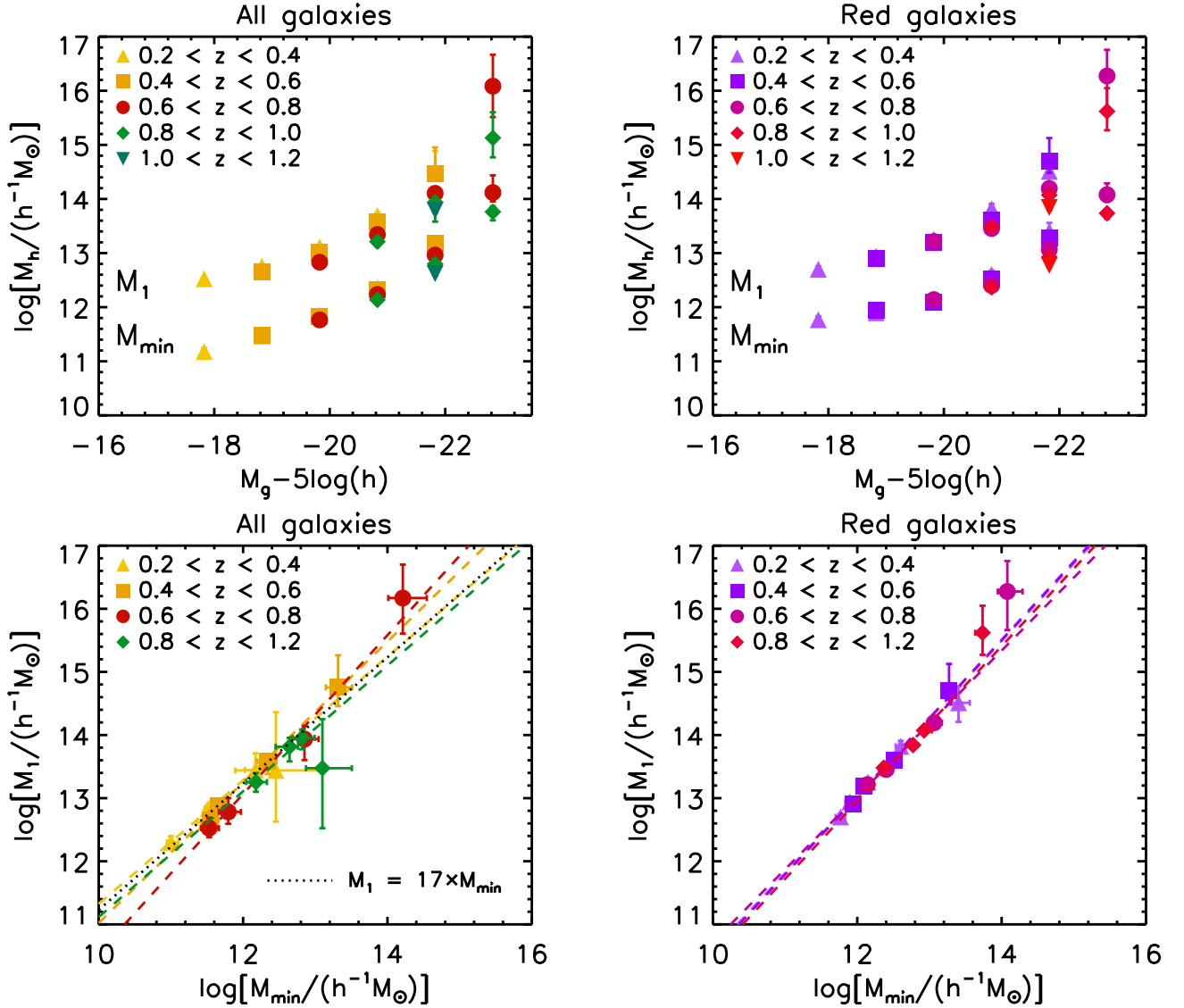


Fig. 12. Top panels: halo mass estimates M_{\min} and M_1 for all (left) and red (right) galaxy samples as function of luminosity threshold (M_g). Bottom panels: M_1 versus M_{\min} in different redshift bins. The dotted lines represent a linear relation and the dashed lines are a power-law fit to M_1 versus M_{\min} in each redshift bin.

In our lowest redshift bin ($0.2 < z < 0.4$), our full sample has best-fitting parameters slightly different than in the SDSS (Zheng et al. 2007; Zehavi et al. 2010), $A = 0.20 \pm 0.01$ (compared to 0.32) and $M_t = 2.24 \pm 0.1 \times 10^{11} h^{-1} M_\odot$ (compared to 3.08×10^{11}). We note that the difference is likely due to the different selection (M_r in the SDSS). At high luminosities, the difference with their relation increases. For a given luminosity, we find lower halo masses, $L_c \propto M^{0.5 \pm 0.01}$, compared to $L_c \propto M^{0.26-0.28}$, which follows the trends observed in Fig. 13, and might be due to contaminated samples at low density. In the red sample, we measure $L_c \propto M^{0.31 \pm 0.16}$, whereas Zheng et al. (2009) found $L_c \propto M^{0.5}$ for luminous red galaxies in the SDSS. Both M_{\min} and M_1 increase with redshift for the full sample. The dependence with redshift is weak for red galaxies, although we detect a slight increase in the very highest redshift bins.

For the full sample we assumed a correction based on the evolution of the stellar mass-to-luminosity ratio of red galaxies (Eq. 24). As the characteristic luminosity of blue galaxies evolves more rapidly than red ones and as the faint sample is

dominated by blue galaxies a legitimate concern is the dependence of our results on our corrections to stellar mass. Several corrections assuming the blue galaxy luminosity evolution (using slopes given in Fig. 14) were tested. If a larger correction is applied, M_1 and M_{\min} show a similar but more pronounced trend. For this reason we conclude that the increase of halo mass parameters with redshift for the full sample is a robust result (although the exact amount of evolution observed depends on the correction we apply).

6.3. Redshift evolution of the SHMR and comparison with literature values

To study the redshift evolution of the stellar-to-halo mass ratio, we consider the relationship between corrected galaxy luminosity and the host halo mass from Eq. 25:

$$\frac{L'_c}{M_h} = A \frac{L_*}{M_t} \left(\frac{M_h}{M_t} \right)^{\alpha_M - 1} \exp\left(-\frac{M_t}{M_h} + 1\right), \quad (26)$$

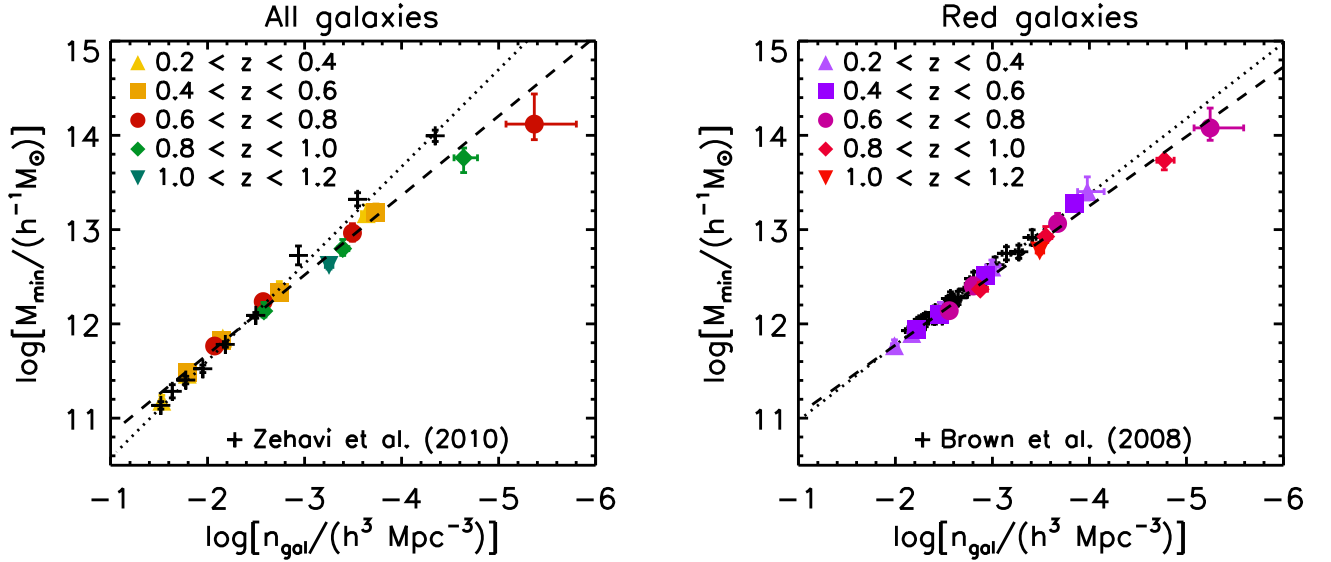


Fig. 13. M_{\min} as a function of galaxy number density for all (left) and red (right) galaxies. The dashed line in each panel represents a power law fit to the data, and the dotted line represents a power law fit to the results given in Brown et al. (2008) (red galaxies) and in the SDSS by Zehavi et al. (2010) (all galaxies). We converted M_{200} halo masses to virial masses M_{vir} when necessary.

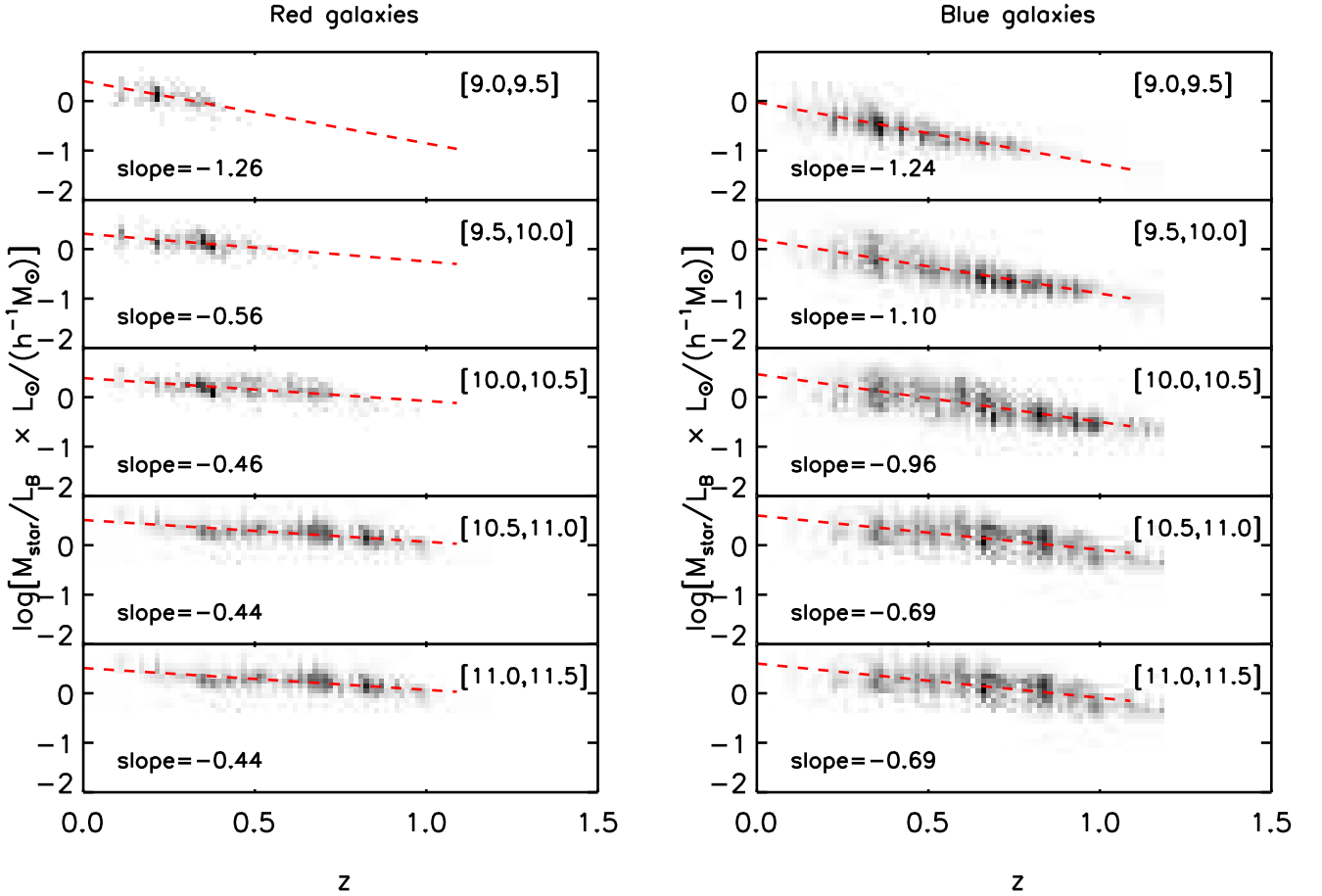


Fig. 14. Stellar mass-to-luminosity relations for red (left) and blue (right) galaxies, as a function of stellar mass and redshift as measured in the COSMOS survey (Ilbert et al. 2009). Each panel shows a separate slice in stellar mass. Samples are fitted with a power law (dashed line).

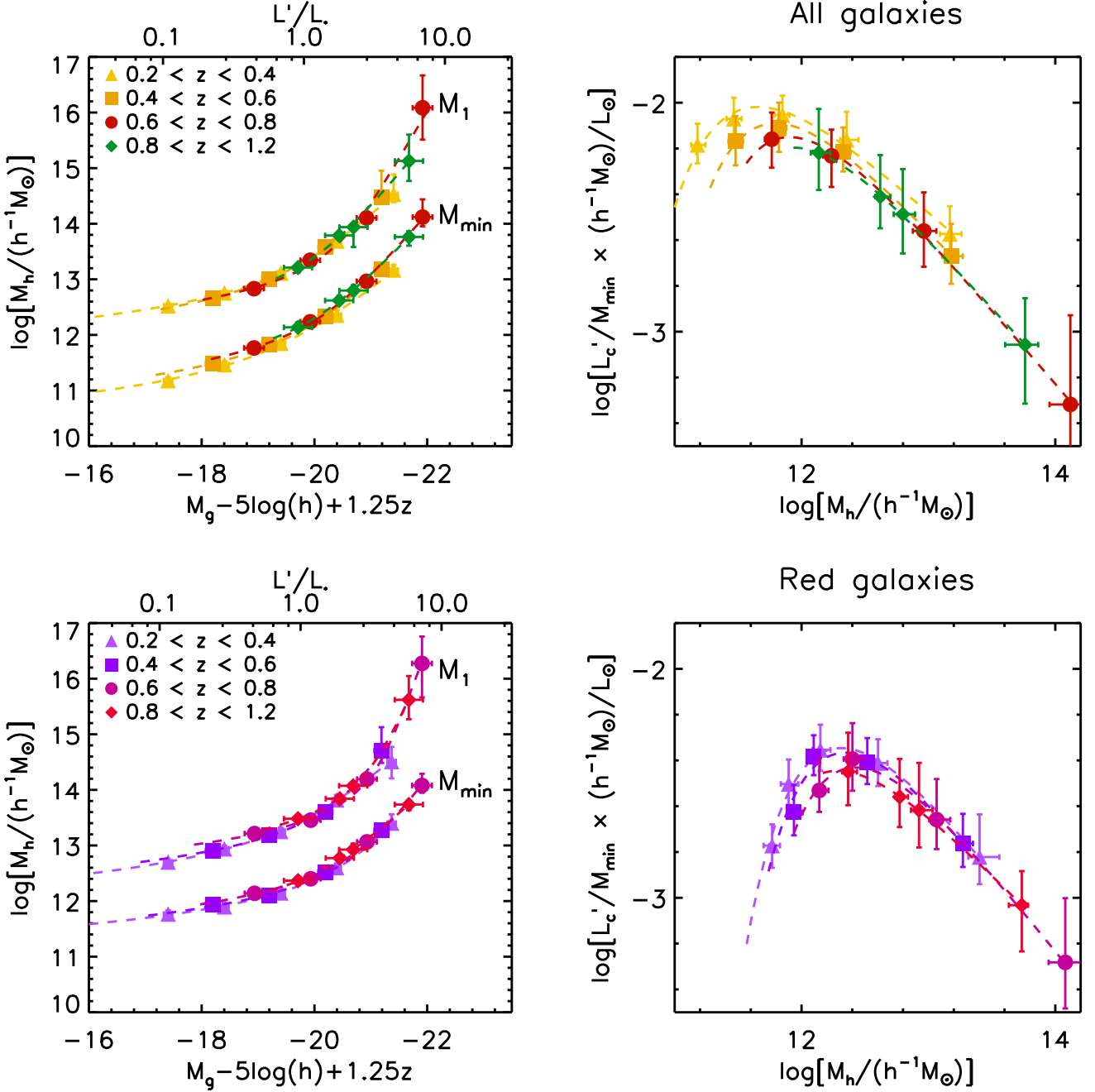


Fig. 15. Left panels: halo mass estimates M_{\min} and M_1 for all (top) and red (bottom) galaxy samples, as function of luminosity threshold, corrected for passive redshift evolution to approximate stellar mass selected samples. The dashed lines correspond to Eq. 25. Right panels: light-to-halo mass ratios L'_c/M_{\min} (Eq. 26 with identical parameters as those fitted with Eq. 25) as function of halo mass.

where the maximum is located at:

$$M_h^{\text{peak}} = \frac{M_t}{1 - \alpha_M}. \quad (27)$$

The right panels of Fig. 15 show the L'_c/M_{\min} relation for full and red samples as function of halo mass fitted by Eq. 25. Best fitting parameters are listed in Table C.6. For less massive haloes, the relative stellar mass content increases with halo mass and reaches a maximum around $M_{\min} \sim 10^{12} h^{-1} M_{\odot}$. In more massive haloes, the stellar-

to-halo mass ratio sharply decreases. Our measurements are consistent with recent observations measuring the stellar-to-halo mass ratio as function of halo mass (Mandelbaum et al. 2006; Zheng et al. 2007; Foucaud et al. 2010; Zehavi et al. 2010; More et al. 2011; Wake et al. 2011; Leauthaud et al. 2011b), and “abundance-matching” techniques based on N -body simulations (Conroy & Wechsler 2009; Moster et al. 2010; Behroozi et al. 2010). Similar trends are found in semi-analytic simulations (see, for e.g., Somerville et al. 2008), in which physical processes (such as supernovae and AGN feedback) preventing gas

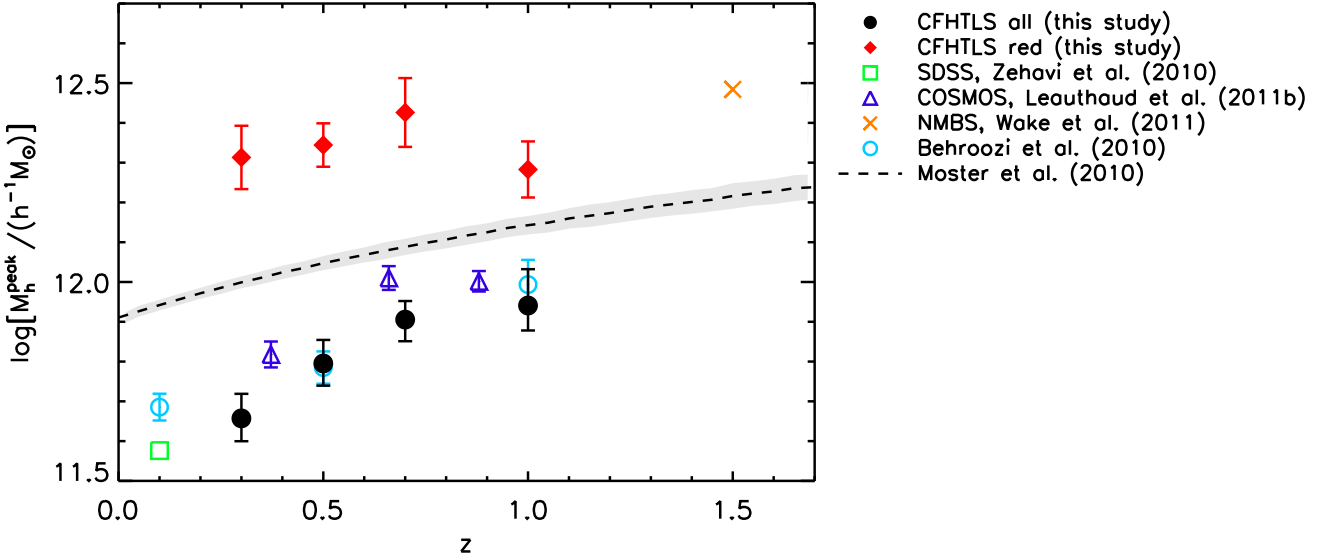


Fig. 16. Position of the peak M_h^{peak} corresponding to $\max(L'_c/M_{\text{min}})$ for the full (filled circles) and red (filled diamonds) samples as function of redshift. Error bars are derived from the nearest data point to the peak. We compare our results with measurements in SDSS (Zehavi et al. 2010), in COSMOS (Leauthaud et al. 2011b) and in the NEWFIRM Medium Band Survey (NMBS, Wake et al. 2011). We convert M_{200} halo masses (corresponding to a sphere with overdensity 200 times the background density) into virial masses M_{vir} (our definition) using the method described in Appendix C of Hu & Kravtsov (2003). We also display numerical predictions based on abundance-matching method from Behroozi et al. (2010) and Moster et al. (2010), where the shaded region shows the $1-\sigma$ uncertainty.

from cooling and quenching star formation must be taken into account to match observations.

Our measured peak values M_h^{peak} (Eq. 27, with error bars from the nearest data points) are plotted as a function of redshift in Fig. 16. Comparing to literature measurements at lower redshifts, the peak stellar-to-halo mass relation is $M_h^{\text{peak}} = 4.54 \times 10^{11} h^{-1} M_\odot$, similar to the local Universe value ($\approx 4.2 \times 10^{11} h^{-1} M_\odot$, Zehavi et al. 2010). For our full sample, the peak location gradually increases with redshift.

At higher redshifts, we compare our measurements with those of Moster et al. (2010) and Behroozi et al. (2010). These authors derived the stellar-to-halo mass relation using an abundance-matching technique, linking dark matter halo mass functions from N -body simulations with observed galaxy stellar mass functions. Moster et al. (2010) estimate the redshift evolution of the stellar-to-halo mass ratio (their Table 7) and from this we derived analytically the position of the peak, as well as associated errors. Values from Behroozi et al. (2010) at redshift 0.1, 0.5 and 1.0 were supplied to us (P. Behroozi, private communication). Both Moster et al. and Behroozi et al.’s measurements are based primarily on galaxy stellar mass measurements covering relatively small areas (a few hundred square arcminutes). Our full sample is in excellent agreement with Behroozi et al. but differs significantly from Moster et al., although in both cases the two data sets show the same general trend: M_h^{peak} shifts gradually towards higher halo masses at higher redshift. The Moster et al. points do not seem to agree very well with most observations and moreover overestimate the position of the peak at low redshift.

Measurements in the COSMOS field are also shown (Leauthaud et al. 2011b); their points are in general larger than most measurements, with the exception of Moster et al.. It has already been noted that there are several rich structures in the COSMOS field (McCracken et al. 2007; Meneux et al. 2009;

de la Torre et al. 2010) which lead to higher correlation functions, especially at $z \sim 0.8$; cosmic variance could perhaps be the origin of this discrepancy.

For red galaxies, the peak is at larger halo masses, $M_h^{\text{peak}} = 20.6 \times 10^{11} h^{-1} M_\odot$. This is not surprising as M_{min} is larger for red galaxies at faint luminosities. The red galaxy peak position undergoes only little evolution to $z \sim 1$. Our intermediate-redshift red galaxy points are consistent with higher redshift measurements (Wake et al. 2011); these authors used a near-infrared survey to select galaxies by stellar mass, and we would expect their selection to be dominated by red galaxies.

The results presented here represent the first time a single data set covering a statistically significant area has been used to derive the evolution of the peak position as a function of redshift and galaxy type in a self-consistent manner. The peak position, M_h^{peak} , can be interpreted as representing the halo mass at which the stellar mass content is most efficiently accumulated in haloes, either by star formation or merger processes. The movement of this peak towards higher halo masses at higher redshifts is consistent with a picture in which the sites of efficient stellar mass growth migrate from low-mass to high-mass haloes at higher redshift. This “anti-hierarchical” evolution, frequently referred to as “halo downsizing”, resembles closely the scenario first sketched by Cowie et al. (1996), in which the maximum luminosity of galaxies undergoing star-formation declines steadily to the current day. Conversely, the fact that we observe constant transition masses for the red population suggests that the stellar-to-halo mass ratio does not significantly evolve in haloes with mass $\sim 10^{12} h^{-1} M_\odot$ and supports observations that intermediate-mass red galaxies have experienced no significant stellar mass growth by star formation since $z \sim 1.2$.

We tried several corrections to convert to stellar mass thresholds based on the slope measured for blue galaxy evolution

(see Fig. 14), and we found that the peak luminosity depends only weakly on these corrections. Only the highest-redshift point changes by around one sigma if we apply the extreme “blue galaxy” correction to our full sample. For this reason we conclude that the increase of M_h^{peak} with redshift for the full sample is a robust result.

6.4. Redshift evolution of halo satellite fraction

The fraction of galaxies which are satellites in a given dark matter halo is a sensitive probe of the past evolutionary history of the halo which may be modified by processes such as major mergers (which can decrease the satellite fraction with time) or environmental effects which operate primarily to reduce the number of satellites, such as, but not limited to, the restriction of gas supply or “strangulation” (Larson et al. 1980) or ram-pressure stripping (Gunn & Gott 1972). Satellite galaxies may also merge with their central galaxy. Observational evidence based on pair fraction measurements and theoretical studies using numerical simulations now shows that mergers seem to play a significant (although not dominant) role in the evolution of massive galaxies since $z \sim 1$ (White et al. 2007; Wang & Jing 2010; van Dokkum et al. 2010; Robaina et al. 2010; Zehavi et al. 2011). Our objective in this section is to see if measurements of the satellite fraction can provide new insights into the evolutionary history of haloes.

The left panels of Figure 17 show the satellite fraction f_s , computed using Eq. 17. As before, each sample is converted to an approximately mass-limited sample by “correcting” for passive luminosity evolution (see Sect. 6.1). At all redshifts, as the luminosity threshold increases, corresponding to higher mass thresholds, the satellite fractions become progressively smaller. The similarity between the full and red samples is simply a consequence of the dominance of red galaxies at bright luminosity thresholds.

At fainter luminosity thresholds, the satellite fraction rises and eventually reaches a plateau. This effect can be understood by considering both the halo mass function and the halo occupation function: the increase of the latter with decreasing luminosity threshold (see Fig. 8) is rapidly compensated by a sharp decrease in massive halo number density, so that faint galaxies are preferentially central galaxies in smaller haloes rather than being satellites in more massive haloes.

We compare our results with satellite fractions found in SDSS ($z \sim 0.1$) and DEEP2 ($z \sim 1$). To explore a complete range in redshift and luminosity, we extrapolate our best-fitting HOD parameters measured in the redshift range $0.4 < z < 0.6$; that is, at a given luminosity, we keep the HOD parameters fixed and compute Eq. 17 at different redshifts. The choice for this intermediate redshift range is motivated by the fact that it contains the most robust photometric redshift estimates and our measured points span a large range in luminosity. Each HOD parameter set is constructed from M_{min} and M_1 interpolated in luminosity using Eq. 25 with best-fitting parameters given in Table C.6. For red galaxies, M_0 is set to $M_{\text{min}}/100$, $\sigma_{\log M}$ is fixed to 0.3 and $\alpha = 1.1$ for $L < L_*$ or $\alpha = 1.4$ otherwise. For all galaxies, M_0 is set to $M_{\text{min}}/100$, $\sigma_{\log M} = 0.4$ and $\alpha = 1.1$ for $L < L_*$, and $\sigma_{\log M} = 0.3$ and $\alpha = 1.3$ for brighter luminosity thresholds.

In the middle panels of Fig. 17 we compare our extrapolated satellite fractions for all galaxies (in dashed lines) with results derived from SDSS and DEEP2, using a HOD analysis similar to ours (Zheng et al. 2007). Our satellite fractions are consistent with these measurements at both redshifts, although we slightly

over-predict satellite fractions at $z \sim 0.1$ for samples brighter than $\sim 0.5L_*$. An overall increase of a factor of two is measured between $z \sim 1$ and $z \sim 0$ for samples with $L > L_*$; we note that this value is lower than the factor of three from $z \sim 0.5$ to $z \sim 0$ measured in the VVDS (Abbas et al. 2010).

We fit the HOD parameters at each redshift independently. Therefore, our model provides us with “snapshots” of the occupation function at various epochs. If any physical process had played a significant role in reducing the satellite number density between $z \sim 1$ and $z \sim 0$, our fixed-HOD model calibrated at $z \sim 0.5$ would over-predict the satellite fraction observed in the local Universe and under-predict the satellite fraction at redshift one. The excellent match found for bright luminosity threshold samples shows that our satellite fraction measurements follow closely a redshift-independent HOD. Since a redshift evolution of the merging rate would change the occupation function, we therefore conclude that our measurements imply a constant merging rate since $z \sim 1$, which confirms the constant (albeit minor) role of merging for intermediate-mass galaxies (e.g., Bundy et al. 2009). As outlined by White et al. (2007), if halo merging was not followed by galaxy merging, we would observe an increase of halo masses at constant galaxy density. Instead, no redshift evolution of the $M_{\text{min}}-n_{\text{gal}}$ relationship (see Fig. 13) supports a scenario with constant galaxy merging with time.

We compare our red satellite fraction with the galaxy-galaxy lensing analysis from SDSS (Mandelbaum et al. 2006). These samples were constructed from luminosity slices, rather than the threshold samples we use here. We then computed the number of satellites per luminosity bin as the difference of satellite fractions between two threshold samples:

$$f_s^{\text{bin}} = \frac{f_s^{\text{thres2}} n_{\text{gal}}^{\text{thres2}} - f_s^{\text{thres1}} n_{\text{gal}}^{\text{thres1}}}{n_{\text{gal}}^{\text{thres2}} - n_{\text{gal}}^{\text{thres1}}}. \quad (28)$$

As we found for the full galaxy sample, the good agreement supports a non-evolving HOD from $z = 0.5$ to $z = 0$.

Finally, in the right panels of Fig. 17, we provide extrapolated satellite fractions as function of redshift for several luminosity thresholds. It is interesting to examine our results in the context of recent results studying the role of satellite galaxies in galaxy formation and evolution (Peng et al. 2010, 2011). These works show measurements from numerical simulations and SDSS group catalogues which indicate that the fraction of satellites *at a fixed overdensity* is independent of halo mass and redshift. In this context, the growth of the satellite fraction we observe is simply a consequence of average growth in overdensity in rich structures between $z \sim 1$ to $z \sim 0$, reflecting the growing importance of environment at low redshift.

6.5. Galaxy bias

We compute the galaxy bias (Eq. 13) from our best-fitting HOD parameters. We fit the bias measurements as function of luminosity and redshift, adopting a linear relationship (Norberg et al. 2001):

$$b_g(> L') = a_{\text{bias}} + b_{\text{bias}} \frac{L'}{L_*}, \quad (29)$$

where L' represents the corrected luminosity (computed from Eq. 24 for the full and red samples). We fit the two highest redshift bins together ($0.8 < z < 1.0$, $1.0 < z < 1.2$), as only one point is available in the highest one. Results are plotted in Fig. 18 and best-fitting parameters are given in Table C.7.

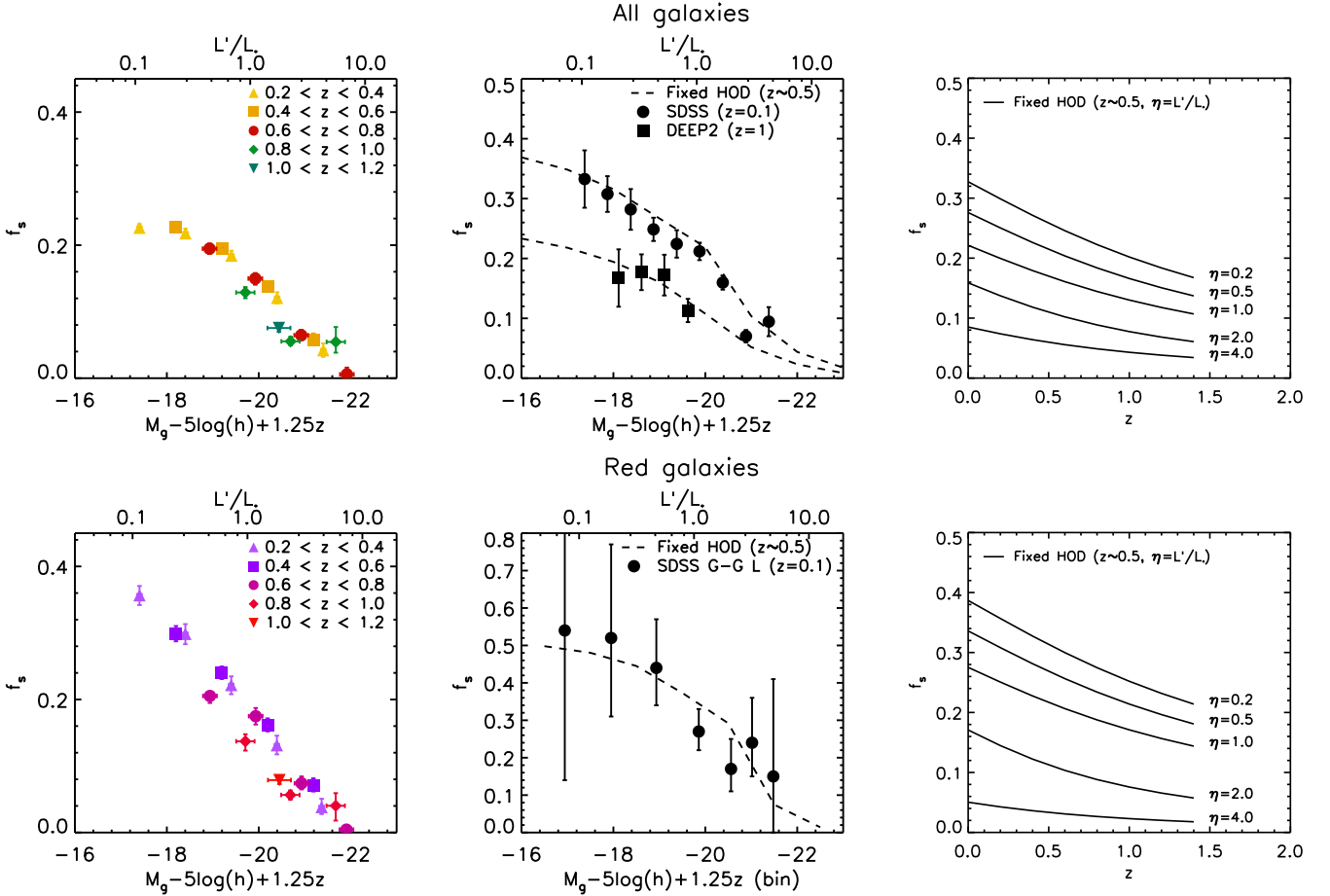


Fig. 17. Satellite fractions as function of luminosity and redshift, for all and red samples (top and bottom panels). The left panels show the measured satellite fraction as function of corrected luminosity. Dashed lines in the middle panels show satellite fractions extrapolated in redshift, based on our HOD parameters measured in the redshift range $0.4 < z < 0.6$. We compare our results with the literature for all galaxies at $z = 0.1$ and $z = 1.0$ (top, Zheng et al. 2007) and with galaxy-galaxy lensing estimates at $z = 0.1$ (bottom, Mandelbaum et al. 2006) for red galaxies. In the right panels we provide values extrapolated in redshift for several L'/L_* ratios.

This parameterised bias relation reproduces our results best at $z < 0.6$. At a fixed redshift, for $L'/L_* < 1$, the bias is a very weak function of luminosity; for $L'/L_* > 1$, bias depends strongly on luminosity. For the faint, low-redshift full-sample galaxies, dominated by more weakly-clustered bluer galaxies, $b \sim 1$; the faint red samples have higher biases, of around $b \sim 1.5$. These results are a consequence of the higher clustering amplitudes observed for red samples compared to the full galaxy sample for $L'/L_* < 1$, and are consistent with similar measurements made by smaller surveys at intermediate redshifts (see for example Meneux et al. 2009).

The right panels of Fig. 18 illustrate the redshift evolution of the bias at several luminosity thresholds. We compare our results (solid lines) derived from Eq. 29 with a galaxy bias evolution computed using a constant set of HOD parameters evaluated at $z \sim 0.5$ (see Sec 6.4). The slight difference observed between the measured HOD and the HOD fixed model at $z = 0.5$ comes from the fact that we set $\sigma_{\log M}$ to 0.3 and α to 1.0. For the full galaxy population, a model with fixed HOD parameters provides an excellent fit to the observations, with more luminous objects undergoing a much more rapid evolution in bias. For the red galaxy population, there is some evidence that the bias evolution is more rapid than the model with fixed HOD parameters.

6.6. Mean halo mass

From Eq. 15 we compute the average dark matter halo mass for each of our samples. Note that this quantity represents the halo mass averaged over samples containing galaxies above the luminosity threshold and differs from M_{\min} which represents the halo mass for central galaxies whose luminosity corresponds to the luminosity threshold. As before, after correcting luminosities to a corresponding stellar mass threshold, we fit the mean halo mass as function of luminosity and redshift, adopting a linear relation:

$$\log \langle M_{\text{halo}} \rangle (> L') = a_{\text{halo}} + b_{\text{halo}} \frac{L'}{L_*}, \quad (30)$$

where L' is the corrected luminosity. Once again, we fit the two highest redshift bins simultaneously. Results are displayed in Fig. 19 and best-fitting parameters are given in Table C.7.

For fainter samples with $L' < 2L_*$ the mean halo mass gradually increases with luminosity and changes more rapidly for brighter samples. Faint red galaxy samples on average have higher halo masses than the full sample which is dominated by bluer galaxies at these luminosities. This is consistent with a sce-

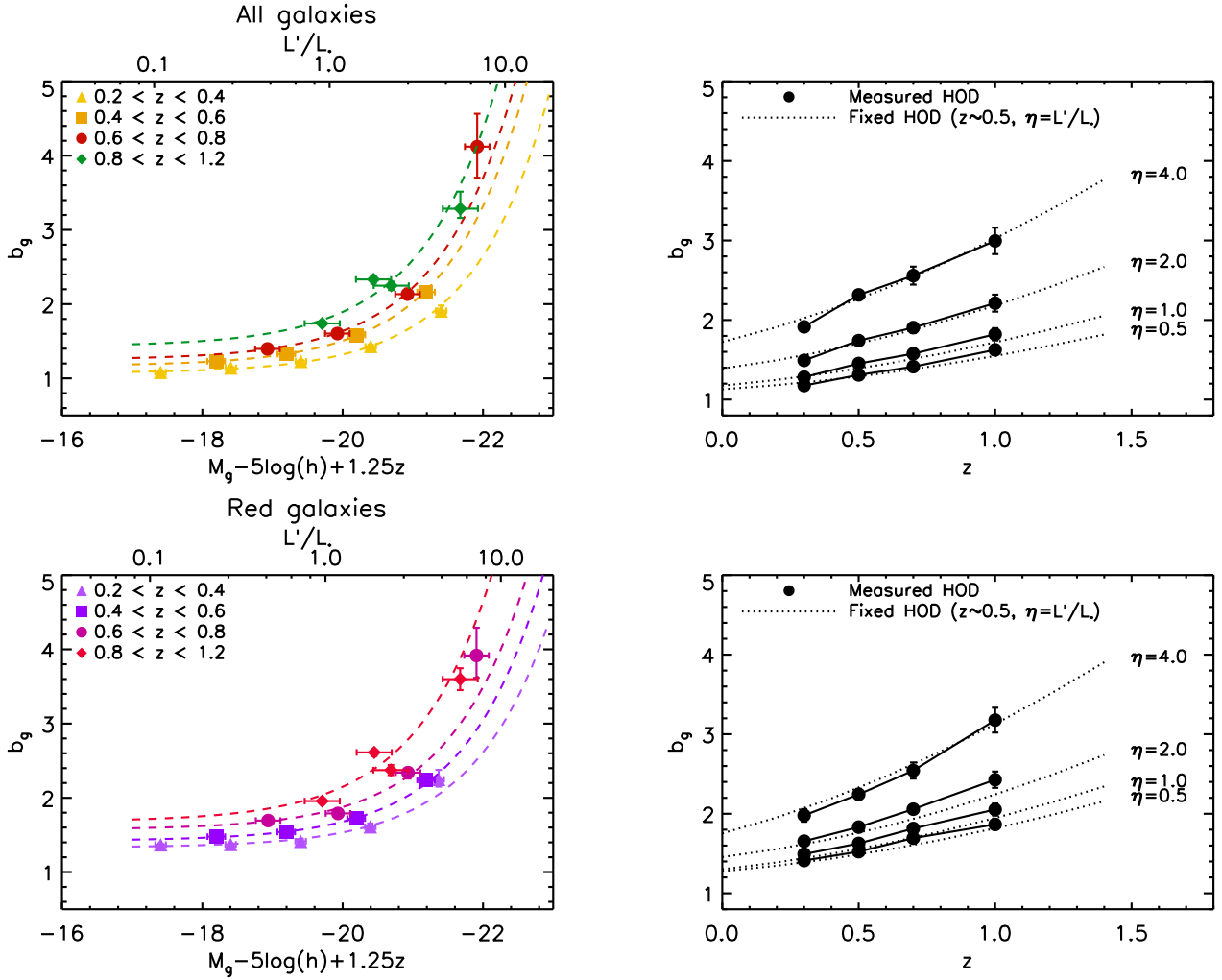


Fig. 18. Galaxy bias as function of luminosity and redshift. Left panels: bias for full and red samples (top and bottom panels) as function of corrected luminosity threshold L' . The dashed line represents Eq. 29. Right panels: computed bias for several luminosity threshold samples L'_* as function of redshift. Error bars were derived from the parametric form shown on the left (dashed line), whereas the dotted lines show the bias evolution computed from our model, assuming a redshift-independent HOD parameter set.

nario in which high numbers of red satellite galaxies in faint samples reside in more massive haloes.

In the right panels of Fig. 19 we show the redshift evolution of the mean halo mass for several luminosity thresholds. As before, we compare mean halo masses derived from our measured HOD parameters (solid lines) with a model of fixed halo model parameters set measured at redshift 0.5. At all luminosities, the mean halo mass decreases with increasing redshift. This is an indication of the fact that haloes merge through cosmic history and the effective mass of haloes grows with time. In bright samples, the mean halo mass evolves more slowly than in fainter ones. At low luminosity thresholds and high redshifts, both the full sample and red galaxy sample deviate slightly from our model with fixed HOD parameters.

7. Summary and conclusions

We have made one of the most precise measurements to date of the angular correlation function w and its dependence on luminosity and rest-frame colour from $z \sim 0$ to $z \sim 1$. Our measurements were constructed from a series of $i' < 22.5$ volume-

limited samples, containing $\sim 3 \times 10^6$ galaxies in four independent fields. These samples were created using accurate five-band photometric redshifts in the CFHTLS Wide survey calibrated with $\sim 10^4$ spectroscopic redshifts. A cross-correlation analysis showed consistency with a relatively small contamination fraction arising from scatter between photometric redshift bins.

We interpreted these measurements in the framework of a model in which the number of galaxies inside each dark matter halo is parametrised by a simple analytic function (the halo occupation distribution) with five adjustable parameters. In this model, central and satellite galaxies are treated separately. For each galaxy sample, we performed a full likelihood analysis and explored model parameter space using an efficient Population Monte Carlo analysis. The very large survey volume probed by the CFHTLS Wide allowed us to place robust constraints on the redshift evolution of the halo model parameters, and make accurate estimates for halo properties of many different galaxy samples over more than two orders of magnitude in luminosity and three orders of magnitude in halo mass, from 10^{12} to $10^{15} (h^{-1} M_\odot)$.

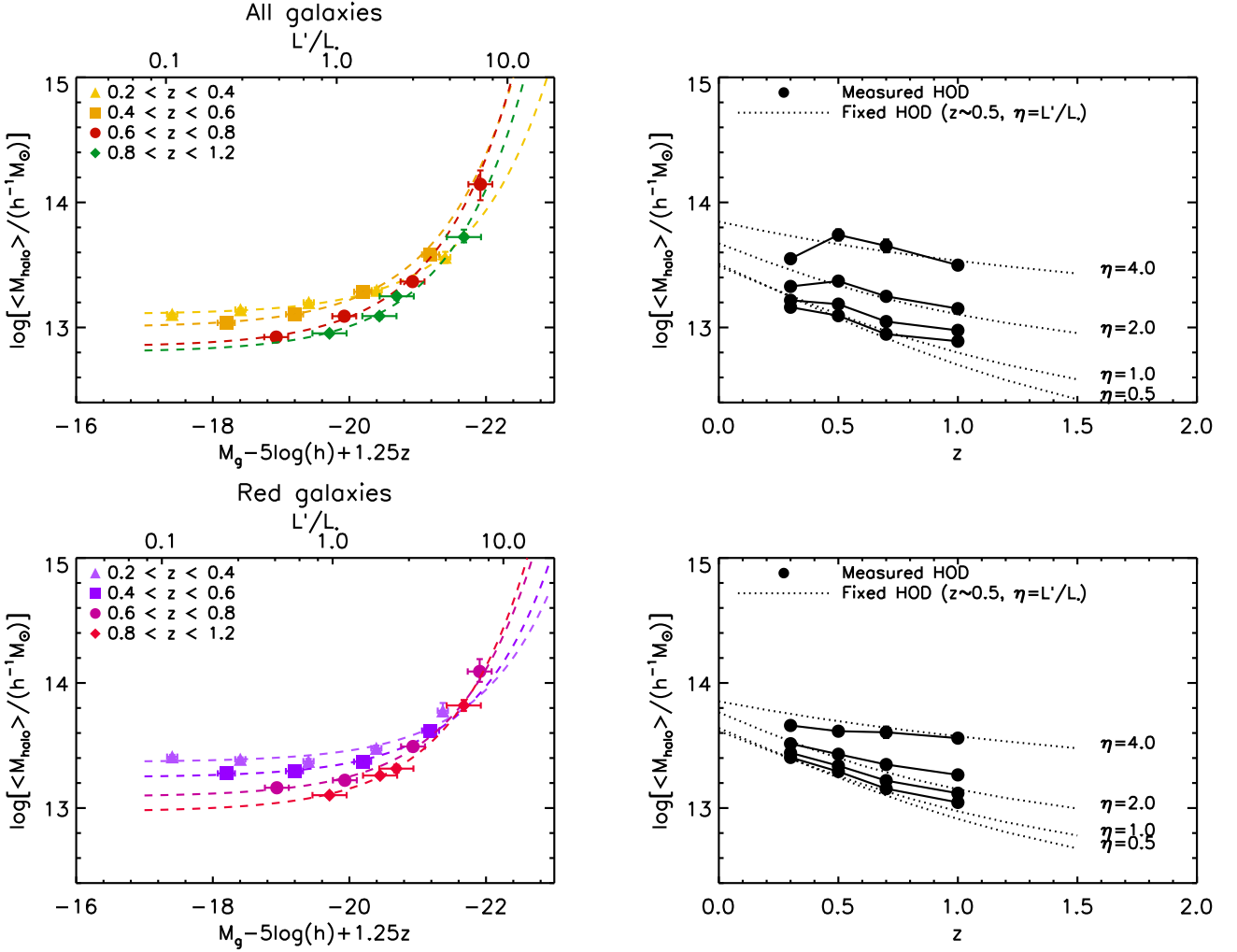


Fig. 19. Mean halo mass as function of luminosity and redshift. Left panels: mean halo mass for full and red samples (top and bottom panels) as function of corrected luminosity threshold L' . The dashed line represents Eq. 30. Right panels: computed mean halo mass for several luminosity threshold samples L'_* as function of redshift. Error bars were derived from the parametric form shown on the left (dashed line), whereas the dotted lines show the mean halo mass evolution computed from our model, assuming a redshift-independent HOD parameter set.

Using 30-band photometric data from the COSMOS survey, we derived an empirical relation between stellar mass, luminosity and redshift and used this to convert our luminosity-selected samples to stellar-mass limited samples. All of our conclusions (following below) are independent of this correction.

These are our principal results:

1. For a given luminosity threshold, galaxies with redder rest-frame colours are more clustered than bluer ones. Clustering strength increases with increasing luminosity, reflecting that bright galaxies reside in more strongly clustered massive haloes.
2. We consider the redshift and luminosity evolution of halo parameters M_1 , representing the characteristic halo mass required to host at least one satellite galaxy, and M_{\min} , representing the halo mass where on average 50% of haloes contain one galaxy. For our full sample, M_1 is closely approximated by $\sim 17 \times M_{\min}$. This ratio becomes smaller at higher redshifts for lower-mass haloes. For red galaxies, M_1/M_{\min} is ~ 12 at intermediate mass scale, and remains constant for all halo masses over $0.2 < z < 0.8$. This lower ratio for

redder galaxies reflects the higher abundance of satellites in these haloes; in general, redder populations reside in more massive haloes.

3. By fitting a simple analytic relation between central galaxy luminosity and halo mass to our observations, we find a maximum in the stellar-to-halo mass ratio. In the lowest redshift bin $z \sim 0.3$, this peak mass is $M_h^{\text{peak}} = 4.5 \times 10^{11} h^{-1} M_\odot$ for the full samples, and $M_h^{\text{peak}} = 21 \times 10^{11} h^{-1} M_\odot$ for the red samples, respectively. This transition represents the halo masses where baryons were most efficiently converted into stars, and is in good agreement with measurements from other studies.
4. For the full sample, M_h^{peak} shifts to higher halo masses at higher redshifts. For the red galaxy sample, the peak position evolves less rapidly with redshift. These results can be understood qualitatively from the lack of on-going star-formation in the red galaxy population which means that the stellar mass content in these massive haloes changes very slowly. For the full galaxy sample, which is expected to contain galaxies still undergoing active star-formation, the shift

of the transition mass to progressively more massive haloes at higher redshifts is a manifestation of “anti-hierarchical” galaxy formation. These results also indicate that the massive, passive galaxies in our survey are already fully formed by $z \sim 1.2$.

5. At increasing luminosities, the fraction of satellite galaxies rapidly drops to zero. For less luminous galaxies, the satellite fraction is higher in our red sample than in our full sample, reflecting the high number of faint red satellites, consistent with observations in the local Universe (Mandelbaum et al. 2006; Zehavi et al. 2010). For our full sample, the number of satellites increases by a factor of two from $z \sim 1$ to $z \sim 0$, consistent with a combined study of galaxies in DEEP2 and SDSS (Zheng et al. 2007). This result suggests that the occupation function for satellite galaxies inside intermediate-mass haloes ($\sim 10^{12} h^{-1} M_{\odot}$) remains constant with cosmic time, and implies that the galaxy merging rate does not change since $z = 1$.
6. Above the characteristic sample luminosity, the mean galaxy bias b_g increases rapidly. Faint red samples have $b_g \sim 1.5$, compared to $b_g \sim 1$ for the full sample. Redder samples also have higher average halo masses, which decrease towards higher redshifts.
7. We compare the measured evolution of our mean halo masses, biases and satellite fractions with a model assuming constant HOD parameters over our redshift range. This model provides a remarkably good fit to our measurements for massive haloes. We note that lower mean halo masses (particularly in the full sample) show a slower decrease compared to a redshift-independent HOD model.

Systematic photometric redshift errors have little impact on our faint luminosity-threshold samples, for which we find no evidence for incompleteness larger than the field-to-field variance estimates. Our very brightest samples however may be affected by incompleteness or contamination from fainter objects. We have shown that these errors could reduce our measured clustering amplitudes and consequently could lead to an underestimation of halo masses. The effect will be more important in contaminated samples, where the higher galaxy number density will lead to lower halo masses. In the worst case, $\log M_{\min}$ might be underestimated by ~ 0.5 .

Because of the lack of deep near-infrared data in the CFHTLS, we cannot calculate reliable stellar masses and cleanly separate the active and passive populations in mass-selected samples. Such a data set, perhaps combined with approximate local density estimators calibrated using spectroscopic redshifts, and a refined halo model would allow us to understand in greater detail the physical origin of the shift of the transition masses to higher halo masses observed here. Furthermore, given the fact that the peak of the star-formation and mass assembly takes place in the redshift range $1 < z < 2$, it is important to push these studies to higher redshifts by constructing larger, wide-area surveys with deep near-infrared data.

In our model, we have assumed a halo mass function, halo density profile, and a cosmological model, although it is well known that the evolution of galaxy clustering depends on these parameters. Combining galaxy-galaxy lensing, galaxy clustering and mass-function measurements from an expanded CFHTLS including near-infrared data should provide new insights on both cosmology and galaxy evolution.

Acknowledgements

We acknowledge CFHT, TERAPIX, CADM and the CFHTLS Steering Group for their assistance in planning, executing and reducing the CFHTLS survey. We also acknowledge the COSMOS, VVDS and DEEP2 collaborations for making their data publicly available. We thank T. Hamana, S. Colombi, M. Brown, M. White, A. Ross, A. Leauthaud and P. Behroozi for useful comments. We thank the referee for his careful and detailed report. HJMCC acknowledges support from ANR grant “ANR-07-BLAN-0228”. JC is supported by the Japanese Society for the Promotion of Science.

References

- Abbas, U., de la Torre, S., Le Fèvre, O., et al. 2010, MNRAS, 406, 1306
 Arnouts, S., Moscardini, L., Vanzella, E., et al. 2002, MNRAS, 329, 355
 Auger, M. W., Treu, T., Bolton, A. S., et al. 2010, ApJ, 724, 511
 Behroozi, P. S., Conroy, C., & Wechsler, R. H. 2010, ApJ, 717, 379
 Benítez, N. 2000, ApJ, 536, 571
 Benjamin, J., van Waerbeke, L., Ménard, B., & Kilbinger, M. 2010, MNRAS, 408, 1168
 Benson, A. J., Bower, R. G., Frenk, C. S., et al. 2003, ApJ, 599, 38
 Berlind, A. A., Blanton, M. R., Hogg, D. W., et al. 2005, ApJ, 629, 625
 Berlind, A. A. & Weinberg, D. H. 2002, ApJ, 575, 587
 Berlind, A. A., Weinberg, D. H., Benson, A. J., et al. 2003, ApJ, 593, 1
 Bertin, E. & Arnouts, S. 1996, A&AS, 117, 393
 Blake, C., Collister, A., & Lahav, O. 2008, MNRAS, 385, 1257
 Bower, R. G., Benson, A. J., Malbon, R., et al. 2006, MNRAS, 370, 645
 Brown, M. J. I., Zheng, Z., White, M., et al. 2008, ApJ, 682, 937
 Bundy, K., Fukugita, M., Ellis, R. S., et al. 2009, ApJ, 697, 1369
 Calzetti, D., Armus, L., Bohlin, R. C., et al. 2000, ApJ, 533, 682
 Cappé, O., Douc, R., Guillin, A., Marin, J.-M., & Robert, C. 2008, Statist. Comput., 18(4), 447
 Cappé, O., Guillin, A., Marin, J.-M., & Robert, C. 2004, J. Comput. Graph. Statist., 13, 907
 Cattaneo, A., Faber, S. M., Binney, J., et al. 2009, Nature, 460, 213
 Coleman, G. D., Wu, C.-C., & Weedman, D. W. 1980, ApJS, 43, 393
 Conroy, C. & Wechsler, R. H. 2009, ApJ, 696, 620
 Cooray, A. & Sheth, R. 2002, Phys. Rep., 372, 1
 Coupon, J., Ilbert, O., Kilbinger, M., et al. 2009, A&A, 500, 981
 Cowie, L. L., Songaila, A., Hu, E. M., & Cohen, J. G. 1996, AJ, 112, 839
 Croton, D. J., Gao, L., & White, S. D. M. 2007, MNRAS, 374, 1303
 Croton, D. J., Springel, V., White, S. D. M., et al. 2006, MNRAS, 365, 11
 Davis, M., Faber, S. M., Newman, J., et al. 2003, in Presented at the Society of Photo-Optical Instrumentation Engineers (SPIE) Conference, Vol. 4834, Discoveries and Research Prospects from 6- to 10-Meter-Class Telescopes II. Edited by Guhathakurta, Puragra. Proceedings of the SPIE, Volume 4834, pp. 161-172 (2003), ed. P. Guhathakurta, 161–172
 de la Torre, S., Guzzo, L., Kovač, K., et al. 2010, MNRAS, 409, 867
 Faber, S. M., Willmer, C. N. A., Wolf, C., et al. 2007, ApJ, 665, 265
 Fall, S. M. & Efstathiou, G. 1980, MNRAS, 193, 189
 Foucaud, S., Conselice, C. J., Hartley, W. G., et al. 2010, MNRAS, 406, 147
 Garilli, B., Le Fèvre, O., Guzzo, L., et al. 2008, A&A, 486, 683
 Goranova, Y., Hudelot, P., Magnard, F., et al. 2009, The CFHTLS T0006 Release
 Groth, E. J. & Peebles, P. J. E. 1977, ApJ, 217, 385
 Gunn, J. E. & Gott, III, J. R. 1972, ApJ, 176, 1
 Guo, Q., White, S., Li, C., & Boylan-Kolchin, M. 2010, MNRAS, 404, 1111
 Hamilton, A. J. S. 2000, MNRAS, 312, 257
 Hartlap, J., Simon, P., & Schneider, P. 2007, A&A, 464, 399
 Henry, J. P. 2000, ApJ, 534, 565
 Heymans, C., Bell, E. F., Rix, H.-W., et al. 2006, MNRAS, 371, L60
 High, F. W., Stubbs, C. W., Rest, A., Stalder, B., & Challis, P. 2009, AJ, 138, 110
 Hoaglin, D. C., Mosteller, F., & Tukey, J. W. 1983, Understanding robust and exploratory data analysis, ed. Hoaglin, D. C., Mosteller, F., & Tukey, J. W.
 Hopkins, P. F., Somerville, R. S., Hernquist, L., et al. 2006, ApJ, 652, 864
 Hu, W. & Kravtsov, A. V. 2003, ApJ, 584, 702
 Ilbert, O., Arnouts, S., McCracken, H. J., et al. 2006, A&A, 457, 841
 Ilbert, O., Capak, P., Salvato, M., et al. 2009, ApJ, 690, 1236
 Ilbert, O., Salvato, M., Le Flocc’h, E., et al. 2010, ApJ, 709, 644
 Ilbert, O., Tresse, L., Zucca, E., et al. 2005, A&A, 439, 863
 Kilbinger, M., Benabed, K., Cappe, O., et al. 2011, ArXiv e-prints
 Kilbinger, M., Wraith, D., Robert, C. P., et al. 2010, MNRAS, 405, 2381
 Kinney, A. L., Calzetti, D., Bohlin, R. C., et al. 1996, ApJ, 467, 38
 Kitayama, T. & Suto, Y. 1996, ApJ, 469, 480

Kravtsov, A. V., Berlind, A. A., Wechsler, R. H., et al. 2004, *ApJ*, 609, 35
 Landy, S. D. & Szalay, A. S. 1993, *ApJ*, 412, 64
 Larson, R. B., Tinsley, B. M., & Caldwell, C. N. 1980, *ApJ*, 237, 692
 Le Fèvre, O., Vettolani, G., Garilli, B., et al. 2005, *A&A*, 439, 845
 Leauthaud, A., Tinker, J., Behroozi, P. S., Busha, M. T., & Wechsler, R. 2011a, *ArXiv e-prints*
 Leauthaud, A., Tinker, J., Bundy, K., et al. 2011b, *ArXiv e-prints*
 Limber, D. N. 1954, *ApJ*, 119, 655
 Mandelbaum, R., Seljak, U., Kauffmann, G., Hirata, C. M., & Brinkmann, J. 2006, *MNRAS*, 368, 715
 McCracken, H. J., Peacock, J. A., Guzzo, L., et al. 2007, *ApJS*, 172, 314
 Meneux, B., Guzzo, L., de la Torre, S., et al. 2009, *A&A*, 505, 463
 More, S., van den Bosch, F. C., Cacciato, M., et al. 2011, *MNRAS*, 410, 210
 Moster, B. P., Somerville, R. S., Maubetsch, C., et al. 2010, *ApJ*, 710, 903
 Nakamura, T. T. & Suto, Y. 1997, *Progress of Theoretical Physics*, 97, 49
 Navarro, J. F., Frenk, C. S., & White, S. D. M. 1997, *ApJ*, 490, 493
 Norberg, P., Baugh, C. M., Hawkins, E., et al. 2001, *MNRAS*, 328, 64
 Peng, Y., Lilly, S. J., Renzini, A., & Carollo, M. 2011, *ArXiv e-prints*
 Peng, Y.-j., Lilly, S. J., Kovač, K., et al. 2010, *ApJ*, 721, 193
 Peterson, J. R. & Fabian, A. C. 2006, *Phys. Rep.*, 427, 1
 Phleps, S., Peacock, J. A., Meisenheimer, K., & Wolf, C. 2006, *A&A*, 457, 145
 Press, W. H. & Schechter, P. 1974, *ApJ*, 187, 425
 Robaina, A. R., Bell, E. F., van der Wel, A., et al. 2010, *ApJ*, 719, 844
 Sheth, R. K., Mo, H. J., & Tormen, G. 2001, *MNRAS*, 323, 1
 Sheth, R. K. & Tormen, G. 1999, *MNRAS*, 308, 119
 Simon, P., Hettterscheidt, M., Wolf, C., et al. 2009, *MNRAS*, 398, 807
 Skibba, R. A. & Sheth, R. K. 2009, *MNRAS*, 392, 1080
 Somerville, R. S., Hopkins, P. F., Cox, T. J., Robertson, B. E., & Hernquist, L. 2008, *MNRAS*, 391, 481
 Springel, V., Frenk, C. S., & White, S. D. M. 2006, *Nature*, 440, 1137
 Szalay, A. S., Connolly, A. J., & Szokoly, G. P. 1999, *AJ*, 117, 68
 Takada, M. & Jain, B. 2003, *MNRAS*, 344, 857
 Tinker, J. L., Weinberg, D. H., Zheng, Z., & Zehavi, I. 2005, *ApJ*, 631, 41
 van Dokkum, P. G., Whitaker, K. E., Brammer, G., et al. 2010, *ApJ*, 709, 1018
 Wake, D. A., Whitaker, K. E., Labbé, I., et al. 2011, *ApJ*, 728, 46
 Wang, L. & Jing, Y. P. 2010, *MNRAS*, 402, 1796
 Weinberg, N. N. & Kamionkowski, M. 2003, *MNRAS*, 341, 251
 White, M., Zheng, Z., Brown, M. J. I., Dey, A., & Jannuzi, B. T. 2007, *ApJ*, 655, L69
 White, S. D. M. & Rees, M. J. 1978, *MNRAS*, 183, 341
 Willmer, C. N. A., Faber, S. M., Koo, D. C., et al. 2006, *ApJ*, 647, 853
 Wraith, D., Kilbinger, M., Benabed, K., et al. 2009, *Phys. Rev. D*, 80, 023507
 Zehavi, I., Patiri, S., & Zheng, Z. 2011, *ArXiv e-prints*
 Zehavi, I., Zheng, Z., Weinberg, D. H., et al. 2010, *ArXiv e-prints*
 Zehavi, I., Zheng, Z., Weinberg, D. H., et al. 2005, *ApJ*, 630, 1
 Zheng, Z. 2004, *ApJ*, 610, 61
 Zheng, Z., Berlind, A. A., Weinberg, D. H., et al. 2005, *ApJ*, 633, 791
 Zheng, Z., Coil, A. L., & Zehavi, I. 2007, *ApJ*, 667, 760
 Zheng, Z., Zehavi, I., Eisenstein, D. J., Weinberg, D. H., & Jing, Y. P. 2009, *ApJ*, 707, 554
 Zucca, E., Ilbert, O., Bardelli, S., et al. 2006, *A&A*, 455, 879

Appendix A: The halo model

The halo occupation distribution (HOD) model (Berlind & Weinberg 2002; Kravtsov et al. 2004; Zheng et al. 2005) allows one to derive physical information about galaxy populations and the dark matter haloes which host them. The HOD prescription is based on the halo model, which describes how dark matter is distributed in space. In this framework, all of the matter is assumed to reside in virialised haloes. The HOD parametrisation specifies how many galaxies populate haloes, on average, as function of halo mass. Accordingly, the number of galaxies per halo N only depends on the mass M of the halo.

A.1. Dark-matter halo model

The three ingredients to the halo model of dark matter are the halo mass function, the halo profile and the halo bias. The dark matter halo abundance can be inferred using the Press & Schechter (1974) approach where dark matter collapses into overdense regions above the critical density δ_c , linearly

evolved to $z = 0$. The mass function, which is the halo number density per unit mass, can be parametrized as

$$n(M, z) dM = \frac{\bar{\rho}_0}{M} f(\nu) d\nu, \quad (\text{A.1})$$

where $\bar{\rho}_0$ is the mean density of matter at the present day. The new mass variable ν writes

$$\nu = \frac{\delta_c(z)}{D(z)\sigma(M)}, \quad (\text{A.2})$$

and characterizes the peak heights of the density field as function of mass and redshift. The linear critical density δ_c depends on the adopted cosmology and redshift; we use the fitting formula from Weinberg & Kamionkowski (2003); see also Kitayama & Suto (1996),

$$\delta_c(z) = \frac{3}{20}(12\pi)^{2/3} [1 + 0.013 \log_{10} \Omega_m(z)]; \quad (\text{A.3})$$

$$\Omega_m(z) = \Omega_m(1+z)^3 \left[\frac{H_0}{H(z)} \right]^2. \quad (\text{A.4})$$

$D(z)$ is the linear growth factor at redshift z , and $\sigma(M)$ is the rms of density fluctuations in a top-hat filter of width $R = (3M/4\pi\bar{\rho}_0)^{1/3}$, computed from linear theory,

$$\sigma^2(M) = \int_0^\infty \frac{dk}{k} \frac{k^3 P_{\text{lin}}(k)}{2\pi^2} W^2(kR), \quad (\text{A.5})$$

where $W(x) = (3/x^3)[\sin x - x \cos x]$. For the mass function $f(\nu)$, we choose the parameterisation by Sheth & Tormen (1999), calibrated on simulations:

$$\nu f(\nu) = A \sqrt{\frac{2a\nu^2}{\pi}} \left[1 + (a\nu^2)^{-p} \right] \exp\left(-\frac{a\nu^2}{2}\right), \quad (\text{A.6})$$

where the normalisation A is fixed by imposing:

$$\int n(M, z) \frac{M}{\rho_0} dM = \int f(\nu) d\nu = 1, \quad (\text{A.7})$$

We adopt the values $p = 0.3$ and $a = 1/\sqrt{2}$. If not indicated otherwise, all integrals over the mass function are performed between $M_{\text{low}} = 10^3 h^{-1} M_\odot$ and $M_{\text{high}} = 10^{16} h^{-1} M_\odot$.

We describe the halo density profile by the following form Navarro et al. (1997),

$$\rho_h(r|M) = \frac{\rho_s}{(r/r_s)(1+r/r_s)^2}. \quad (\text{A.8})$$

The total halo mass is then written as (see Takada & Jain 2003):

$$M = \int_0^{r_{\text{vir}}} 4\pi r^2 dr \rho_h(r|M) = \frac{4\pi\rho_s r_{\text{vir}}^3}{c^3} \left[\ln(1+c) - \frac{c}{1+c} \right], \quad (\text{A.9})$$

where $c = r_{\text{vir}}/r_s$ is the ‘‘concentration parameter’’, for which we assume the following expression,

$$c(M, z) = \frac{c_0}{1+z} \left[\frac{M}{M_\star} \right]^{-\beta}. \quad (\text{A.10})$$

We take $c_0 = 11$ and $\beta = 0.13$, and M_\star is defined such that $\nu(z=0) = 1$, i.e. $\delta_c(0) = \sigma(M_\star)$. The virial radius r_{vir} is given by the following relation

$$M = \frac{4\pi r_{\text{vir}}^3}{3} \bar{\rho}_0 \Delta_{\text{vir}}(z), \quad (\text{A.11})$$

with $\Delta_{\text{vir}}(z)$ being the critical overdensity for virialisation at redshift z (Kitayama & Suto 1996; Nakamura & Suto 1997; Henry 2000). We take the fitting formula from Weinberg & Kamionkowski (2003)

$$\Delta_{\text{vir}}(z) = 18\pi^2 \left[1 + 0.399 \left(\Omega_{\text{m}}^{-1}(z) - 1 \right)^{0.941} \right]. \quad (\text{A.12})$$

Following Tinker et al. (2005), we use the scale-dependent halo bias

$$b_{\text{h}}^2(M, z, r) = b_{\text{h}}^2(M, z) \frac{[1 + 1.17\xi_{\text{m}}(r, z)]^{1.49}}{[1 + 0.69\xi_{\text{m}}(r, z)]^{2.09}}, \quad (\text{A.13})$$

where ξ_{m} is the matter correlation function. The large-scale halo bias $b_{\text{h}}(M, z)$ is given by Sheth et al. (2001) as

$$b_{\text{h}}(M, z) = b_{\text{h}}(v) = 1 + \frac{1}{\sqrt{a}\delta_{\text{c}}} \left[\sqrt{a}(av^2) + \sqrt{ab}(av^2)^{1-c} - \frac{(av^2)^c}{(av^2)^c + b(1-c)(1-c/2)} \right]. \quad (\text{A.14})$$

As in Tinker et al. (2005), we adopt the revised parameters $a = 1/\sqrt{2}$, $b = 0.35$ and $c = 0.8$.

A.2. The galaxy correlation function

We write the correlation function as a sum of two components: The one-halo term, to express the galaxy correlation inside a halo, and the two-halo term, to account for halo-to-halo correlation,

$$\xi(r) = 1 + \xi_1(r) + \xi_2(r), \quad (\text{A.15})$$

The one-halo term depends on the number of galaxy pairs $\langle N(N-1) \rangle$ per halo. This is comprised of the central-satellite contribution $\langle N_{\text{c}}N_{\text{s}} \rangle$ and the satellite-satellite term $\langle N_{\text{s}}(N_{\text{s}}-1) \rangle$. Assuming a Poisson distribution, we write

$$\begin{aligned} \langle N_{\text{s}}(N_{\text{s}}-1) \rangle(M) &= N_{\text{s}}^2(M); \\ \langle N_{\text{c}}N_{\text{s}} \rangle(M) &= N_{\text{c}}(M)N_{\text{s}}(M). \end{aligned} \quad (\text{A.16})$$

The one-halo term correlation function for central-satellite pairs is then

$$1 + \xi_{\text{cs}}(r, z) = \int_{M_{\text{vir}}(r)}^{M_{\text{high}}} dM n(M, z) \frac{N_{\text{c}}(M)N_{\text{s}}(M)}{n_{\text{gal}}^2/2} \rho_{\text{h}}(r|M). \quad (\text{A.17})$$

The lower integration limit $M_{\text{vir}}(r)$ is the virial mass contained in a halo of radius r , computed with Eq. A.11. This accounts for the fact that less-massive haloes are too small to contribute to the correlation at separation r .

The one-halo satellite-satellite contribution ξ_{ss} involves the halo profile auto-convolution and is therefore easier to compute in Fourier space. The corresponding power spectrum is written as

$$P_{\text{ss}}(k) = \int_{M_{\text{low}}}^{M_{\text{high}}} dM n(M) \frac{N_{\text{s}}^2(M)}{n_{\text{gal}}^2} |u_{\text{h}}(k|M)|^2, \quad (\text{A.18})$$

where $u_{\text{h}}(k|M)$ is the Fourier transform of the dark-matter halo profile $\rho_{\text{h}}(r|M)$. The correlation function ξ_{ss} is then obtained via a Fourier transform. The one-halo correlation function is the sum of the two contributions,

$$\xi_1(r) = \xi_{\text{cs}}(r) + \xi_{\text{ss}}(r). \quad (\text{A.19})$$

The two-halo term is derived from the dark-matter power spectrum and the halo two-point correlation function:

$$P_2(k, r) = P_{\text{m}}(k) \times \left[\int_{M_{\text{low}}}^{M_{\text{lim}}(r)} dM n(M) \frac{N(M)}{n'_{\text{gal}}(r)} b_{\text{h}}(M, r) |u_{\text{h}}(k|M)| \right]^2 \quad (\text{A.20})$$

where

$$n'_{\text{gal}}(r) = \int_{M_{\text{low}}}^{M_{\text{lim}}(r)} n(M)N(M, z) dM. \quad (\text{A.21})$$

The upper integration limit $M_{\text{lim}}(r)$ takes into account the halo exclusion (Zheng 2004), i.e. the fact that haloes are non-overlapping. We follow Tinker et al. (2005) to compute $M_{\text{lim}}(r)$ by matching $n'_{\text{gal}}(r)$ with the following expression,

$$n'_{\text{gal}}(r) = \int dM_1 n(M_1)N(M_1) \times \int dM_2 n(M_2)N(M_2)P(r, M_1, M_2), \quad (\text{A.22})$$

where $P(r, M_1, M_2)$ is the probability that two ellipsoidal haloes of mass M_1 and M_2 , respectively, do not overlap. Defining $x = r/[r_{\text{vir}}(M_1) + r_{\text{vir}}(M_2)]$ as the ratio of the halo separation and the sum of the virial radii, and $y = (x-0.8)/0.29$, Tinker et al. (2005) found the probability of non-overlapping haloes to be

$$P(r, M_1, M_2) = P(y) = \begin{cases} 0 & \text{if } y < 0 \\ (3y^2 - 2y^3) & \text{if } 0 \leq y \leq 1 \\ 1 & \text{if } y > 1 \end{cases}. \quad (\text{A.23})$$

We Fourier-transform Eq. A.20 for a range of tabulated values of r , to compute the two-halo term ξ_2 of the galaxy autocorrelation function. Finally, we renormalise it to the total number of galaxy pairs:

$$1 + \xi_2(r) = \left[\frac{n'_{\text{gal}}(r)}{n_{\text{gal}}} \right] [1 + \xi_2(r)]. \quad (\text{A.24})$$

The angular two-point correlation function $w(\theta)$ is computed from the observed photometric redshift distribution and $\xi(r)$ using Limber's equation (Limber 1954):

$$w(\theta) = 2 \int_0^{\infty} dx f(x)^2 \int_0^{\infty} du \xi(r = \sqrt{u^2 + x^2\theta^2}), \quad (\text{A.25})$$

with

$$f(x) = \frac{n(z)}{dx(z)/dz}, \quad (\text{A.26})$$

and $x(z)$, the radial comoving coordinate.

Appendix B: Best-fitting HOD parameters and deduced quantities

Table B.1. Description of all galaxy samples and best-fitting HOD parameters. Halo masses are given in $h^{-1}M_{\odot}$ and galaxy number densities in $h^{-3} \text{Mpc}^3$.

Redshift	$M_g - 5 \log h$	N	$\log n_{\text{gal,obs}}$	$\log M_{\text{min}}$	$\log M_1$	$\log M_0$	$\sigma_{\log M}$	α	$\log n_{\text{gal,mod}}$	b_g	$\log M_{\text{halo}}$	f_s	χ^2/dof
$0.2 < z < 0.4$	< -17.8	451 203	$-1.53^{+0.02}_{-0.02}$	$11.18^{+0.06}_{-0.05}$	$12.53^{+0.03}_{-0.03}$	$7.54^{+1.72}_{-1.71}$	$0.40^{+0.12}_{-0.13}$	$1.10^{+0.01}_{-0.01}$	$-1.53^{+0.02}_{-0.02}$	$1.08^{+0.01}_{-0.01}$	$13.11^{+0.01}_{-0.01}$	$0.23^{+0.01}_{-0.01}$	3.58
$0.2 < z < 0.4$	< -18.8	243 833	$-1.80^{+0.02}_{-0.02}$	$11.47^{+0.06}_{-0.06}$	$12.76^{+0.03}_{-0.03}$	$7.57^{+1.86}_{-1.78}$	$0.42^{+0.12}_{-0.15}$	$1.12^{+0.01}_{-0.01}$	$-1.79^{+0.02}_{-0.02}$	$1.14^{+0.01}_{-0.01}$	$13.14^{+0.01}_{-0.01}$	$0.22^{+0.01}_{-0.01}$	4.93
$0.2 < z < 0.4$	< -19.8	104 889	$-2.17^{+0.03}_{-0.03}$	$11.85^{+0.05}_{-0.06}$	$13.11^{+0.04}_{-0.04}$	$8.18^{+2.03}_{-2.15}$	$0.45^{+0.10}_{-0.16}$	$1.16^{+0.02}_{-0.02}$	$-2.16^{+0.03}_{-0.03}$	$1.23^{+0.01}_{-0.01}$	$13.20^{+0.01}_{-0.02}$	$0.18^{+0.01}_{-0.01}$	3.33
$0.2 < z < 0.4$	< -20.8	28 081	$-2.74^{+0.04}_{-0.04}$	$12.36^{+0.09}_{-0.05}$	$13.69^{+0.05}_{-0.05}$	$8.35^{+2.22}_{-2.32}$	$0.32^{+0.17}_{-0.13}$	$1.28^{+0.05}_{-0.05}$	$-2.74^{+0.04}_{-0.05}$	$1.43^{+0.02}_{-0.03}$	$13.30^{+0.02}_{-0.02}$	$0.12^{+0.01}_{-0.01}$	4.87
$0.2 < z < 0.4$	< -21.8	3 679	$-3.62^{+0.05}_{-0.05}$	$13.17^{+0.09}_{-0.08}$	$14.53^{+0.36}_{-0.14}$	$11.09^{+2.32}_{-3.28}$	$0.39^{+0.15}_{-0.18}$	$1.27^{+0.33}_{-0.47}$	$-3.64^{+0.05}_{-0.06}$	$1.91^{+0.07}_{-0.06}$	$13.56^{+0.04}_{-0.05}$	$0.04^{+0.01}_{-0.01}$	3.21
$0.4 < z < 0.6$	< -18.8	551 547	$-1.80^{+0.01}_{-0.01}$	$11.48^{+0.06}_{-0.06}$	$12.66^{+0.03}_{-0.03}$	$10.96^{+0.26}_{-0.72}$	$0.43^{+0.11}_{-0.15}$	$1.09^{+0.02}_{-0.02}$	$-1.80^{+0.01}_{-0.02}$	$1.23^{+0.01}_{-0.01}$	$13.04^{+0.01}_{-0.01}$	$0.23^{+0.01}_{-0.00}$	3.71
$0.4 < z < 0.6$	< -19.8	244 854	$-2.15^{+0.02}_{-0.02}$	$11.82^{+0.06}_{-0.06}$	$13.01^{+0.04}_{-0.04}$	$11.02^{+0.38}_{-0.63}$	$0.43^{+0.11}_{-0.13}$	$1.15^{+0.03}_{-0.03}$	$-2.14^{+0.02}_{-0.03}$	$1.33^{+0.01}_{-0.01}$	$13.11^{+0.01}_{-0.01}$	$0.20^{+0.01}_{-0.01}$	3.62
$0.4 < z < 0.6$	< -20.8	65 557	$-2.73^{+0.04}_{-0.04}$	$12.33^{+0.06}_{-0.03}$	$13.58^{+0.04}_{-0.04}$	$8.49^{+2.40}_{-2.26}$	$0.30^{+0.11}_{-0.09}$	$1.37^{+0.03}_{-0.03}$	$-2.74^{+0.04}_{-0.03}$	$1.58^{+0.02}_{-0.02}$	$13.29^{+0.01}_{-0.01}$	$0.14^{+0.01}_{-0.01}$	3.86
$0.4 < z < 0.6$	< -21.8	6 724	$-3.71^{+0.06}_{-0.06}$	$13.18^{+0.09}_{-0.07}$	$14.47^{+0.48}_{-0.11}$	$10.93^{+1.69}_{-1.86}$	$0.30^{+0.16}_{-0.12}$	$1.36^{+0.24}_{-0.44}$	$-3.74^{+0.05}_{-0.07}$	$2.16^{+0.06}_{-0.07}$	$13.58^{+0.03}_{-0.04}$	$0.06^{+0.01}_{-0.01}$	1.93
$0.6 < z < 0.8$	< -19.8	458 863	$-2.08^{+0.03}_{-0.03}$	$11.77^{+0.05}_{-0.05}$	$12.83^{+0.04}_{-0.04}$	$11.54^{+0.15}_{-0.18}$	$0.50^{+0.07}_{-0.10}$	$1.07^{+0.03}_{-0.03}$	$-2.07^{+0.03}_{-0.03}$	$1.40^{+0.01}_{-0.01}$	$12.92^{+0.01}_{-0.01}$	$0.19^{+0.01}_{-0.01}$	1.85
$0.6 < z < 0.8$	< -20.8	141 129	$-2.59^{+0.04}_{-0.04}$	$12.24^{+0.04}_{-0.07}$	$13.34^{+0.05}_{-0.04}$	$10.50^{+0.84}_{-0.84}$	$0.50^{+0.06}_{-0.36}$	$1.28^{+0.03}_{-0.03}$	$-2.57^{+0.04}_{-0.05}$	$1.60^{+0.03}_{-0.02}$	$13.09^{+0.01}_{-0.01}$	$0.15^{+0.01}_{-0.01}$	2.92
$0.6 < z < 0.8$	< -21.8	17 683	$-3.50^{+0.06}_{-0.06}$	$12.96^{+0.10}_{-0.09}$	$14.10^{+0.07}_{-0.09}$	$12.47^{+0.62}_{-0.93}$	$0.38^{+0.14}_{-0.21}$	$1.28^{+0.23}_{-0.51}$	$-3.49^{+0.05}_{-0.06}$	$2.13^{+0.08}_{-0.07}$	$13.37^{+0.03}_{-0.03}$	$0.06^{+0.01}_{-0.01}$	4.76
$0.6 < z < 0.8$	< -22.8	656	$-4.93^{+0.18}_{-0.18}$	$14.12^{+0.32}_{-0.16}$	$16.09^{+0.58}_{-0.57}$	$9.72^{+3.15}_{-3.11}$	$0.31^{+0.18}_{-0.12}$	$1.31^{+0.44}_{-0.36}$	$-5.37^{+0.29}_{-0.43}$	$4.12^{+0.44}_{-0.42}$	$14.14^{+0.11}_{-0.13}$	$0.01^{+0.01}_{-0.00}$	10.17
$0.8 < z < 1.0$	< -20.8	200 516	$-2.57^{+0.04}_{-0.04}$	$12.14^{+0.09}_{-0.06}$	$13.21^{+0.08}_{-0.09}$	$12.23^{+0.18}_{-0.27}$	$0.35^{+0.14}_{-0.13}$	$1.12^{+0.09}_{-0.13}$	$-2.58^{+0.04}_{-0.05}$	$1.74^{+0.03}_{-0.03}$	$12.95^{+0.02}_{-0.02}$	$0.13^{+0.01}_{-0.01}$	4.85
$0.8 < z < 1.0$	< -21.8	31 001	$-3.38^{+0.05}_{-0.05}$	$12.80^{+0.10}_{-0.07}$	$13.94^{+0.06}_{-0.36}$	$12.15^{+0.91}_{-1.01}$	$0.33^{+0.14}_{-0.15}$	$1.52^{+0.20}_{-0.88}$	$-3.39^{+0.05}_{-0.06}$	$2.25^{+0.05}_{-0.06}$	$13.25^{+0.02}_{-0.03}$	$0.06^{+0.01}_{-0.01}$	8.69
$0.8 < z < 1.0$	< -22.8	1 411	$-4.72^{+0.15}_{-0.15}$	$13.76^{+0.10}_{-0.16}$	$15.13^{+0.47}_{-0.36}$	$9.11^{+2.48}_{-2.91}$	$0.48^{+0.08}_{-0.37}$	$0.94^{+0.60}_{-0.20}$	$-4.64^{+0.10}_{-0.14}$	$3.28^{+0.23}_{-0.12}$	$13.72^{+0.06}_{-0.04}$	$0.05^{+0.02}_{-0.02}$	7.35
$1.0 < z < 1.2$	< -21.8	52 310	$-3.24^{+0.04}_{-0.04}$	$12.62^{+0.08}_{-0.04}$	$13.79^{+0.05}_{-0.04}$	$8.67^{+2.54}_{-2.44}$	$0.30^{+0.14}_{-0.09}$	$1.50^{+0.09}_{-0.11}$	$-3.25^{+0.04}_{-0.04}$	$2.33^{+0.04}_{-0.06}$	$13.09^{+0.02}_{-0.02}$	$0.08^{+0.01}_{-0.01}$	3.24

Table B.2. Description of red galaxy samples and best-fitting HOD parameters. Halo masses are given in $h^{-1}M_{\odot}$ and galaxy number densities in $h^{-3} \text{Mpc}^3$.

Redshift	$M_g - 5 \log h$	N	$\log n_{\text{gal,obs}}$	$\log M_{\text{min}}$	$\log M_1$	$\log M_0$	$\sigma_{\log M}$	α	$\log n_{\text{gal,mod}}$	b_g	$\log M_{\text{halo}}$	f_s	χ^2/dof
$0.2 < z < 0.4$	< -17.8	153 729	$-2.00^{+0.04}_{-0.04}$	$11.77^{+0.06}_{-0.07}$	$12.70^{+0.05}_{-0.05}$	$9.69^{+1.65}_{-3.45}$	$0.41^{+0.12}_{-0.22}$	$1.13^{+0.02}_{-0.04}$	$-1.99^{+0.03}_{-0.04}$	$1.37^{+0.01}_{-0.01}$	$13.41^{+0.02}_{-0.02}$	$0.36^{+0.01}_{-0.01}$	4.77
$0.2 < z < 0.4$	< -18.8	100 829	$-2.19^{+0.04}_{-0.04}$	$11.90^{+0.08}_{-0.06}$	$12.94^{+0.06}_{-0.05}$	$8.04^{+2.09}_{-2.02}$	$0.37^{+0.14}_{-0.15}$	$1.17^{+0.02}_{-0.02}$	$-2.17^{+0.04}_{-0.05}$	$1.37^{+0.01}_{-0.02}$	$13.39^{+0.01}_{-0.02}$	$0.30^{+0.01}_{-0.02}$	5.64
$0.2 < z < 0.4$	< -19.8	54 393	$-2.45^{+0.04}_{-0.04}$	$12.15^{+0.08}_{-0.06}$	$13.25^{+0.07}_{-0.07}$	$10.58^{+1.28}_{-2.42}$	$0.36^{+0.15}_{-0.15}$	$1.19^{+0.04}_{-0.13}$	$-2.46^{+0.04}_{-0.05}$	$1.42^{+0.02}_{-0.02}$	$13.37^{+0.02}_{-0.02}$	$0.22^{+0.01}_{-0.01}$	3.63
$0.2 < z < 0.4$	< -20.8	17 200	$-2.95^{+0.05}_{-0.05}$	$12.60^{+0.07}_{-0.07}$	$13.82^{+0.09}_{-0.07}$	$8.56^{+2.46}_{-2.48}$	$0.31^{+0.15}_{-0.10}$	$1.42^{+0.06}_{-0.06}$	$-2.99^{+0.06}_{-0.08}$	$1.61^{+0.04}_{-0.03}$	$13.48^{+0.02}_{-0.02}$	$0.13^{+0.01}_{-0.01}$	3.00
$0.2 < z < 0.4$	< -21.8	1 545	$-3.85^{+0.08}_{-0.08}$	$13.40^{+0.16}_{-0.09}$	$14.51^{+0.26}_{-0.30}$	$13.47^{+0.43}_{-1.52}$	$0.30^{+0.18}_{-0.11}$	$1.24^{+0.51}_{-0.46}$	$-3.98^{+0.10}_{-0.17}$	$2.25^{+0.13}_{-0.10}$	$13.78^{+0.06}_{-0.05}$	$0.04^{+0.01}_{-0.01}$	2.92
$0.4 < z < 0.6$	< -18.8	209 469	$-2.22^{+0.03}_{-0.03}$	$11.94^{+0.07}_{-0.05}$	$12.90^{+0.04}_{-0.04}$	$10.04^{+1.29}_{-2.37}$	$0.40^{+0.13}_{-0.12}$	$1.15^{+0.02}_{-0.03}$	$-2.21^{+0.03}_{-0.03}$	$1.48^{+0.01}_{-0.01}$	$13.28^{+0.01}_{-0.01}$	$0.30^{+0.01}_{-0.01}$	4.96
$0.4 < z < 0.6$	< -19.8	122 073	$-2.46^{+0.03}_{-0.03}$	$12.10^{+0.04}_{-0.03}$	$13.19^{+0.04}_{-0.03}$	$8.37^{+1.99}_{-1.97}$	$0.26^{+0.12}_{-0.07}$	$1.22^{+0.02}_{-0.02}$	$-2.46^{+0.03}_{-0.03}$	$1.54^{+0.01}_{-0.01}$	$13.29^{+0.01}_{-0.01}$	$0.24^{+0.01}_{-0.01}$	3.07
$0.4 < z < 0.6$	< -20.8	42 303	$-2.92^{+0.03}_{-0.03}$	$12.52^{+0.05}_{-0.05}$	$13.61^{+0.05}_{-0.11}$	$11.79^{+0.65}_{-1.03}$	$0.29^{+0.12}_{-0.08}$	$1.26^{+0.07}_{-0.27}$	$-2.93^{+0.03}_{-0.04}$	$1.72^{+0.02}_{-0.02}$	$13.37^{+0.01}_{-0.02}$	$0.16^{+0.01}_{-0.01}$	3.88
$0.4 < z < 0.6$	< -21.8	5 210	$-3.82^{+0.05}_{-0.05}$	$13.27^{+0.08}_{-0.05}$	$14.70^{+0.42}_{-0.22}$	$9.48^{+2.65}_{-2.83}$	$0.32^{+0.14}_{-0.11}$	$1.03^{+0.28}_{-0.26}$	$-3.84^{+0.05}_{-0.05}$	$2.24^{+0.07}_{-0.07}$	$13.62^{+0.04}_{-0.04}$	$0.07^{+0.01}_{-0.01}$	1.14
$0.6 < z < 0.8$	< -19.8	216 675	$-2.41^{+0.05}_{-0.05}$	$12.14^{+0.07}_{-0.02}$	$13.21^{+0.04}_{-0.04}$	$11.65^{+0.19}_{-0.16}$	$0.25^{+0.11}_{-0.06}$	$1.22^{+0.02}_{-0.03}$	$-2.56^{+0.02}_{-0.03}$	$1.69^{+0.01}_{-0.01}$	$13.16^{+0.01}_{-0.01}$	$0.21^{+0.01}_{-0.01}$	4.35
$0.6 < z < 0.8$	< -20.8	83 687	$-2.82^{+0.05}_{-0.05}$	$12.40^{+0.09}_{-0.07}$	$13.46^{+0.05}_{-0.05}$	$8.25^{+2.20}_{-2.22}$	$0.36^{+0.14}_{-0.14}$	$1.31^{+0.03}_{-0.03}$	$-2.80^{+0.04}_{-0.05}$	$1.79^{+0.02}_{-0.03}$	$13.22^{+0.01}_{-0.01}$	$0.17^{+0.01}_{-0.01}$	2.76
$0.6 < z < 0.8$	< -21.8	11 982	$-3.67^{+0.07}_{-0.07}$	$13.06^{+0.11}_{-0.06}$	$14.19^{+0.07}_{-0.06}$	$9.43^{+2.38}_{-3.31}$	$0.28^{+0.16}_{-0.13}$	$1.54^{+0.12}_{-0.19}$	$-3.67^{+0.06}_{-0.07}$	$2.34^{+0.06}_{-0.08}$	$13.49^{+0.03}_{-0.03}$	$0.07^{+0.01}_{-0.01}$	2.93
$0.6 < z < 0.8$	< -22.8	385	$-5.16^{+0.16}_{-0.16}$	$14.08^{+0.21}_{-0.13}$	$16.27^{+0.48}_{-0.61}$	$9.87^{+3.43}_{-3.28}$	$0.34^{+0.17}_{-0.15}$	$1.35^{+0.44}_{-0.46}$	$-5.24^{+0.17}_{-0.35}$	$3.92^{+0.37}_{-0.30}$	$14.09^{+0.10}_{-0.08}$	$0.00^{+0.00}_{-0.00}$	6.24
$0.8 < z < 1.0$	< -20.8	111 158	$-2.83^{+0.06}_{-0.06}$	$12.37^{+0.07}_{-0.05}$	$13.48^{+0.07}_{-0.05}$	$11.76^{+0.37}_{-0.34}$	$0.26^{+0.11}_{-0.09}$	$1.31^{+0.05}_{-0.10}$	$-2.88^{+0.05}_{-0.07}$	$1.96^{+0.03}_{-0.03}$	$13.10^{+0.02}_{-0.02}$	$0.14^{+0.01}_{-0.01}$	4.65
$0.8 < z < 1.0$	< -21.8	21 494	$-3.54^{+0.06}_{-0.06}$	$12.93^{+0.11}_{-0.06}$	$14.07^{+0.07}_{-0.06}$	$10.86^{+1.57}_{-1.52}$	$0.34^{+0.14}_{-0.14}$	$1.61^{+0.14}_{-0.40}$	$-3.55^{+0.06}_{-0.06}$	$2.37^{+0.07}_{-0.07}$	$13.31^{+0.03}_{-0.03}$	$0.06^{+0.01}_{-0.01}$	4.65
$0.8 < z < 1.0$	< -22.8	955	$-4.89^{+0.12}_{-0.12}$	$13.74^{+0.05}_{-0.10}$	$15.62^{+0.43}_{-0.35}$	$9.27^{+1.95}_{-2.67}$	$0.34^{+0.07}_{-0.16}$	$0.82^{+0.78}_{-0.15}$	$-4.77^{+0.08}_{-0.10}$	$3.60^{+0.15}_{-0.15}$	$13.82^{+0.04}_{-0.04}$	$0.04^{+0.02}_{-0.02}$	5.21
$1.0 < z < 1.2$	< -21.8	30 637	$-3.47^{+0.04}_{-0.04}$	$12.77^{+0.07}_{-0.03}$	$13.84^{+0.03}_{-0.05}$	$11.72^{+0.70}_{-0.59}$	$0.21^{+0.16}_{-0.07}$	$1.72^{+0.08}_{-0.13}$	$-3.49^{+0.04}_{-0.04}$	$2.61^{+0.04}_{-0.05}$	$13.26^{+0.02}_{-0.02}$	$0.08^{+0.01}_{-0.01}$	3.37

Appendix C: Two-point correlation function measurements

Table B.3. Description of blue galaxy samples. Galaxy number densities are given in $h^{-3} \text{Mpc}^3$.

Redshift	$M_g - 5 \log h$	N	$\log n_{\text{gal,obs}}$
$0.2 < z < 0.4$	< -17.8	297 474	$-1.72^{+0.01}_{-0.01}$
$0.2 < z < 0.4$	< -18.8	143 004	$-2.03^{+0.02}_{-0.02}$
$0.2 < z < 0.4$	< -19.8	50 496	$-2.49^{+0.04}_{-0.04}$
$0.2 < z < 0.4$	< -20.8	10 881	$-3.15^{+0.06}_{-0.06}$
$0.4 < z < 0.6$	< -18.8	342 078	$-2.01^{+0.02}_{-0.02}$
$0.4 < z < 0.6$	< -19.8	122 781	$-2.45^{+0.04}_{-0.04}$
$0.4 < z < 0.6$	< -20.8	23 254	$-3.18^{+0.08}_{-0.08}$
$0.6 < z < 0.8$	< -19.8	242 188	$-2.36^{+0.02}_{-0.02}$
$0.6 < z < 0.8$	< -20.8	57 442	$-2.99^{+0.03}_{-0.03}$
$0.6 < z < 0.8$	< -21.8	5 701	$-3.99^{+0.06}_{-0.06}$
$0.8 < z < 1.0$	< -20.8	89 358	$-2.92^{+0.03}_{-0.03}$
$0.8 < z < 1.0$	< -21.8	9 507	$-3.89^{+0.05}_{-0.05}$
$1.0 < z < 1.2$	< -21.8	21 673	$-3.62^{+0.04}_{-0.04}$

Table C.1. Two-point correlation function measurements in the range $0.2 < z < 0.4$.

All galaxies					
$\theta(\text{deg})$	$M_g - 5 \log h < -17.8$	$M_g - 5 \log h < -18.8$	$M_g - 5 \log h < -19.8$	$M_g - 5 \log h < -20.8$	$M_g - 5 \log h < -21.8$
0.0013	1.4818 ± 0.0322	2.3199 ± 0.0670	3.5549 ± 0.1685	7.3561 ± 0.9543	10.3172 ± 6.7590
0.0024	0.8895 ± 0.0213	1.3596 ± 0.0377	1.9627 ± 0.0878	3.8350 ± 0.2778	7.1094 ± 2.8470
0.0042	0.5787 ± 0.0132	0.8173 ± 0.0222	1.1466 ± 0.0466	2.0245 ± 0.1489	2.0728 ± 1.2725
0.0075	0.3949 ± 0.0127	0.5195 ± 0.0180	0.7166 ± 0.0307	1.0055 ± 0.0949	1.2243 ± 0.4861
0.0133	0.2819 ± 0.0106	0.3630 ± 0.0140	0.4808 ± 0.0213	0.7403 ± 0.0500	0.9581 ± 0.2822
0.0237	0.1883 ± 0.0091	0.2340 ± 0.0130	0.2893 ± 0.0182	0.4364 ± 0.0403	0.5257 ± 0.1548
0.0422	0.1243 ± 0.0072	0.1501 ± 0.0103	0.1861 ± 0.0140	0.2800 ± 0.0268	0.4263 ± 0.0780
0.0750	0.0776 ± 0.0060	0.0928 ± 0.0081	0.1179 ± 0.0111	0.1700 ± 0.0238	0.1334 ± 0.0493
0.1334	0.0499 ± 0.0052	0.0593 ± 0.0068	0.0761 ± 0.0086	0.1172 ± 0.0173	0.1055 ± 0.0393
0.2371	0.0342 ± 0.0052	0.0426 ± 0.0067	0.0536 ± 0.0088	0.0820 ± 0.0169	0.0888 ± 0.0225
0.4217	0.0241 ± 0.0046	0.0297 ± 0.0060	0.0362 ± 0.0083	0.0624 ± 0.0138	0.0620 ± 0.0176
0.7499	0.0135 ± 0.0033	0.0165 ± 0.0045	0.0212 ± 0.0056	0.0327 ± 0.0076	0.0330 ± 0.0121
1.3335	0.0047 ± 0.0046	0.0060 ± 0.0047	0.0082 ± 0.0047	0.0148 ± 0.0068	0.0210 ± 0.0104

Red galaxies					
$\theta(\text{deg})$	$M_g - 5 \log h < -17.8$	$M_g - 5 \log h < -18.8$	$M_g - 5 \log h < -19.8$	$M_g - 5 \log h < -20.8$	$M_g - 5 \log h < -21.8$
0.0013	4.7974 ± 0.1698	6.0040 ± 0.2551	7.4692 ± 0.5074	12.0464 ± 2.1742	37.0212 ± 31.1297
0.0024	3.2359 ± 0.0904	3.7019 ± 0.1303	4.2512 ± 0.2044	7.2855 ± 0.8348	14.9207 ± 9.6253
0.0042	2.1016 ± 0.0635	2.2614 ± 0.0780	2.5039 ± 0.1200	3.5656 ± 0.3051	4.8226 ± 3.5344
0.0075	1.4436 ± 0.0540	1.4913 ± 0.0594	1.5948 ± 0.0767	1.8603 ± 0.1843	4.4201 ± 1.7669
0.0133	0.9918 ± 0.0456	1.0089 ± 0.0472	1.0138 ± 0.0489	1.3918 ± 0.0982	3.3844 ± 0.9315
0.0237	0.6053 ± 0.0357	0.6219 ± 0.0381	0.5959 ± 0.0363	0.7927 ± 0.0671	2.1519 ± 0.4732
0.0422	0.3411 ± 0.0230	0.3528 ± 0.0257	0.3319 ± 0.0278	0.4282 ± 0.0418	1.1750 ± 0.2607
0.0750	0.1768 ± 0.0146	0.1953 ± 0.0173	0.1961 ± 0.0178	0.2743 ± 0.0344	0.5895 ± 0.1460
0.1334	0.0950 ± 0.0098	0.1094 ± 0.0125	0.1199 ± 0.0130	0.1749 ± 0.0205	0.3728 ± 0.1074
0.2371	0.0596 ± 0.0092	0.0728 ± 0.0116	0.0807 ± 0.0127	0.1151 ± 0.0196	0.2964 ± 0.0609
0.4217	0.0409 ± 0.0077	0.0506 ± 0.0096	0.0560 ± 0.0115	0.0847 ± 0.0153	0.1940 ± 0.0458
0.7499	0.0239 ± 0.0062	0.0301 ± 0.0087	0.0328 ± 0.0090	0.0462 ± 0.0114	0.1166 ± 0.0292
1.3335	0.0101 ± 0.0062	0.0142 ± 0.0086	0.0142 ± 0.0083	0.0220 ± 0.0119	0.0572 ± 0.0309

Blue galaxies					
$\theta(\text{deg})$	$M_g - 5 \log h < -17.8$	$M_g - 5 \log h < -18.8$	$M_g - 5 \log h < -19.8$	$M_g - 5 \log h < -20.8$	$M_g - 5 \log h < -21.8$
0.0013	1.0697 ± 0.0363	1.6188 ± 0.0912	2.4395 ± 0.3425	5.9775 ± 2.1846	33.1298 ± 40.8099
0.0024	0.5225 ± 0.0225	0.7530 ± 0.0501	1.0018 ± 0.1375	1.0833 ± 0.5121	5.9415 ± 4.5196
0.0042	0.3040 ± 0.0145	0.4330 ± 0.0260	0.5566 ± 0.0585	1.0238 ± 0.2918	1.3497 ± 1.4446
0.0075	0.1801 ± 0.0086	0.2253 ± 0.0130	0.3712 ± 0.0356	0.6845 ± 0.1501	0.8682 ± 0.7125
0.0133	0.1339 ± 0.0067	0.1661 ± 0.0087	0.2189 ± 0.0229	0.1885 ± 0.0979	0.2393 ± 0.3912
0.0237	0.0934 ± 0.0049	0.1144 ± 0.0078	0.1490 ± 0.0161	0.1619 ± 0.0526	0.2913 ± 0.2202
0.0422	0.0681 ± 0.0045	0.0799 ± 0.0062	0.1063 ± 0.0125	0.1598 ± 0.0318	0.1634 ± 0.1230
0.0750	0.0507 ± 0.0046	0.0598 ± 0.0056	0.0753 ± 0.0105	0.1043 ± 0.0234	0.0250 ± 0.0562
0.1334	0.0369 ± 0.0039	0.0414 ± 0.0050	0.0560 ± 0.0085	0.0872 ± 0.0190	-0.0117 ± 0.0385
0.2371	0.0263 ± 0.0039	0.0301 ± 0.0048	0.0366 ± 0.0079	0.0602 ± 0.0165	0.0452 ± 0.0231
0.4217	0.0183 ± 0.0035	0.0214 ± 0.0044	0.0279 ± 0.0079	0.0443 ± 0.0160	0.0169 ± 0.0182
0.7499	0.0098 ± 0.0026	0.0113 ± 0.0030	0.0178 ± 0.0052	0.0276 ± 0.0086	0.0178 ± 0.0104
1.3335	0.0029 ± 0.0037	0.0032 ± 0.0035	0.0070 ± 0.0038	0.0133 ± 0.0063	0.0112 ± 0.0116

Table C.2. Two-point correlation function measurements in the range $0.4 < z < 0.6$.

All galaxies				
$\theta(\text{deg})$	$M_g - 5 \log h < -18.8$	$M_g - 5 \log h < -19.8$	$M_g - 5 \log h < -20.8$	$M_g - 5 \log h < -21.8$
0.0013	1.3933 ± 0.0262	2.2367 ± 0.0615	4.1633 ± 0.2645	9.4751 ± 3.9229
0.0024	0.8180 ± 0.0148	1.2711 ± 0.0286	2.3764 ± 0.1307	7.9475 ± 1.7637
0.0042	0.5276 ± 0.0104	0.7745 ± 0.0193	1.4069 ± 0.0628	3.8402 ± 0.7920
0.0075	0.3481 ± 0.0073	0.4912 ± 0.0125	0.8450 ± 0.0375	1.8830 ± 0.3531
0.0133	0.2218 ± 0.0055	0.3019 ± 0.0090	0.5299 ± 0.0206	0.8854 ± 0.1511
0.0237	0.1398 ± 0.0047	0.1862 ± 0.0069	0.3035 ± 0.0148	0.6038 ± 0.0930
0.0422	0.0876 ± 0.0035	0.1167 ± 0.0055	0.1787 ± 0.0106	0.2470 ± 0.0497
0.0750	0.0563 ± 0.0029	0.0749 ± 0.0044	0.1150 ± 0.0085	0.2270 ± 0.0288
0.1334	0.0378 ± 0.0025	0.0504 ± 0.0035	0.0800 ± 0.0052	0.1409 ± 0.0165
0.2371	0.0254 ± 0.0021	0.0339 ± 0.0029	0.0499 ± 0.0046	0.0948 ± 0.0146
0.4217	0.0145 ± 0.0017	0.0201 ± 0.0025	0.0293 ± 0.0044	0.0497 ± 0.0108
0.7499	0.0066 ± 0.0018	0.0101 ± 0.0027	0.0153 ± 0.0041	0.0197 ± 0.0081
1.3335	0.0022 ± 0.0044	0.0043 ± 0.0041	0.0088 ± 0.0040	0.0124 ± 0.0079
Red galaxies				
$\theta(\text{deg})$	$M_g - 5 \log h < -18.8$	$M_g - 5 \log h < -19.8$	$M_g - 5 \log h < -20.8$	$M_g - 5 \log h < -21.8$
0.0013	4.0250 ± 0.1139	5.0502 ± 0.1719	7.2406 ± 0.5425	19.5919 ± 9.0027
0.0024	2.4772 ± 0.0594	2.9115 ± 0.0828	4.0217 ± 0.2380	10.5452 ± 2.8842
0.0042	1.5544 ± 0.0337	1.7346 ± 0.0467	2.2900 ± 0.1250	6.5579 ± 1.4118
0.0075	1.0081 ± 0.0254	1.0944 ± 0.0255	1.3993 ± 0.0555	3.1910 ± 0.4906
0.0133	0.6123 ± 0.0191	0.6484 ± 0.0204	0.8565 ± 0.0352	1.3759 ± 0.2206
0.0237	0.3545 ± 0.0142	0.3719 ± 0.0141	0.4487 ± 0.0231	0.7683 ± 0.1319
0.0422	0.1899 ± 0.0100	0.2063 ± 0.0112	0.2154 ± 0.0189	0.2399 ± 0.0625
0.0750	0.1101 ± 0.0063	0.1223 ± 0.0077	0.1460 ± 0.0111	0.3053 ± 0.0422
0.1334	0.0662 ± 0.0049	0.0749 ± 0.0059	0.0961 ± 0.0070	0.1346 ± 0.0256
0.2371	0.0459 ± 0.0051	0.0500 ± 0.0052	0.0630 ± 0.0058	0.1122 ± 0.0198
0.4217	0.0261 ± 0.0040	0.0287 ± 0.0042	0.0366 ± 0.0054	0.0466 ± 0.0119
0.7499	0.0124 ± 0.0037	0.0139 ± 0.0041	0.0174 ± 0.0051	0.0242 ± 0.0099
1.3335	0.0053 ± 0.0047	0.0054 ± 0.0049	0.0075 ± 0.0050	0.0124 ± 0.0090
Blue galaxies				
$\theta(\text{deg})$	$M_g - 5 \log h < -18.8$	$M_g - 5 \log h < -19.8$	$M_g - 5 \log h < -20.8$	$M_g - 5 \log h < -21.8$
0.0013	0.9171 ± 0.0314	1.4191 ± 0.0867	2.4257 ± 0.5698	-2.0388 ± 2.8547
0.0024	0.5111 ± 0.0180	0.6902 ± 0.0447	0.8761 ± 0.2250	4.0406 ± 5.0154
0.0042	0.2934 ± 0.0088	0.4165 ± 0.0244	0.8823 ± 0.1442	1.9021 ± 2.6653
0.0075	0.1813 ± 0.0068	0.2587 ± 0.0172	0.4201 ± 0.0649	-0.0745 ± 0.8562
0.0133	0.1165 ± 0.0047	0.1636 ± 0.0106	0.2602 ± 0.0462	-0.3840 ± 0.4747
0.0237	0.0863 ± 0.0027	0.1086 ± 0.0069	0.1781 ± 0.0322	0.0085 ± 0.3271
0.0422	0.0610 ± 0.0026	0.0759 ± 0.0043	0.1388 ± 0.0175	0.2799 ± 0.1861
0.0750	0.0439 ± 0.0025	0.0580 ± 0.0034	0.0942 ± 0.0142	0.2588 ± 0.0975
0.1334	0.0317 ± 0.0020	0.0425 ± 0.0035	0.0851 ± 0.0117	0.2357 ± 0.0651
0.2371	0.0206 ± 0.0016	0.0317 ± 0.0026	0.0593 ± 0.0096	0.0646 ± 0.0473
0.4217	0.0117 ± 0.0014	0.0202 ± 0.0033	0.0396 ± 0.0094	0.0974 ± 0.0322
0.7499	0.0058 ± 0.0015	0.0119 ± 0.0027	0.0289 ± 0.0094	0.0396 ± 0.0289
1.3335	0.0025 ± 0.0040	0.0071 ± 0.0039	0.0219 ± 0.0104	0.0591 ± 0.0314

Table C.3. Two-point correlation function measurements in the range $0.6 < z < 0.8$.

All galaxies				
$\theta(\text{deg})$	$M_g - 5 \log h < -19.8$	$M_g - 5 \log h < -20.8$	$M_g - 5 \log h < -21.8$	$M_g - 5 \log h < -22.8$
0.0013	1.5217 ± 0.0356	3.0868 ± 0.1218	8.0221 ± 1.5873	N/A
0.0024	0.8792 ± 0.0158	1.5273 ± 0.0550	3.5010 ± 0.4573	N/A
0.0042	0.5453 ± 0.0097	0.9487 ± 0.0349	1.7392 ± 0.2452	N/A
0.0075	0.3274 ± 0.0074	0.5640 ± 0.0190	0.9377 ± 0.1134	4.8069 ± 4.4791
0.0133	0.1943 ± 0.0049	0.3223 ± 0.0113	0.6846 ± 0.0694	1.0014 ± 1.4080
0.0237	0.1227 ± 0.0039	0.1870 ± 0.0076	0.3379 ± 0.0336	1.4934 ± 0.8316
0.0422	0.0789 ± 0.0036	0.1129 ± 0.0070	0.1957 ± 0.0269	0.7017 ± 0.3584
0.0750	0.0537 ± 0.0029	0.0772 ± 0.0058	0.1499 ± 0.0178	0.8865 ± 0.2413
0.1334	0.0375 ± 0.0028	0.0543 ± 0.0053	0.0992 ± 0.0151	0.5009 ± 0.1653
0.2371	0.0252 ± 0.0026	0.0372 ± 0.0047	0.0675 ± 0.0129	0.2492 ± 0.0983
0.4217	0.0152 ± 0.0029	0.0236 ± 0.0048	0.0478 ± 0.0130	0.2689 ± 0.0748
0.7499	0.0070 ± 0.0027	0.0128 ± 0.0043	0.0251 ± 0.0098	0.1509 ± 0.0683
1.3335	0.0037 ± 0.0046	0.0053 ± 0.0052	0.0150 ± 0.0078	0.1576 ± 0.0655
Red galaxies				
$\theta(\text{deg})$	$M_g - 5 \log h < -19.8$	$M_g - 5 \log h < -20.8$	$M_g - 5 \log h < -21.8$	$M_g - 5 \log h < -22.8$
0.0013	3.6793 ± 0.1127	5.4089 ± 0.3033	15.8452 ± 4.5991	N/A
0.0024	2.1018 ± 0.0547	2.9129 ± 0.1258	6.9176 ± 1.0528	N/A
0.0042	1.2737 ± 0.0330	1.7428 ± 0.0633	3.6702 ± 0.4636	N/A
0.0075	0.7465 ± 0.0223	0.9808 ± 0.0354	1.4866 ± 0.2029	7.6277 ± 8.1243
0.0133	0.4112 ± 0.0125	0.5170 ± 0.0179	1.1126 ± 0.1101	1.7428 ± 3.0541
0.0237	0.2301 ± 0.0087	0.2942 ± 0.0116	0.4482 ± 0.0544	1.9737 ± 1.5615
0.0422	0.1334 ± 0.0057	0.1669 ± 0.0086	0.2866 ± 0.0401	-0.1086 ± 0.5148
0.0750	0.0861 ± 0.0045	0.1104 ± 0.0071	0.1700 ± 0.0267	0.5358 ± 0.4698
0.1334	0.0590 ± 0.0042	0.0755 ± 0.0066	0.1255 ± 0.0243	0.5715 ± 0.2197
0.2371	0.0407 ± 0.0039	0.0548 ± 0.0061	0.0871 ± 0.0164	0.0901 ± 0.1194
0.4217	0.0244 ± 0.0040	0.0332 ± 0.0059	0.0552 ± 0.0146	0.2193 ± 0.1365
0.7499	0.0120 ± 0.0042	0.0175 ± 0.0055	0.0260 ± 0.0101	0.1040 ± 0.0817
1.3335	0.0083 ± 0.0061	0.0096 ± 0.0060	0.0182 ± 0.0097	0.0749 ± 0.0386
Blue galaxies				
$\theta(\text{deg})$	$M_g - 5 \log h < -19.8$	$M_g - 5 \log h < -20.8$	$M_g - 5 \log h < -21.8$	$M_g - 5 \log h < -22.8$
0.0013	0.8487 ± 0.0496	1.4324 ± 0.2268	4.1554 ± 3.3984	N/A
0.0024	0.4539 ± 0.0264	0.4523 ± 0.1133	0.8359 ± 0.9450	N/A
0.0042	0.2618 ± 0.0144	0.3612 ± 0.0618	-0.2525 ± 0.5016	N/A
0.0075	0.1553 ± 0.0083	0.2681 ± 0.0291	0.0214 ± 0.2699	N/A
0.0133	0.1038 ± 0.0055	0.1476 ± 0.0189	0.3495 ± 0.1536	-1.4572 ± 0.5388
0.0237	0.0771 ± 0.0038	0.1075 ± 0.0114	0.1912 ± 0.0780	-1.1570 ± 0.3078
0.0422	0.0563 ± 0.0031	0.0834 ± 0.0077	0.1621 ± 0.0520	1.9834 ± 1.5364
0.0750	0.0398 ± 0.0024	0.0624 ± 0.0065	0.1584 ± 0.0294	1.5887 ± 0.7844
0.1334	0.0279 ± 0.0023	0.0431 ± 0.0045	0.1002 ± 0.0178	0.5221 ± 0.4101
0.2371	0.0194 ± 0.0022	0.0322 ± 0.0042	0.0503 ± 0.0160	0.4081 ± 0.1886
0.4217	0.0110 ± 0.0020	0.0187 ± 0.0037	0.0539 ± 0.0144	0.4225 ± 0.1605
0.7499	0.0047 ± 0.0015	0.0094 ± 0.0032	0.0298 ± 0.0122	N/A
1.3335	0.0010 ± 0.0032	0.0013 ± 0.0034	0.0136 ± 0.0078	N/A

Table C.4. Two-point correlation function measurements in the range $0.8 < z < 1.0$.

All galaxies			
$\theta(\text{deg})$	$M_g - 5 \log h < -20.8$	$M_g - 5 \log h < -21.8$	$M_g - 5 \log h < -22.8$
0.0013	1.9297 ± 0.0672	6.5369 ± 0.8511	61.7234 ± 41.9290
0.0024	1.1410 ± 0.0340	2.2368 ± 0.2615	28.1877 ± 19.7251
0.0042	0.6653 ± 0.0252	1.5711 ± 0.1320	22.8965 ± 9.3422
0.0075	0.4075 ± 0.0142	0.8834 ± 0.0785	7.9313 ± 3.7334
0.0133	0.2298 ± 0.0084	0.4598 ± 0.0453	1.5075 ± 1.4777
0.0237	0.1446 ± 0.0068	0.2568 ± 0.0267	0.5253 ± 0.3927
0.0422	0.1004 ± 0.0052	0.1774 ± 0.0162	0.4819 ± 0.1835
0.0750	0.0715 ± 0.0043	0.1192 ± 0.0108	0.5160 ± 0.1432
0.1334	0.0525 ± 0.0038	0.0933 ± 0.0076	0.2072 ± 0.0657
0.2371	0.0355 ± 0.0041	0.0574 ± 0.0067	0.1539 ± 0.0430
0.4217	0.0231 ± 0.0041	0.0400 ± 0.0066	0.1461 ± 0.0376
0.7499	0.0156 ± 0.0039	0.0269 ± 0.0066	0.1218 ± 0.0368
1.3335	0.0112 ± 0.0056	0.0195 ± 0.0075	0.1075 ± 0.0371
Red galaxies			
$\theta(\text{deg})$	$M_g - 5 \log h < -20.8$	$M_g - 5 \log h < -21.8$	$M_g - 5 \log h < -22.8$
0.0013	4.0563 ± 0.1830	8.0337 ± 1.1816	62.4523 ± 72.7031
0.0024	2.1944 ± 0.0796	3.5455 ± 0.4726	62.2007 ± 48.4134
0.0042	1.2422 ± 0.0465	2.1323 ± 0.2013	39.5324 ± 16.5788
0.0075	0.6819 ± 0.0246	1.1544 ± 0.1257	11.4103 ± 6.7419
0.0133	0.3588 ± 0.0178	0.6279 ± 0.0633	3.2474 ± 3.0772
0.0237	0.2091 ± 0.0127	0.3088 ± 0.0311	0.4151 ± 0.5025
0.0422	0.1384 ± 0.0083	0.2302 ± 0.0206	0.3642 ± 0.2609
0.0750	0.0970 ± 0.0058	0.1410 ± 0.0155	0.5988 ± 0.1924
0.1334	0.0678 ± 0.0049	0.1041 ± 0.0101	0.1791 ± 0.0805
0.2371	0.0460 ± 0.0057	0.0590 ± 0.0087	0.1322 ± 0.0458
0.4217	0.0295 ± 0.0057	0.0424 ± 0.0068	0.0712 ± 0.0370
0.7499	0.0205 ± 0.0057	0.0267 ± 0.0074	0.1058 ± 0.0316
1.3335	0.0157 ± 0.0072	0.0197 ± 0.0080	0.0573 ± 0.0251
Blue galaxies			
$\theta(\text{deg})$	$M_g - 5 \log h < -20.8$	$M_g - 5 \log h < -21.8$	$M_g - 5 \log h < -22.8$
0.0013	1.0353 ± 0.1344	0.8847 ± 1.3392	320.2051 ± 433.1487
0.0024	0.5535 ± 0.0699	-0.0151 ± 0.7771	123.6391 ± 153.4200
0.0042	0.2876 ± 0.0413	0.6398 ± 0.3317	21.6725 ± 22.7273
0.0075	0.2044 ± 0.0218	0.5090 ± 0.1797	5.3233 ± 5.7498
0.0133	0.1323 ± 0.0117	0.3050 ± 0.1021	1.7491 ± 2.0265
0.0237	0.0975 ± 0.0086	0.2763 ± 0.0572	2.4051 ± 1.5689
0.0422	0.0841 ± 0.0057	0.1246 ± 0.0291	1.5988 ± 0.7454
0.0750	0.0543 ± 0.0046	0.0981 ± 0.0227	0.5858 ± 0.3418
0.1334	0.0430 ± 0.0046	0.0743 ± 0.0126	0.2787 ± 0.1904
0.2371	0.0304 ± 0.0043	0.0546 ± 0.0106	0.3135 ± 0.1561
0.4217	0.0209 ± 0.0041	0.0355 ± 0.0068	0.2642 ± 0.0839
0.7499	0.0135 ± 0.0036	0.0262 ± 0.0077	N/A
1.3335	0.0086 ± 0.0044	0.0182 ± 0.0071	N/A

Table C.5. Two-point correlation function measurements in the range $1.0 < z < 1.2$.

$M_g - 5 \log h < -21.8$			
$\theta(\text{deg})$	All galaxies	Red galaxies	Blue galaxies
0.0013	3.7142 ± 0.2962	6.3867 ± 0.7254	2.2515 ± 0.4971
0.0024	1.6094 ± 0.1283	2.9118 ± 0.3126	0.3135 ± 0.3126
0.0042	0.8737 ± 0.0657	1.7832 ± 0.1386	0.2647 ± 0.1136
0.0075	0.6176 ± 0.0433	1.1093 ± 0.0762	0.2090 ± 0.0738
0.0133	0.2992 ± 0.0273	0.5005 ± 0.0425	0.1765 ± 0.0437
0.0237	0.1926 ± 0.0158	0.3243 ± 0.0254	0.1098 ± 0.0302
0.0422	0.1403 ± 0.0130	0.2180 ± 0.0208	0.0851 ± 0.0162
0.0750	0.1003 ± 0.0095	0.1545 ± 0.0171	0.0516 ± 0.0137
0.1334	0.0727 ± 0.0074	0.1027 ± 0.0162	0.0515 ± 0.0089
0.2371	0.0520 ± 0.0072	0.0742 ± 0.0135	0.0401 ± 0.0081
0.4217	0.0297 ± 0.0056	0.0428 ± 0.0101	0.0213 ± 0.0068
0.7499	0.0137 ± 0.0057	0.0190 ± 0.0064	0.0110 ± 0.0068
1.3335	0.0059 ± 0.0050	0.0076 ± 0.0055	0.0058 ± 0.0054

Table C.6. Best-fitting parameters (from Eq. 25) of M_{\min} and M_1 as function of luminosity threshold corrected for passive redshift evolution to approximate stellar mass selected samples. Results are given for all and red samples, as function of redshift bins. Halo masses are given in $h^{-1}M_{\odot}$

All galaxies						
Redshift	A	M_{\min} $\log(M_t)$	α_M	A	M_1 $\log(M_t)$	α_M
$0.2 < z < 0.4$	0.203 ± 0.005	11.354 ± 0.012	0.503 ± 0.010	0.274 ± 0.017	12.756 ± 0.021	0.439 ± 0.035
$0.4 < z < 0.6$	0.301 ± 0.195	11.570 ± 0.224	0.404 ± 0.149	0.269 ± 0.181	12.715 ± 0.211	0.399 ± 0.191
$0.6 < z < 0.8$	0.377 ± 0.044	11.717 ± 0.063	0.352 ± 0.039	0.514 ± 0.002	12.898 ± 0.002	0.233 ± 0.002
$0.8 < z < 1.2$	0.345 ± 0.006	11.731 ± 0.013	0.383 ± 0.006	0.334 ± 0.002	12.759 ± 0.005	0.335 ± 0.002
Red galaxies						
Redshift	A	M_{\min} $\log(M_t)$	α_M	A	M_1 $\log(M_t)$	α_M
$0.2 < z < 0.4$	0.706 ± 0.341	12.154 ± 0.129	0.307 ± 0.161	0.288 ± 0.009	12.930 ± 0.011	0.477 ± 0.020
$0.4 < z < 0.6$	0.776 ± 0.531	12.209 ± 0.198	0.267 ± 0.241	0.552 ± 0.007	13.141 ± 0.004	0.268 ± 0.008
$0.6 < z < 0.8$	0.761 ± 0.553	12.270 ± 0.233	0.302 ± 0.176	1.033 ± 0.114	13.435 ± 0.043	0.144 ± 0.036
$0.8 < z < 1.2$	0.405 ± 0.429	12.037 ± 0.502	0.433 ± 0.187	0.839 ± 0.114	13.426 ± 0.083	0.188 ± 0.054

All galaxies

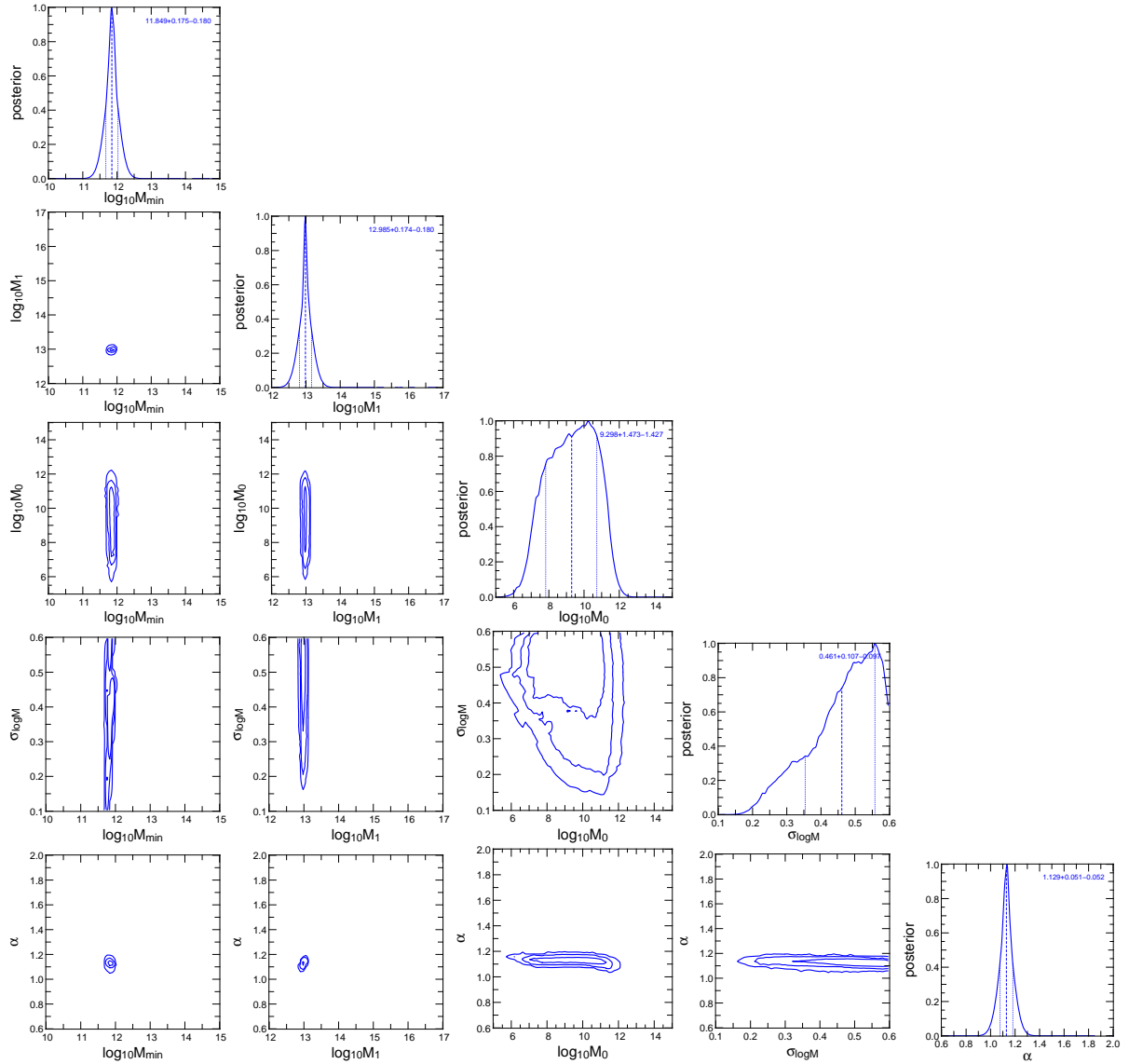


Fig. C.1. 1D (diagonal) and 2D likelihood distributions of best-fitting HOD parameters for the full sample, in the range $0.4 < z < 0.6$, and $M_g - 5 \log h < -19.8$.

Table C.7. Best-fitting parameters (from Eqs. 29 and 30) of b_g and $\log\langle M_{\text{halo}} \rangle$ as function of redshift. Results are given for all and red samples.

All galaxies				
Redshift	Galaxy bias b_g		Mean halo mass $\log\langle M_{\text{halo}} \rangle$	
	a_{bias}	b_{bias}	a_{h}	b_{h}
$0.2 < z < 0.4$	1.071 ± 0.006	0.211 ± 0.011	13.106 ± 0.002	0.111 ± 0.002
$0.4 < z < 0.6$	1.166 ± 0.002	0.288 ± 0.003	13.002 ± 0.009	0.185 ± 0.009
$0.6 < z < 0.8$	1.250 ± 0.018	0.327 ± 0.024	12.846 ± 0.011	0.202 ± 0.010
$0.8 < z < 1.2$	1.430 ± 0.047	0.391 ± 0.030	12.803 ± 0.001	0.174 ± 0.001
Red galaxies				
Redshift	Galaxy bias b_g		Mean halo mass $\log\langle M_{\text{halo}} \rangle$	
	a_{bias}	b_{bias}	a_{h}	b_{h}
$0.2 < z < 0.4$	1.331 ± 0.011	0.162 ± 0.017	13.368 ± 0.001	0.073 ± 0.001
$0.4 < z < 0.6$	1.421 ± 0.013	0.206 ± 0.014	13.246 ± 0.002	0.092 ± 0.002
$0.6 < z < 0.8$	1.572 ± 0.016	0.243 ± 0.021	13.090 ± 0.011	0.129 ± 0.009
$0.8 < z < 1.2$	1.679 ± 0.049	0.375 ± 0.027	12.971 ± 0.003	0.147 ± 0.002